# UC San Diego

## UC San Diego Electronic Theses and Dissertations

**Title**

Toughness of Wear-Resistant Cu-Zr-Based Bulk Metallic Glasses

**Permalink**

https://escholarship.org/uc/item/9s47m159

**Author**

Andersen, Laura Michelle

**Publication Date**

2016

Peer reviewed|Thesis/dissertation

eScholarship.org Powered by the California Digital Library
University of California

UNIVERSITY OF CALIFORNIA, SAN DIEGO

**Toughness of Wear-Resistant Cu-Zr-Based Bulk Metallic Glasses**

A dissertation submitted in partial satisfaction of the
requirements for the degree
Doctor of Philosophy

in

Materials Science and Engineering

by

Laura M. Andersen

Committee in charge:

Kenneth Vecchio, Chair
Douglas Hofmann
Vlado Lubarda
Jian Luo
Marc Meyers
Shyue Ping Ong

2016

Copyright
Laura M. Andersen, 2016
All rights reserved.

The dissertation of Laura M. Andersen is approved, and it is acceptable in quality and form for publication on microfilm and electronically:

_____

_____

_____

_____

_____

_____

Chair

University of California, San Diego

2016

# DEDICATION

To my teachers, who have always been an inspiration to me. And to my very first teachers, Craig and Christine Andersen, who taught me to never stop questioning.

# EPIGRAPH

*To achieve great things, two things are needed;*

*a plan, and not quite enough time.*

—Leonard Bernstein

TABLE OF CONTENTS

LIST OF FIGURES

LIST OF TABLES

ACKNOWLEDGEMENTS

I would like to thank Professor Ken Vecchio for accepting me as a graduate student and providing me the opportunity to navigate my own research path under his guidance. I respect Professor Vecchio's "learn by doing" attitude, which has played a huge part in helping me become a highly skilled and well-rounded materials scientist and engineer. I am amazed at what Professor Vecchio has done over the past six years with the installment of the NanoEngineering Materials Research Center (MRC) and the introduction the undergraduate materials science program. I am honored and forever grateful to have been a part of it. I would also like to thank Dr. Douglas Hofmann, who has had an incredible influence on this work. Doug's optimism and passion for bulk metallic glass research has been one of the most encouraging aspects of this journey, and for that, I cannot thank him enough.

Next, I would like to thank the wonderful professors that I have had a chance to work with during my time at the University of California, San Diego. Prof. Bahadori, thank you for always looking out for me and often going out of your way to secure me a TA-ship. Prof. Conn and Prof. Nemat-Nasser, you are both fantastic teachers. Your teaching styles emphasize the fundamental concepts, which at the end of the day, is what every university student should walk away with. Your passion for teaching really shines and it has inspired me to teach university courses later down my career path. Prof. Lubarda, you are a pleasure to work with and your genuine and optimistic personality always made my day better. Prof. Ong, TA-ing your course was by far the most

challenging, but I learned more in that course than I did in my graduate crystallography class (shh...). You have a wealth of knowledge and I know first-hand that the students think very highly of you because of your consistent involvement with the class. Prof. Marko Lubarda, it was a pleasure to work with you, I only wish we could have worked together more.

I owe a great deal of thanks to the whole team down in the NanoEngineering Materials Research Center (MRC). Wayne Nelson and Sabine Faulhaber, you provided indispensable resources and great company (especially during the early days when max. 4 people occupied the MRC at all times). Thank you to the members of Dr. Vecchio's lab group, who were always willing to help out. Particularly Tyler for your help with EBSD measurements and Roxan for your help in the lab and friendly support. Also, thank you Darren for your advice and words of wisdom. You are a fantastic scientist and have an encouraging personality. I hope someday you will advise a lucky group of doctoral students.

And of course thank you to my fiancée, Dr. Sean Davis, whom I met 2 months into my Ph. D. program. Thank you for making me laugh the past six wonderful years and for putting up with me for this past particularly hectic year. And last but not least, thank you to my family for your unconditional support. Nicole, thank you for editing and proofreading nearly every part of this work. You are a fantastic writer and thanks to you, this work is slightly more interesting to read. Craig and Christine, you are wonderful parents and your constant curiosity is ultimately what has inspired me to pursue a Ph. D.

Chapter 2, in full, is a reprint of the material that is being prepared for publication

in Advanced Engineering Materials. Hofmann, Douglas; Andersen, Laura; Kolodziejska, Joanna; Roberts, Scott; Borgonia, John-Paul; Vecchio, Kenneth; Kennett, Andrew, WILEY-VCH Verlag GmbH & Co. KGaA, 2016.

Chapter 3, in full, is a reprint of the material that was submitted for publication in the Journal of Non-Crystalline Solids. Andersen, Laura; Faulhaber, Sabine; Hofmann, Douglas; Vecchio, Kenneth, Elsevier B.V., 2016. The dissertation/thesis author was the primary investigator and author of this material.

Chapter 4, in full, is a reprint of the material as it appears in Materials Science and Engineering: A. Andersen, Laura; Hofmann, Douglas; Vecchio, Kenneth, Elsevier B.V., 2016. The dissertation/thesis author was the primary investigator and author of this material.

I would also like to thank the Achievement Rewards for College Scientists (ARCS) Foundation and the Jet Propulsion Laboratory (JPL) Summer Internship Program for financial support. Thanks also to my committee members, Dr. Vlado Lubarda, Dr. Jian Luo, Dr. Marc Meyers and Dr. Shyue Ping Ong, for your assistance and support in the completion of this dissertation.

## VITA

| | |
|---|---|
| 2009 | B. S. in Materials Science and Engineering, University of Washington, Seattle |
| 2011-2015 | Graduate Teaching Assistant, University of California, San Diego |
| 2011 | M. S. in Materials Science and Engineering, University of California, San Diego |
| 2012 | JPL Summer Research Program, Jet Propulsion Laboratory, Pasadena, CA |
| 2015 | Failure Analysis and Materials Characterization Internship, Apple Inc., Cupertino, CA |
| 2016 | Ph. D. in Materials Science and Engineering, University of California, San Diego |

## PUBLICATIONS & PRESENTATIONS

L. M. Andersen, D. C. Hofmann, and K. S. Vecchio, "Effect of zirconium purity on the glass-forming-ability and notch toughness of $Cu_{43}Zr_{43}Al_7Be_7$," *Materials Science and Engineering: A*, vol. 674, pp. 397–405, 2016.

L. M. Andersen, S. Faulhaber, D. C. Hofmann and K. S. Vecchio, "Criteria to Optimize the Toughness of Cu-Zr-based Bulk Metallic Glasses with in-situ Crystallization", Submitted to *Journal of Non-Crystalline Solids* on August 14, 2016.

D. C. Hofmann, L. M. Andersen, J. Kolodziejska, S. N. Roberts, J.-P. Borgonia, K. S. Vecchio, A. Kennett, "Optimizing Bulk Metallic Glasses for Robust, Highly Wear-Resistant Gears", In preparation.

L. M. Andersen, D. C. Hofmann and K. S. Vecchio, "Toughness of Wear-Resistant Cu-Zr-Based Bulk Metallic Glasses", *Materials Science & Technology*, Columbus, OH, Oct. 2015.

L. M. Andersen, D. C. Hofmann and K. S. Vecchio, "Investigating the Fracture Mechanics of Wear-Resistant, High Glass-Forming Bulk Metallic Glasses", *TMS Annual Meeting & Exhibition*, San Diego, CA, Feb. 2014.

ABSTRACT OF THE DISSERTATION

**Toughness of Wear-Resistant Cu-Zr-Based Bulk Metallic Glasses**

by

Laura M. Andersen

Doctor of Philosophy in Materials Science and Engineering

University of California, San Diego, 2016

Kenneth Vecchio, Chair

Bulk metallic glasses (BMGs) have the potential to exhibit exceptional wear-resistance due to their high hardness and strength. Combined with their other unique properties, this makes them ideal candidates for a wide range of technological applications (e.g. gears, bearings, biomaterials). In the course of this dissertation, high-glass-forming bulk metallic glasses are prepared and characterized in order to identify wear-resistant compositions and optimize their toughness.

First, a comprehensive study identifies a class of Cu-Zr-based BMGs that exhibit

more exceptional wear performance than other BMGs. The results demonstrate that when BMGs are designed properly, they exhibit wear properties that compete with, and can surpass, state-of-the-art engineering materials. It is identified that, in order to optimize the wear performance of Cu-Zr-based BMG gears, toughness should be maximized.

Second, the notch toughness of wear-resistant $Cu_{43}Zr_{43}Al_7Be_7$ BMGs with in-situ crystallization is investigated. In order to identify in-situ crystallization using X-ray diffraction (XRD) with Cu K$\alpha$ radiation, extremely long dwell times and high X-ray fluxes are required. This demonstrates the importance of reporting operating parameters when trying to evaluate the amorphous nature of BMGs. XRD, energy-dispersive X-ray spectroscopy (EDS) and electron backscatter diffraction (EBSD) are used to identify the metastable crystalline phase. The notch toughness is found to correlate closely with the amount of crystallization and the composition of the remaining amorphous matrix.

Finally, the effect of substituting standard-grade zirconium lump (99.8% excluding up to 4% hafnium) for high-purity zirconium crystal bar (99.5%) in $Cu_{43}Zr_{43}Al_7Be_7$ is investigated. Introducing low-purity zirconium significantly decreases the glass-forming-ability and reduces the notch toughness of the BMG. Furthermore, Weibull statistics provide an analysis of the variability in toughness for high-purity ingots synthesized both in a small laboratory arc-melter and synthesized commercially.

The dissertation concludes with a summary of key findings that have led to our increase in knowledge and a discussion of particularly pressing directions for future research in this field.

# 1 Introduction

If you freeze any liquid fast enough, even liquid metal, it becomes a glass [1]. Materials we typically describe as glassy (i.e. polymers and silica) form localized chemical bonds. In order to crystallize, the molecules must find an appropriate place in the lattice and position themselves at just the right angle relative to their neighbors. Thus, the kinetics proceed slowly and even moderate cooling rates suffice to vitrify such a liquid into an amorphous structure. On the other hand, metals are bound by freely shared conduction-band electrons that have no orientational requirement and only need to adopt translational order to crystallize. As a result, supercooled metals tend to crystallize extremely fast. Not until 1960, was it was discovered that metals could also be cooled into a glassy state [2]. However, the chief breakthrough was recognizing that the propensity to crystallize is dramatically lower for certain alloys than others [3, 4]. These certain alloys became known as *bulk* metallic glasses (BMGs). Bulk metallic glasses (in contrast to simply metallic glasses) are generally considered alloys in which the transformation kinetics are slow enough to form totally amorphous samples with dimensions of 1 mm or greater.

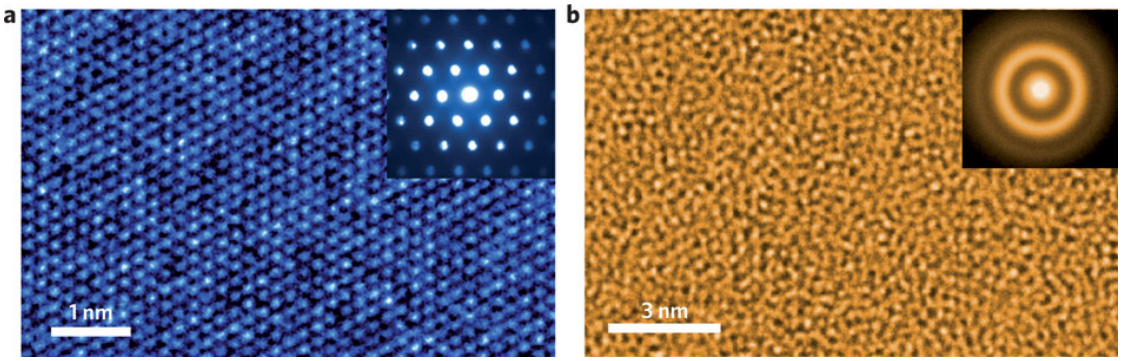


**Figure 1.1**: High-resolution TEM images of (a) the crystalline atomic structure of a typical metal and (b) the amorphous structure of a metallic glass. The inset in each image shows the corresponding selected-area electron diffraction (SAED) pattern. Taken from Ref. [5].

The atomic structure is the most striking characteristic of a metallic glass as it is fundamentally different from ordinary metals. The atomic structure of conventional crystalline metals is periodic and the atoms show a repeating pattern over an extended range. By contrast, when observing BMGs, no discernible long-range patterns exist in the amorphous atomic structure. Fig. 1.1 shows transmission electron microscope (TEM) images comparing the atomic structure of a conventional metal (low-carbon steel) and that of a $Zr_{67}Ni_{33}$ metallic glass.

A direct consequence of the amorphous structure in BMGs is very high yield strengths, approaching the theoretical limits and far exceeding the strength values available in crystalline metals and alloys. For example, yield strengths of over 1.8 GPa have been achieved in Ti-base BMGs, which is more than twice the strength of conventional titanium alloys [6]. Meanwhile, Fe-base BMGs can have yield strength values approaching 4.0 GPa, exceeding that of any other metallic alloy [7]. Another unique property of BMGs is their superior elastic strain limit, or the ability to retain their original shape

after undergoing very high loads and stress. This particular property was the basis for Liquidmetal's™[1] effort to commercialize BMG golf club heads in the late 1990's [8]. The combination of high strength and a high elastic limit puts BMGs in a property space where no other materials currently sit, as shown by the Ashby plot in Fig. 1.2. In addition, BMGs have also been shown to exhibit high hardness, excellent corrosion resistance and the ability to undergo thermoplastic forming. Thus, BMGs offer an opportunity to revolutionize the field of structural materials with properties outside the envelope achievable using current technology.

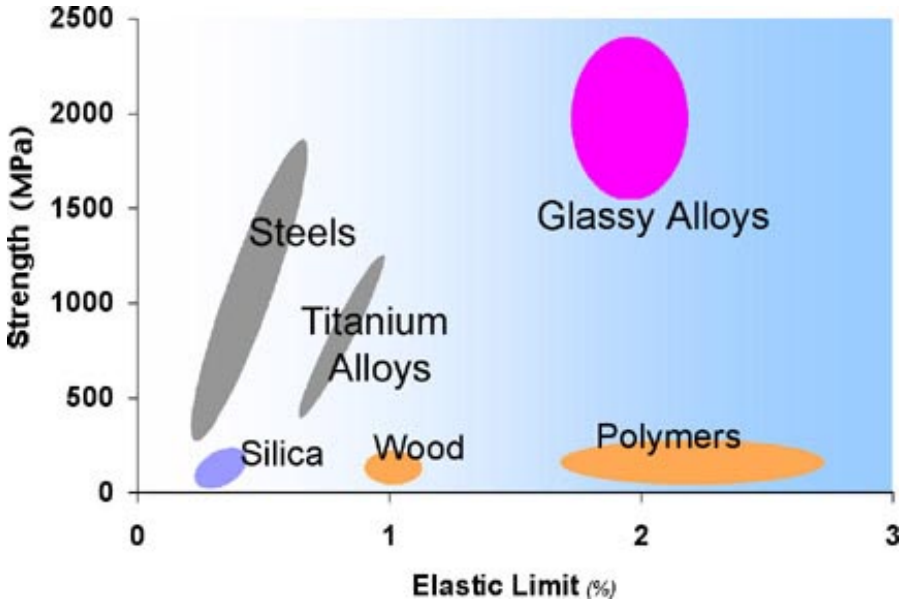


**Figure 1.2**: Ashby plot showing the relative comparison between the strength and elastic limit for different materials. No other known material has the combination of strength and elastic limit as BMGs. Taken from Ref. [9].

However, it is important to remember that, just like crystalline alloys, the properties of BMGs are inherently tied to their composition and can vary dramatically from one composition to the next. Too often BMGs become grouped into one monolithic class of

[1]Liquidmetal® Technologies, 30452 Esperanza, Rancho Santa Margarita, CA 92688.

materials, but this is far from an accurate description. For example, although Fe-based BMGs are the strongest known metallic alloy, Al-based BMGs have strength values one third of Fe-based BMGs [8]. Furthermore, BMGs are generally thought to be incredibly wear-resistant, but it will be shown later in this work that many BMG compositions have very poor wear performance. Achieving a combination of all these properties previously discussed is not trivial, and the issue becomes more complex as we have to factor in raw material costs and processability.

A major ongoing issue with bulk metallic glasses is their lack of plastic strain in tension that is inherent in glassy materials. Thus, the ability to make bulk specimens through reproducible methods has indeed created a focus on the deformation mechanisms. Recent reports on BMGs have shown significant improvements in plastic strain in compression and even shown work-hardening behavior [10]. However, process-related variations in key properties such as fracture toughness still present complications. Even small fluctuations in processing can create drastic changes in material properties. For example, in the case of the Liquidmetal™[2] golf clubs, the commercial-scale processing method introduced internal defects that acted as crack-initiation sites, thus severely limiting the fatigue performance of the club [11]. Another challenge lies in obtaining tougher, more fracture-resistant alloys in a cost-effective manner. For example, a Pd-based alloy has been developed with an unrivaled combination of fracture toughness and yield strength [12]. But the prohibitive cost of Pd reduces use of these alloys to a mere laboratory curiosity.

[2]Liquidmetal® Technologies, 30452 Esperanza, Rancho Santa Margarita, CA 92688.

The biggest remaining challenge for implementing BMGs as engineering materials is combining durability, scaleability and cost. In this work we take an in-depth look at these issues as related to wear-resistant BMGs. This includes a comprehensive investigation of the relationships among the microstructure, toughness and wear-resistance in BMGs, particularly Cu-Zr-based alloys. Thus, the theoretical introduction, which follows in this chapter, provides background information on the thermodynamics and kinetics of glass formation (Section 1.1), the structure of bulk metallic glass (Section 1.2), the mechanics of metallic glass deformation (Section 1.3), Cu-Zr-based alloys (Section 1.4), and wear-resistant materials (Section 1.5). The chapter concludes with a clear statement of the aims and objectives of this work (Section 1.6).

## 1.1 Glass Formation and Transformation Kinetics

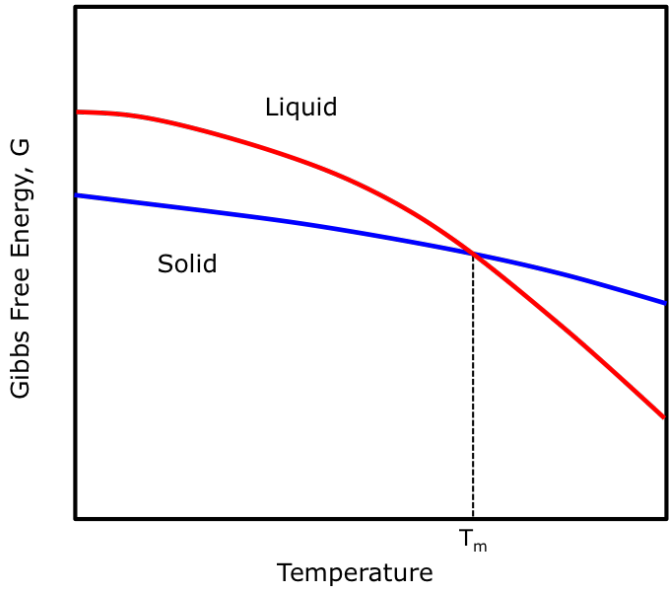


**Figure 1.3**: Gibbs free energy for a solid and a liquid as a function of temperature.

Glass formation of a metallic alloy occurs when nucleation and growth of the crystalline phase is bypassed. Consider a typical metal alloy above its melting temperature, $T_m$. The alloy is in the liquid state because it is the most thermodynamically favored state or the state in which it has the lowest Gibbs free energy. For constant pressure, the Gibbs free energy of a system, $G$, is defined as

$$G = H - T\Delta S \tag{1.1}$$

where $H$ is enthalpy or internal energy, $T$ is temperature in Kelvin and $S$ is entropy. Fig. 1.3 shows the approximate variation in the Gibbs free energy, as a function of temperature, for any given material. At high temperature, the $-T\Delta S$ term dominates, and therefore, the high entropy of the liquid causes it to have the lowest $G$. At low temperature, the ordered stable crystalline structure reduces the enthalpy, $H$, thus reducing the Gibbs free energy, $G$.

When the molten alloy is cooled below $T_m$, the liquid is thermodynamically driven to crystallize because the free energy of the system is lowest in the solid state. However, this transformation does not necessary occur immediately. An activation barrier needs to be overcome in order to nucleate crystals, so the liquid state is maintained below $T_m$ and the material is considered a supercooled (or undercooled) liquid. The degree of undercooling that can be achieved depends on several factors relating to both the material composition and the cooling process, such as the initial viscosity of the liquid, the amount of heterogeneous nucleation sites and the cooling rate. The difference between a glass

forming alloy and a typical crystalline alloy is that a glass-forming alloy can be more significantly undercooled.

During undercooling, the atomic structure of the alloy is still liquid-like, and the dynamics become more and more sluggish upon further cooling. The point of solidification depends on two opposing forces. First, the activation barrier decreases, which means there is less of a driving force for the atoms to rearrange into an ordered state. Second, with significant undercooling the viscosity increases very rapidly. At some point the viscosity becomes so high that the material is considered solid for all practical purposes, and it maintains a glassy structure similar to that of the high viscosity liquid. The temperature at which the supercooled liquid becomes a solid glass is referred to as the glass transition temperature, $T_g$.

### 1.1.1 The Glass Transition Temperature

The glass transition temperature, $T_g$, is the temperature at which the supercooled liquid becomes a solid glass, or vice-versa. As a supercooled liquid is cooled, the specific volume decreases and the viscosity continues to increase. At some temperature, the viscosity becomes so high that the liquid structure gets "frozen-in." Traditionally, $T_g$ is the temperature at which the viscosity of the material reaches $10^{12}$ Pa-s, but in reality, there is no sharply defined glass transition temperature [13]. The glass transition is strictly a kinetic event that spans a range of temperatures and is closely dependent on the imposed cooling or heating rate and the thermal history of the glass. Fig. 1.4 schematically depicts how the glass transition is shifted to lower temperatures when the

cooling rate is decreased. The faster the alloy is solidified from the liquid state, the higher the measured glass transition temperature (i.e. $T_{g,1}$).

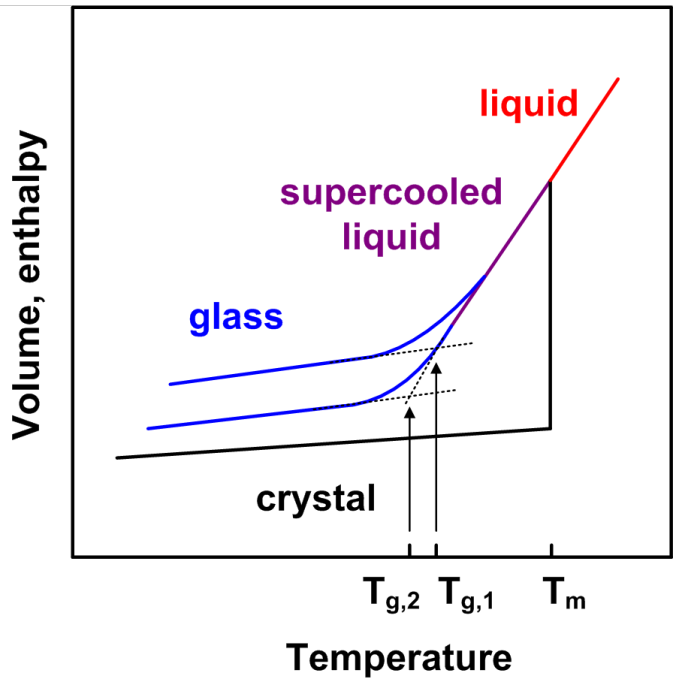


**Figure 1.4**: Variation of specific volume or enthalpy with temperature for a normal and glass-forming material. Taken from Ref. [14].

At $T_g$, there is also a sudden drop in heat capacity, $C_p$, a manifestation of the fewer degrees of freedom in the solid [15]. This sudden change in heat capacity is the basis for how $T_g$ of a metallic glass is most often measured. The increase in $C_p$ can be observed when heating a metallic glass in a differential scanning calorimeter (DSC) at a constant rate. Typically, a heating rate of 20 K/min is used.

### 1.1.2 Kinetics of Glass Formation

Since the problem of glass formation turns out to be purely kinetic in nature, theoretically every liquid will form a glass provided that the cooling rate is sufficiently

quick and crystallization can be hindered [1]. The homogenous nucleation rate, $I$, for the formation of crystalline nuclei in a supercool liquid can be expressed as

$$I = \frac{A}{\eta} \exp\left( -\frac{16\pi\sigma^3}{3k_B T \Delta G_c{}^2} \right) \tag{1.2}$$

where $A$ is a constant, $\eta$ is viscosity, $\sigma$ is the interfacial surface energy, $k_B$ is the Boltzmann constant, $T$ is temperature in Kelvin and $\Delta G_c$ is the free energy at crystal formation [16]. Equation 1.2 shows that with increasing $\eta$ the nucleation rate decreases, which explains why the further an alloy can be undercooled, the easier it is to form a glass. We also see that for a given temperature and $\eta$, the nucleation rate decreases very steeply with increasing $\sigma$ or decreasing $\Delta G_c$. Increasing $\sigma$ follows from an increase in packing density, and $\Delta G_c$ represents the driving force for crystallization, thus these parameters both contribute to the glass-forming properties. The growth rate of a crystal from a supercooled liquid, $U$, is defined by

$$U = \frac{k_B}{3\pi l^2 \eta} \left[ 1 - \exp\left( -\frac{n\Delta G_c}{k_B T} \right) \right] \tag{1.3}$$

where $l$ is the average atomic diameter and $n$ is the average atomic volume [16]. Like the nucleation rate, the crystal growth rate also varies with $1/\eta$ for a given temperature.

Combining 1.2 and 1.3 with the Johnson-Mehl-Avrami equation for transformation kinetics [16], the volume fraction of crystals, $x$, as a function of time, $t$, can be written as

$$x = \frac{\pi}{3} U^3 t^4 I \tag{1.4}$$

It follows then that the time needed to form a given fraction of crystals, $x$, is

$$t = \left( \frac{3x}{\pi I U^3} \right)^{1/4} \tag{1.5}$$

A plot of the crystallization time, $t$, as a function of temperature, $T$, is the foundation for a time-temperature-transformation (TTT) diagram. A TTT diagram can also be constructed experimentally through a series of isothermal DSC scans. Fig. 1.5 shows the calculated and experimentally determined TTT curves determined for the Zr-based BMG known as Vitreloy™[3]. The solid line represents the calculated TTT curve for a crystalline volume fraction of $x = 10^{-4}$, and it is overlaid with experimental data points as determined by DSC.

By inspection of the TTT curve, the critical cooling rate to avoid crystallization, $R_c$, is

$$R_c = \frac{\Delta T}{t_n} \tag{1.6}$$

where $\Delta T$ is the amount of undercooling and $t_n$ is the time at the nose of the TTT curve. $R_c$ is a very effective indicator of how easily a composition will solidify into a glass. This concept, called glass-forming-ability, will be discussed further in the next section.

[3]Liquidmetal® Technologies, 30452 Esperanza, Rancho Santa Margarita, CA 92688.

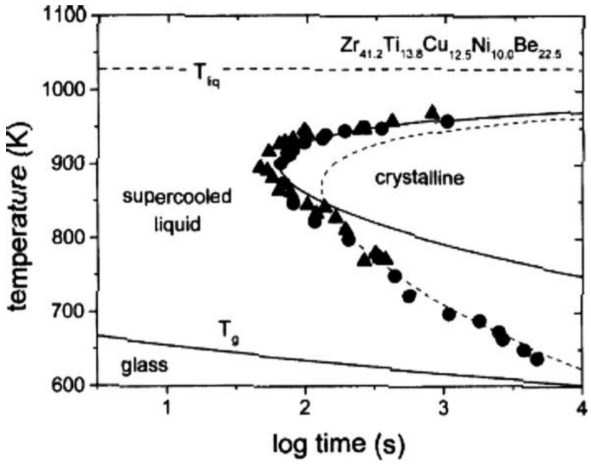


**Figure 1.5**: Time-temperature-transformation (TTT) curves for the onset of crystallization for Vitreloy™. Data obtained by electrostatic levitation (●) and processing in high-purity carbon crucibles (▲) are included. Taken from Ref. [17].

### 1.1.3 Glass-Forming-Ability

The fundamental requirement for the synthesis of a metallic glass is a high cooling rate, although, as discussed above, certain characteristics of the alloy itself can increase the likelihood of vitrification of the melt. The glass-forming-ability (GFA) is defined as the ability of a metallic alloy to transform into the glassy state. A high GFA is important because it is directly related to the critical cooling rate, $R_c$, which determines the maximum thickness that can be made amorphous. As an approximation,

$$d_c = \sqrt{\frac{10}{R_c}} \tag{1.7}$$

where $d_c$ is the diameter or thickness, measured in centimeters [18]. Both $R_c$ and $d_c$ are commonly accepted as criteria used to describe GFA, where the smaller $R_c$ and the larger $d_c$, the better the GFA [19].

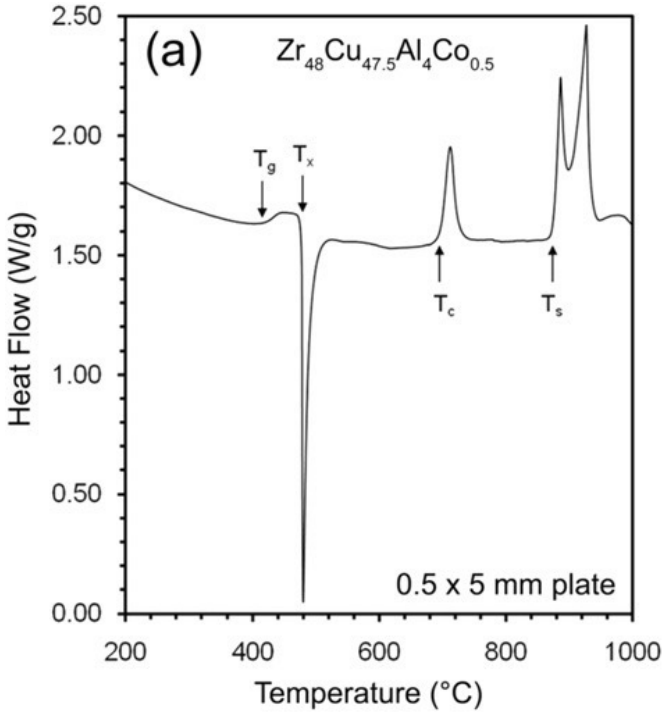


**Figure 1.6**: DSC curve from a $0.5 \times 5 \times 30$ mm plate of a $Zr_{48}Cu_{47.5}Al_4Co_{0.5}$ BMGMC. The glass transition temperature, $T_g$, the crystallization temperature, $T_x$, a transition temperature of the composite, $T_c$, the melting temperature, $T_m$, and the liquidus temperature, $T_l$, are noted. Note that $T_c$ does not exist for monolithic BMGs. Taken from Ref. [20].

The ability to predict the GFA is especially desirable as it spares the tedious trial and error approach in the search for new metallic glass formers. Fortunately, many parameters have been developed that correlate the GFA to characteristic temperatures such as the glass transition temperature, $T_g$, the crystallization onset temperature $T_x$, and the liquidus temperature, $T_l$. These temperatures can be readily determined with differential scanning calorimetry (DSC) or differential thermal analysis (DTA) [21, 22]. Fig. 1.6 shows a DSC scan of a $Zr_{48}Cu_{47.5}Al_4Co_{0.5}$ BMGMC during heating at a constant rate of 20 K/min. The first event upon heating from room temperature is $T_g$, and it is characterized by temporary change in slope of the curve. Temperatures above $T_g$ and

below $T_x$ are in the supercooled liquid region (SLR) and the BMG exists as a highly viscous liquid. At $T_x$, the alloy undergoes an exothermic reaction and crystallizes. Upon further heating, the samples will melt when it reaches $T_l$.

The width of the supercooled liquid region (SLR) is referred to as the temperature interval between $T_x$ and $T_g$, and it is expressed as $\Delta T_x = T_x - T_g$ [23]. A large $\Delta T_x$ corresponds to a large SLR, suggesting that the glassy phase is very stable and resists crystallization. In an early observation, it was proposed, and in many cases it was confirmed, that the GFA is directly related to $\Delta T_x$ [23]. However, with the discovery of more exotic multicomponent BMGs, such as $Pd_{40}Cu_{30}Ni_{10}P_{20}$ and $La_{62}Al_{14}(Cu,Ni)_{24}$ exceptions to this criterion have been noted [24, 25]. Therefore, it has been suggested that $\Delta T_x$ should be used only to evaluate the thermal stability of the supercooled liquid and not the GFA of the alloy. Most BMGs have a large $\Delta T_x$ [26].

The reduced glass transition temperature, $T_{rg}$, is the ratio of the glass transition temperature, $T_g$, to the liquidus temperature, $T_l$, or $T_{rg} = T_g/T_l$ [1]. As the reduced glass transition temperature increases (i.e. $T_g$ approaches $T_l$), the homogenous nucleation rate in the undercooled liquid becomes sluggish and crystallization is suppressed. In other words, the critical casting rate decreases and the GFA increases. However, it should be noted, that it is important to use the correct temperature for the completion of melting, as no correlation was found for the relationship $T_{rg} = T_g/T_m$ [27]. Almost all bulk forming metallic glasses have values of $T_{rg} \geq 2/3$, where, theoretically, homogeneous nucleation of the crystalline phase is completely suppressed.

The higher the value of $T_{rg}$, the higher the viscosity of the liquid and thus the

easier it will be to solidify into a glass. A large $T_g$ also results in a small temperature window between the stable region of the glass and the melt, which corresponds to deep eutectics in the phase diagram of a given system. A deep eutectic in an alloy system is a eutectic temperature that exhibits a significantly lower melting point than the individual components. Although, in some cases, maximum GFA has been found to be shifted slightly towards the steeper liquidus line, resulting in "off-eutectic" compositions [28].

The relative depth of a eutectic in an alloy system can be described by the $\alpha$ parameter [29]. The weighted liquidus temperature is the numerator, where $x_i$ is the atomic fraction of element $i$, $T_i$ is the melting temperature of element $i$, and $n$ is the number of elements in the alloy. Within good glass-forming alloys, the actual liquidus temperature, $T_l$, is far below that calculated from an ideal solution, as shown in Fig. 1.7. The magnitude of the $\alpha$ parameter describes this deviation:

$$\alpha = \frac{\sum_{i=1}^{n} x_i}{T_l} \tag{1.8}$$

A eutectic will generate an $\alpha$ value greater than one, with larger $\alpha$ parameters signify higher glass-forming-ability. Specifically, an $\alpha$ parameter value in excess of 1 suggests a slight tendency for glass formation, while $\alpha$ values greater than 1.5 suggest a very strong tendency.

Other parameters for determining the GFA of alloys will not be discussed here, but a number are described in [30]. Each criteria has been successful in identifying glass-forming alloys (either ribbons or bulk-forming), although exceptions have been

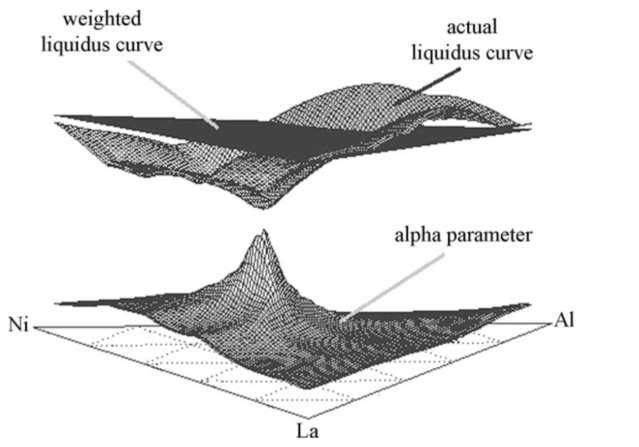


**Figure 1.7**: Plot of alpha parameter for the La-Ni-Al system, actual (calculated based on thermodynamics), and ideal (weighted) liquidus profile. Taken from Ref. [29].

reported for all cases. Most criteria are somewhat related to each other and they can be roughly divided into two groups: (1) parameters considering thermodynamic aspects and (2) parameters considering structural aspects. This not surprising as a high viscosity, $\eta$, (outcome of a densely packed liquid structure) and a low driving force for crystallization, $\Delta G_c$, (thermodynamic aspect of glass formation) have been identified to be essential for the extraordinary GFA of bulk metallic glasses [31].

From a less theoretical approach, a well-known and successful strategy used to identify high GFA bulk systems is the Inoue criteria. Based on the extensive data generated on the synthesis of BMGs, Inoue formulated three basic empirical rules for the formation of BMGs [32]:

1. The alloy must contain at least three components.
2. The atomic size difference should be at least 12% among the main constituent elements.

3. There should be negative heats of mixing among the major constituent elements.

The first criterion is based on thermodynamic aspects of glass formation, the second is based on topological aspects and the third is required for homogeneous alloying to occur. It has been often cited that these criteria are, not surprisingly, reminiscent, and opposite, of the well-known Hume-Rothery rules used to predict the stability of intermetallic phases [33]. Although exceptions to the Inoue criteria have been found, several hundreds of BMG compositions have been successfully discovered using these three empirical "guidelines."

## 1.2 Structure of Metallic Glass

Metallic glasses can broadly be subdivided into two categories—alloys of two or more metallic elements (solute-solute type) and alloys in which a non-metallic or semi-metallic element is essential for glass formation (solute-solvent type). Solute-solute type glasses have been observed over a wide composition range, but they are typically poor glass formers with a maximum critical casting diameter of 1.5 mm [34]. The solute-solvent type, on the other hand, are bulk glass formers, and they typically consist of 75–85 at% metal and 15–25 at% metalloid atoms. The small atomic size of the metalloid component fits into structural voids, creating a densely packed structure that frustrates crystallization [26]. The focus of this work is on multicomponent Cu-Zr-based BMGs, which are of the solute-solvent type. Therefore, the following discussion will focus on the structure of the solute-solvent type BMGs.

### 1.2.1 Dense Icosahedral Packing

The most widely accepted structural model for solute-solvent metallic glasses is a dense packing of icosahedral clusters (the three-dimensional equivalent of a pentagon) [35]. The five-fold rotational symmetry of the icosahedral (or icosahedral-like) clusters make it mathematically impossible for them to arrange into a periodic repetitive pattern. Thus, the atomic structure of a metallic glass does not exhibit translational symmetry or long-range order like that of typical crystalline metal. Furthermore, many authors have shown that a high packing density is essential to achieve high glass forming ability [3, 36, 37]. In order for a crystalline phase to form, the clusters must be dissociated and a substantial redistribution of the component elements is required. A highly dense random packing of atoms in a supercooled BMG alloy results in extremely slow atomic mobility and leads to the suppression of the nucleation and growth of a crystalline phase and excellent glass-forming-ability [37].

From a topological point of view, atomic packing efficiency is closely related to the atomic size ratio between the solute and solvent atoms. For a hard-sphere packing model, the ideal icosahedral dense packing requires an atomic size ratio $r_B/r_A$, of 0.902, where $r_A$ and $r_B$ are the atomic radii of the solvent and center solute atoms, respectively [38]. The atomic size ratio of constituent elements has therefore been proposed as an important factor governing glass-forming-ability, particularly in binary alloys that only contain transition metals [39]. However, the optimal composition for the best glass formers cannot be determined from the ideal effective atomic size ratio because

of the multiple compositional variables of multicomponent alloys and the possible chemical heterogeneity of the constituent elements.

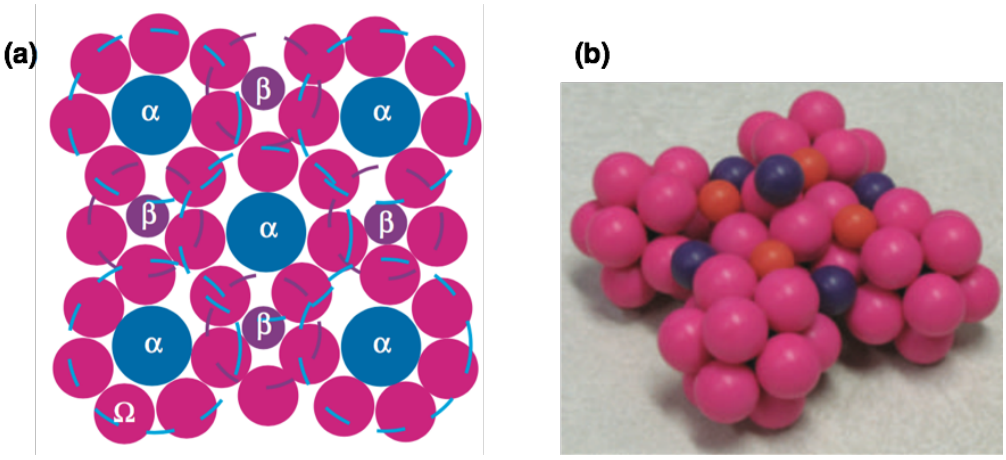


**Figure 1.8**: Schematic of a single cluster unit cell for the dense cluster packing model. (a) 2D illustration and (b) 3D representation of interpenetrating clusters and efficient atomic packing around each solute. The $\alpha$ and $\beta$ sites represent the positions of the solutes, which are topologically distinct. The other sites, $\Omega$, are occupied by the solvent. Taken from Ref. [40].

Beyond the nearest-neighbor clusters, there is little significant structure, although some specific packings of icosahedra have been proposed. Miracle [40] suggested a model for medium-range order (MRO) in multicomponent metallic glasses by packing the sphere-like clusters in face-centered cubic (FCC) and hexagonal close-packed (HCP) configurations to most efficiently fill a three-dimensional space. Fig. 1.8b shows Miracle's familiar schematic and 3D model of a single cluster unit cell for the dense cluster packing model. In contrast, Sheng [41] proposed that an icosahedral five-fold packing scheme is a more favorable ordering pattern of cluster-cluster connections. In both MRO models, the order of the cluster-forming solutes cannot extend beyond a few cluster diameters due to internal strains and topological frustration, thus beyond the nanoscale the metallic

glasses structure is disordered.

### 1.2.2 Chemical Short-Range Order

The local order does not come merely from a straightforward topological packing of hard spheres of fixed sizes; it is also affected by the chemistry of the specific alloy [42]. In the liquid state, a large negative heat of mixing, $\Delta H_{mix}$, enhances the interactions among the components and promotes chemical short range ordering (CSRO) [43]. In other words, if $\Delta H_{mix}$ between two elements is largely negative, the atoms will tend to locate around one another. On the other hand, if $\Delta H_{mix}$ is positive, they will tend to locate away from one another.

The discussion here will focus on CSRO models for Cu-Zr-based BMGs, due to their attractive mechanical properties and their importance in this work. Icosahedra structures develop prominently in these BMGs because of the the large negative $\Delta H_{mix}$ among the constituent elements [43]. In binary Cu-Zr, it is impossible to encage every Cu by Zr atoms only, when the Cu concentration is high and $\Delta H_{mix}$ is highly negative. Instead, Zr atoms mix with Cu in the first-neighbor shell of Cu. This allows leeway in adjusting the relative proportions of Zr and Cu to facilitate icosahedral packing.

The excellent glass-forming multicomponent alloy, $Cu_{45}Zr_{45}Ag_{10}$, exhibits a heterogenous atomic structure of Zr-rich interpenetrating clusters centered by paired and stringed Ag atoms and Cu-rich Cu-centered icosahedra [44]. Similar to simple icosahedra, interpenetrating clusters also lack translational periodicity and are difficult to grow in comparison with the crystal counterparts. The light blue spheres in Fig. 1.9

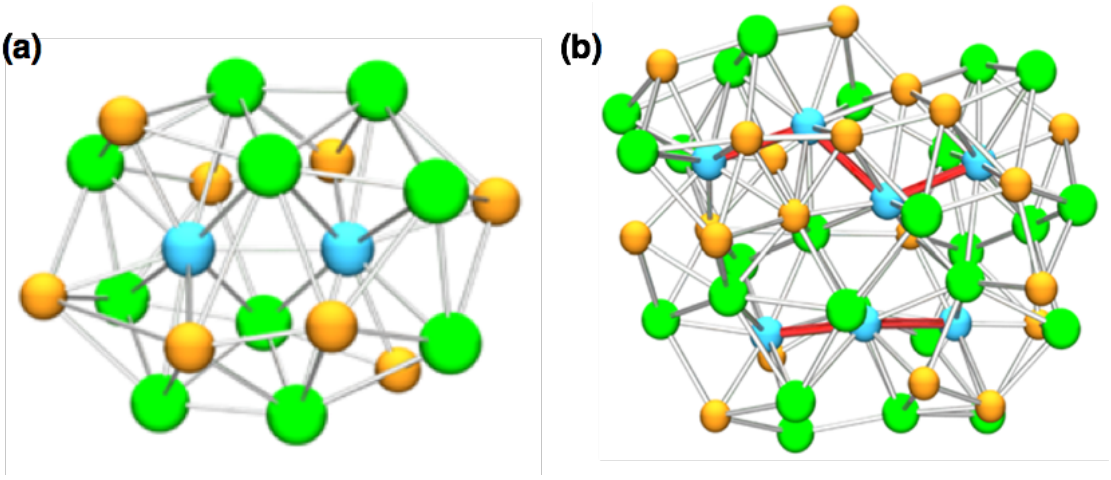


**Figure 1.9**: Ag-centered interpenetrating clusters in $Cu_{45}Zr_{45}Ag_{10}$. (a) An interpenetrating cluster with paired Ag atoms in the center and (b) a large interpenetrating cluster centered by stringed Ag atoms. The red line denotes Ag-Ag connections. The yellow, green, and light blue spheres represent the Cu, Zr, and Ag atoms, respectively. Taken from Ref. [44]

.

schematically show (a) an Ag pair and (b) a string of Ag atoms. More than 90% of the Ag atoms are in the form of Ag atom pairs and strings, which creates an inhomogeneous distribution of constituent elements. Furthermore, the atomic-scale heterogeneity causes the Cu-centered clusters to contain more Cu and less Zr, resulting in an effective atomic size ratio very close to the ideal value of 0.902 [44]. Thus, atomic-scale heterogeneity plays a key role in stabilizing the liquid phase and in improving the glass-forming-ability of $Cu_{45}Zr_{45}Ag_{10}$.

Similarly, the structure of $Cu_{46}Zr_{47}Al_7$ is best described as overlapping icosahedral motifs centered around Cu and Al (the smaller species), with mixed atomic species in the first shell [42]. Interpenetrating Cu-centered icosahedra are the characteristic structural feature, with some additional Al-centered icosahedra. Note that the atomic size ratio, $r_{Al}/r_{Zr} = 0.905$, is rather close to the ideal ratio of 0.902. This suggests that Al

surrounded by Zr would be the topologically optimal way for the most favorable packing. However, this is unlikely since the composition of this alloy is rather rich in Cu and the calculated $\Delta H_{mix}$ is negative between any two species [42]. Therefore, using simulations, most Al-centered icosahedra in $Cu_{46}Zr_{47}Al_7$ were found to have mixed atomic species in the shell. Evidently, alloying with 7% Al greatly enhances the five-fold symmetry of the Cu-centered polyhedra, making them more populous, complete, and regular, and thus stabilizing the structure [45].

While a definitive model for the atomic structure of disordered metallic glasses has yet to be determined, this remains an important research effort. The cluster ordering provides a physical basis for medium range order and locally distributed free volume that play a dominant role in the deformation response of the metallic glasses. Bulk metallic glasses exhibit mechanical properties that are very different from those of crystalline materials because of their unique structural characteristics. Understanding the atomic structure of the best glass formers is a viable route to quantitatively designing new BMGs with excellent physical, chemical and mechanical properties.

## 1.3 Mechanisms for Deformation and Fracture

Some of the most attractive aspects bulk metallic glasses are their interesting mechanical properties, which occupy a unique niche compared with other classes of engineering materials. For example, while their elastic modulus is of the same order of magnitude as that of crystalline alloys of the same composition, their room temperature

strength is much higher. Furthermore, they have been shown to exhibit significant ductility in bending, high hardness, and high resistance to corrosion, oxidation and wear [23].

On the other hand, metallic glasses do not strain harden. Rather, deformation at room temperature occurs inhomogeneously through plastic strains concentrated in localized shear bands [46]. Even though the strain can be extremely large within the shear bands (up to 10) [47], the small thickness and the usually limited number of shear bands prevents them from contributing to macroscopic plastic deformation. Consequently, bulk metallic glasses tend to be subject to a weakest link phenomenon and fail catastrophically due to uninhibited propagation of the shear bands. In general, bulk metallic glasses are considered to be "macroscopically brittle."

At high temperatures ($> 0.7T_g$) the deformation mechanism of metallic glasses is best described through viscous flow and can result in significant plasticity. The deformation mechanisms in this regime has significant commercial importance due to the net-shape forming capability of metallic glass, although this discussion is outside the scope of this work and therefore will not be presented. A more detailed discussion can be found in [26].

In both regimes, the plasticity of metallic glasses is largely based on two atomic-scale mechanisms: (1) deformation-induced dilatation or free volume and (2) local events of cooperative shearing of atomic clusters termed shear transformation zones (STZs).

### 1.3.1 The Free Volume Model

The classical "free-volume" model was first developed by Cohen, Grest and Turnbull [48]. Spaepen expanded on this single-atom model to describe plastic flow in metallic glass based on the competition between the stress-driven creation and the diffusional annihilation of free volume [49]. The model views deformation as a series of diffusion-like local atomic jumps, as depicted schematically in Fig. 1.10. These jumps are favored near vacant sites of high free-volume (or low packing density) which can more readily accommodate them.

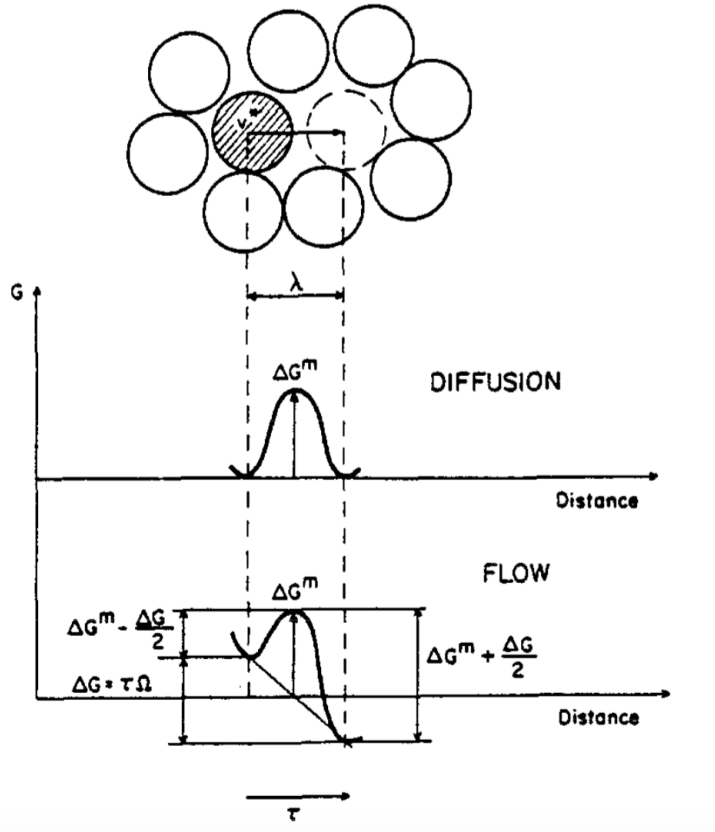


**Figure 1.10**: Schematic of an individual atomic jump, the basic step for macroscopic diffusion and flow. Taken from Ref. [49].

When an external force is applied, the atomic jumps preferentially occur in the direction of the force, which results in a net forward flux of atoms and forms the basic mechanism for flow. If the applied shear stress is large enough, free volume can be created as an atom with squeezes into a neighboring free volume site with slightly smaller volume [49]. This dilation during deformation is similar to that seen in granular materials. For example, the disappearance of water under footsteps on a wet beach, or the firmness of ground coffee in a vacuum-packed bag [50].

As the free volume increases, the viscosity in the shear bands decreases and the ability of the material to flow becomes more pronounced. In other words, the shear-induced dilation leaves the already deformed regions to be more prone to further deformation. Consequently, the strain becomes localized in narrow regions of the metallic glasses, which leads to shear softening.

### 1.3.2 Shear Transformation Zones

In an alternative, complementary model, Argon demonstrates that flow localization occurs due to local events of cooperative shearing of atomic clusters called shear transformation zones (STZs) [51]. A STZ is a small cluster of randomly-close packed atoms that spontaneously and cooperatively reorganize under the action of an applied shear stress. Instead of holes opening up in the surrounding coordination sites of an atom, as described in the free volume model, the whole collection of atoms rearranges as one cooperative movement. The schematic in Fig. 1.11a shows an example of the local rearrangement in a STZ. Compare this to the schematic of a local atomic jump, as

described by Spaepen, in Fig. 1.11b.

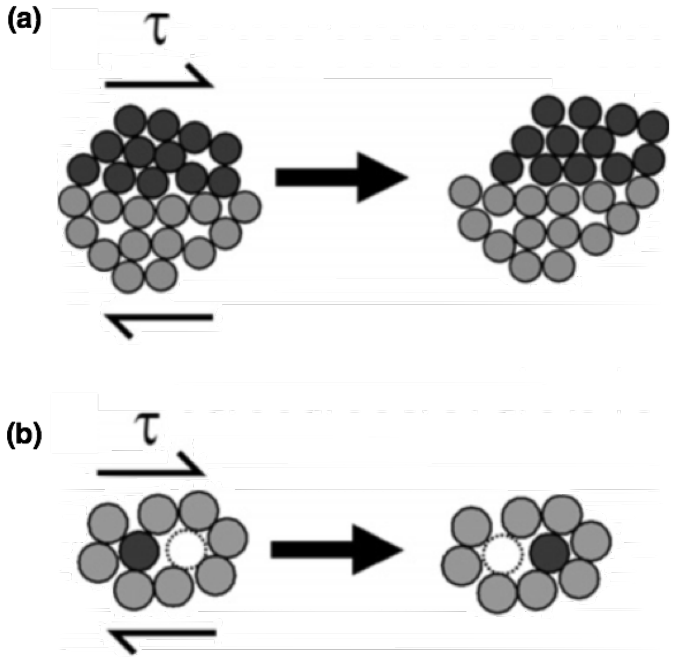


**Figure 1.11**: Schematic of the atomistic deformation mechanisms proposed for amorphous metals, including (a) a shear transformation zone (STZ), after Argon [51], and (b) a local atomic jump, after Spaepen [49]. Taken from Ref. [52]

The further propagation of an applied shear strain occurs when one STZ creates a localized distortion of the surrounding material and perturbation in strain rate, triggering the formation of large planar bands of STZs, or so-called "shear bands" [51]. Alternatively, intense shearing may accumulate in a small volume, which then propagates as a front that sweeps across the shear plane. Most likely, the true sequence of events is intermediate to these two extreme cases [52].

Various simulations suggest that STZs are common to deformation of all amorphous metals, but there is still no consensus as to the size of a STZ. It is likely that the structure, size and energy of STZs varies from one glass to the next. Argon originally

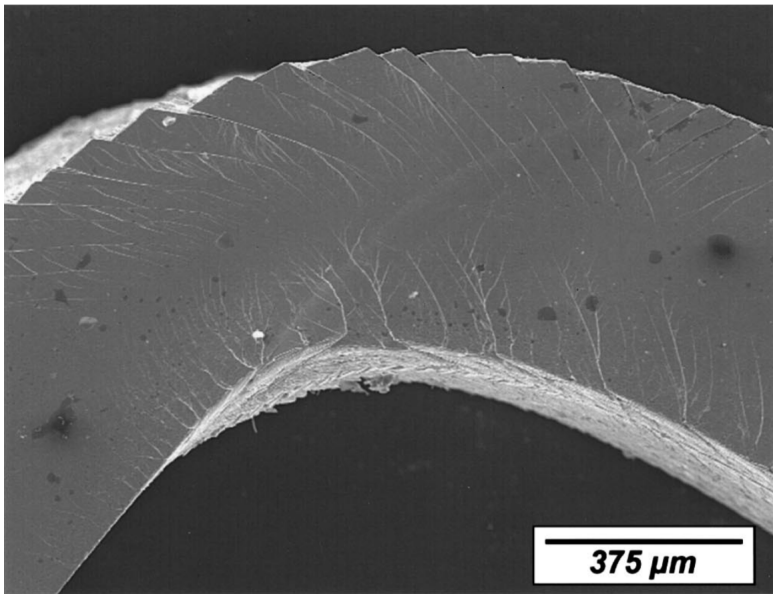


**Figure 1.12**: SEM micrograph illustrating the "slip steps" or surface offsets associated with shear bands in deformed metallic glasses. A bent strip of $Zr_{57}Nb_5Al_{10}Cu_{15.4}Ni_{12.6}$ illustrates slip steps formed in both tensile and compressive modes of loading, on the top and bottom surfaces, respectively. Taken from [53].

proposed that they are on the order of a few atomic diameters [51]. On the other hand, more recent results suggest that STZ comprise of up to 100–120 atoms [54] or even over 600 atoms [55]. On a macroscale, shear band operations can be seen in the form of "slip steps" in a deformed bulk metallic glass, as shown in the SEM image in Fig. 1.12.

### 1.3.3 Strain Softening

Both the shear transformation zone or the free-volume for local diffusive jumps can be used to describe the deformation of metallic glasses. In general, both models suggest the same basic sequence of events. As stress is increased, strains are first accommodated elastically, until the stress level increases to the point where it can activate flow locally. The mismatch in strain rate between the locally strained regions and

unstrained regions leads to strain softening, which continues to lead to a further increase in the strain rate mismatch until the shear band propagates across the whole sample.

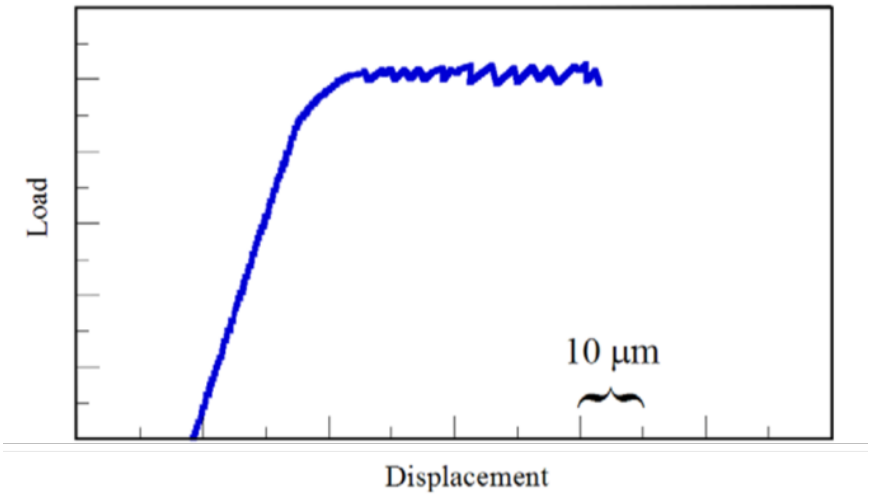


**Figure 1.13**: Example of serrated flow in metallic glasses as shown in the compression response of a $Pd_{77.5}Cu_6Si_{16.5}$ specimen. The data represents a displacement controlled experiment, thus serrations are represented as load drops. Taken from [52].

Plastic shearing within a shear band stops when the applied strain is fully accommodated by the shear accumulated within the band, relaxing the stress. This situation can occur in constrained loading, such as indentation [56], crack opening [57], or compression [58]. After a single shear band operates and arrests, the material can be deformed further through additional shear banding operations. Load-displacement curves from such events exhibit flow serrations, which are noticeable small drops in the load when the experiment is displacement-controlled, as shown in Fig. 1.13.

### 1.3.4 Elastic Property Correlations

Although BMGs do not exhibit macroscopic ductility, they are capable of plastic compression (malleable) and can be bent plastically. By applying a model developed by Pugh for crystalline metals, Lewandowski et. al. found that the ductility and fracture energy of BMGs correlates with the ratio of the shear modulus to the bulk modulus, $G/B$, or the brittleness ratio [59, 60] as shown in Fig. 1.14. Glassy alloys with a low value of $G/B$ exhibited extensive shear banding and a high fracture energy. Below a critical $G/B$ ratio of 0.41–0.43 BMGs are considered ductile, whereas above this value they are deemed brittle. For isotropic materials, the $G/B$ ratio can also be expressed in terms of Poisson's ratio, $\nu$:

$$\frac{G}{B} = \frac{3(1-2\nu)}{2(1+\nu)} \tag{1.9}$$

It follows then, that a high Poisson's ratio of >0.31–0.32 signifies a ductile BMG.

Since $G$ and $B$ can be measured using non-destructive ultrasonic measurements, this relationship presents an attractive method to characterize the toughness of BMGs. Furthermore, computational methods have been developed to predict the Poisson's ratio of a multicomponent glass and used to design BMGs with significant plasticity [62, 63]. For example, $Pt_{57.5}Cu_{14.7}Ni_{5.3}P_{22.5}$, designed based on its particularly large Poisson's ratio of $\nu = 0.42$, exhibits large plastic strains in compression and bending and has a high fracture toughness of $K_c = 80$ MPa-$m^{1/2}$ [64].

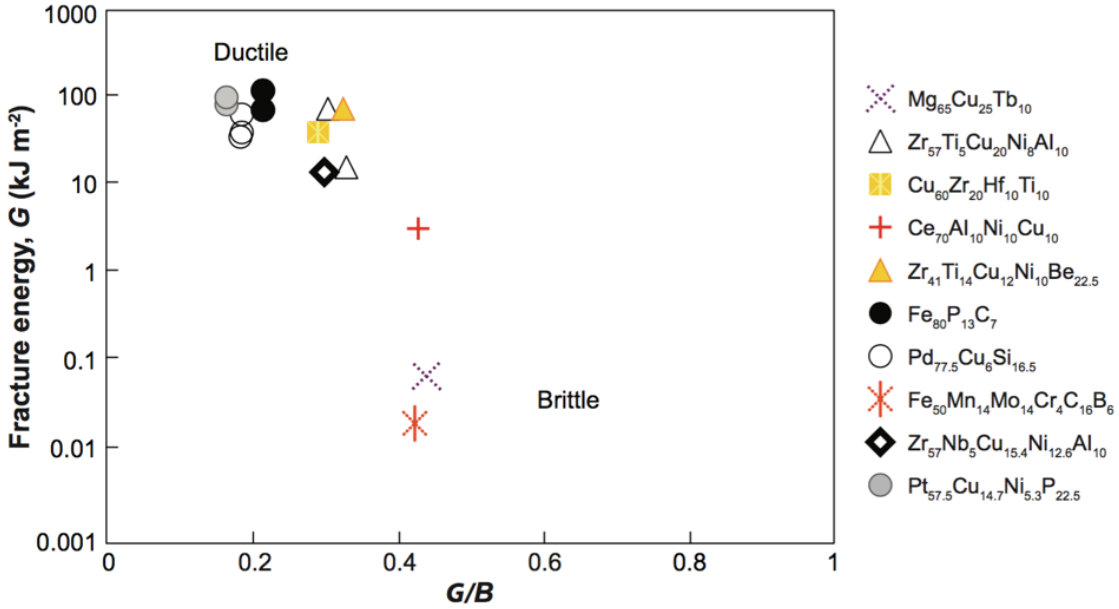


**Figure 1.14**: The correlation of fracture energy, $G$, with elastic modulus ratio, $G/B$, for as-cast metallic glasses for which relevant data are available (compositions in at%). Adapted from Refs. [60, 61].

### 1.3.5 Weibull Statistics

Since BMGs are flaw sensitive and yield discretely as a shear band is formed, they may be amenable to the weakest link assumption. If there exists a weaker band of material in the specimen, then a shear band should form preferentially there.

A Weibull analysis is a statistically approach that is commonly used to describe the fracture strength when fracture initiates from a single critical flaw [65]. Weibull analysis has historically been applied to ceramics and brittle metals. Over a decade ago, some metallic glass ribbons were studied using a Weibull analysis [66, 67], and more recently, may studies on larger bulk metallic glasses specimens have been reported [ref]. There are generally two assumptions on which the Weibull theory is based: (i) fracture will occur at the weakest point within the specimen, and (ii) the material is statistically

homogeneous at a sufficiently large length scale, i.e. the probability to find a critical flaw in a given volume element is the same as in the overall volume [65].

The Weibull equation describes the fracture probability, $P_f$, for a given uniaxial stress, $\sigma$ (or in this case, fracture toughness, $K_{IC}$). The 3-parameter Weibull equation is:

$$P_f = 1 - \exp\left[-\left(\frac{\sigma - \sigma_u}{\sigma_0}\right)^m\right] \tag{1.10}$$

where $\sigma_0$ is the scale parameter, $m$ is the Weibull modulus or shape parameter, and $\sigma_u$ is the location parameter, which denotes the stress where the probability of failure is zero.

When $\sigma_u = 0$, Eq. 1.10 reduces to a 2-parameter Weibull distribution. Because it is very risky to assume a finite threshold strength without careful screening or non-destructive evaluation, a 2-parameter model is usually used as a safe assumption. Many studies on BMGs have taken this approach [68, 69], while others argue that a 3-parameter model is more appropriate [70, 71]. Numerical simulations and experimental data show that, if sample data are limited in number ($N \leq 40$) and the location parameter, $\sigma_u$, is not too large, the 2-parameter Weibull distribution is the preferred model [72]. Thus, in this work, a 2-parameter Weibull analysis is implemented.

The parameters of a 2-parameter Weibull distribution can be obtained by linearizing Eq. 1.10 and setting $\sigma_u = 0$:

$$y_i = \ln\left\{\ln\left[\frac{1}{(1 - P_{f,i})}\right]\right\} = m\ln\sigma_i - m\ln\sigma_0 = mx_i - m\ln\sigma_0 \tag{1.11}$$

In a double-logarithmic plot of $\ln(\ln(1/(1-P_f)))$ plotted against $\ln\sigma$, the

Weibull modulus, $m$, is the slope, and the scale parameter, $\sigma_0$, is obtained from the $y$-intercept.

## 1.4 Cu-Zr-Based Amorphous Alloys

Cu-Zr-based amorphous alloys are composed of mainly copper and zirconium atoms in equal (or nearly equal) amounts. Their good mechanical properties and high glass-forming-ability (GFA) suggests that they could be used for structural applications. Therefore, a number of Cu-Zr-based BMGs have been synthesized in recent years, and they are increasingly becoming the focus of studies on strength, plastic strain and toughness. Currently, the maximum critical casting diameter reported in this system is 25 mm in a $Cu_{36}Zr_{48}Ag_8Al_8$ alloy [73]. On the other hand, limiting the content of Cu and Zr to strictly a 1:1 ratio, the maximum critical casting diameter is 12 mm, in both $Cu_{42}Zr_{42}Ag_8Al_8$ and $Cu_{43}Zr_{43}Al_7Be_7$ [73, 74].

Binary Cu-Zr-based amorphous alloys can be vitrified into glasses across a wide compositional range of $Cu_{100-x}Zr_x$ with $20 \leq x \leq 75$, although a majority of these alloys cannot be cast in bulk form [77]. The bulk Cu-Zr-based BMG compositions include $Cu_{64.5}Zr_{35.5}$, $Cu_{64}Zr_{36}$, $Cu_{60}Zr_{40}$, $Cu_{50}Zr_{50}$, and $Cu_{46}Zr_{54}$ [28, 78–80] with a maximum GFA of 2 mm in $Cu_{50}Zr_{50}$ [80]. It is interesting to note, that the highest glass formers do not coincide with deep eutectics in the equilibrium phase diagram [28]. Rather the location of an intermetallic forming near a deep eutectic decreases the GFA of the alloy. For example, the high GFA in binary $Cu_{50}Zr_{50}$ can be attributed to a deep metastable

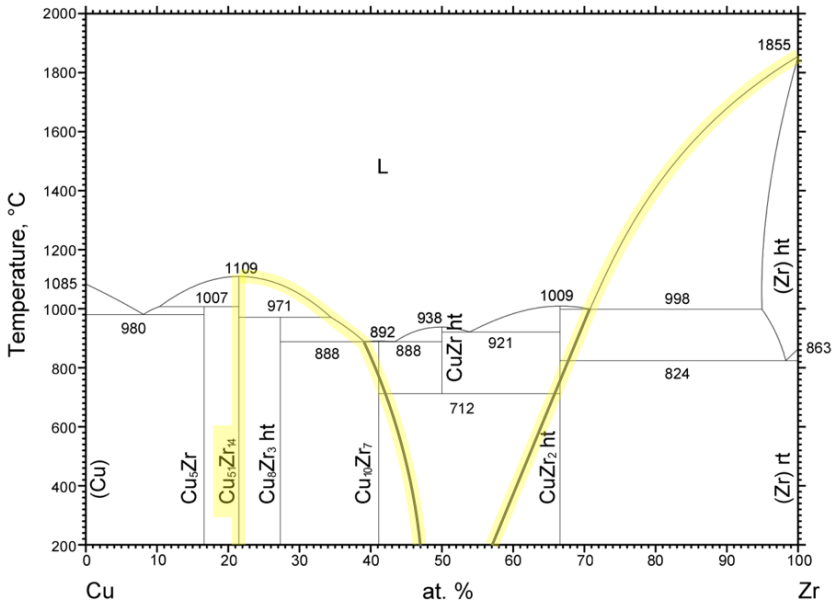


**Figure 1.15**: The equilibrium phase diagram of Cu-Zr. The bold lines indicate the extrapolated liquidus lines for the metastable eutectic of $Cu_{51}Zr_{14}$ and $\beta$-Zr. This eutectic is significant in the absence of the compounds $CuZr_2$, CuZr, $Cu_{10}Zr_7$, and $Cu_8Zr_3$. Adapted from Ref. [75]. Phase diagram taken from Ref. [76].

eutectic between $Cu_{51}Zr_{14}$ and $\beta$-Zr [75], as shown by the extrapolated liquidus lines in Fig. 1.15. In this system, the primary intermetallic phase competing with glass formation is $Cu_{51}Zr_{14}$.

In general, minor alloying elements improve the GFA of a given system, and in $Cu_{50}Zr_{50}$ minor additions of aluminum destabilize $Cu_{51}Zr_{14}$ and promote glass formation [75, 81]. Additions of 4 at% Al to $Cu_{50}Zr_{50}$ increases the critical casting diameter from 2 mm to 5 mm [75]. It is expected that the addition of aluminum atoms helps segregate the Cu and Zr atoms due to the mixing enthalpies. Furthermore, the improved GFA of $Cu_{47.5}Zr_{47.5}Al_5$ has been attributed to its dense liquid structure and its high value of viscosity [82].

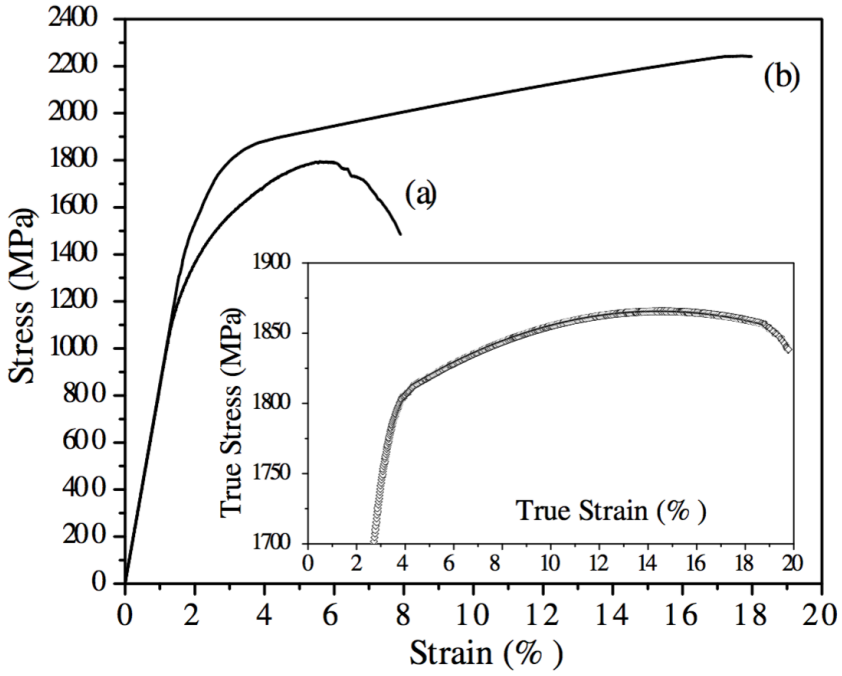


**Figure 1.16**: Stress-strain curves of (a) $Cu_{50}Zr_{50}$ and (b) $Cu_{47.5}Zr_{47.5}Al_5$ under compression at a strain rate of $8 \times 10^{-4}$ $s^{-1}$, showing a highly "work-hardenable" metallic glass up to 18% strain. The inset shows the true stress-true strain curve of alloy (b) $Cu_{47.5}Zr_{47.5}Al_5$ as obtained from conversion of the engineering stress-strain values. Taken from Ref. [10].

From an engineering point of view, the binary and ternary Cu-Zr-based BMGs have a certain attractiveness as they exhibit considerable plastic strain along with high yield strength under room temperature compression. In particular, ternary $Cu_{47.5}Zr_{47.5}Al_5$ has received special attention because of its significant work hardening behavior compared to other Cu-Zr-based BMGs [10, 83, 84]. Fig. 1.16 shows this "work-hardening" behavior in the compression stress-strain curve. $Cu_{50}Zr_{50}$ and $Cu_{47.5}Zr_{47.5}Al_5$ show appreciable compressive plasticity with a fracture strain of about ~8% and ~18%, respectively, and a yield strength of 1.3 GPa and 1.5 GPa, respectively [10]. The increase in ductility and strength with the addition of 5% Al to $Cu_{50}Zr_{50}$ is attributed to a unique

atomic-scale inhomogeneity in the amorphous structure, which promotes nucleation of the shear bands and continuous multiplication during deformation [10].

In some Cu-Zr-based alloys that exhibit pronounced plasticity in compression, microscopic observations show evidence of nanocrystals in the amorphous matrix [74]. It has been suggested that some discrepancies in plasticity reported in this system may be a consequence of small amounts of crystals that have not been detected during the investigations. On the other hand, one study observed no chemical or structural inhomogeneities before testing a sample that exhibited a large plastic strain [85]. Rather, after testing, localized deformation induced nanocrystallization was identified in the plastic $Cu_{47.5}Zr_{47.5}Al_5$ alloy, and no indication of nanocrystallization during deformation was seen in the macroscopically brittle $Cu_{45}Zr_{45}Al_{10}$ [85].

The addition of aluminum (3–8 at%) in binary Cu-Zr-based BMGs has been shown to promote the formation of the metastable austenitic B2-CuZr phase [86]. Such partially crystalline BMGs are interesting because crystalline CuZr can undergo a deformation induced martensitic transformation from a cubic primitive B2 ($Pm\bar{3}m$) to a monoclinic $B19'$ (P21/m and $C_m$) phase, similarly to the NiTi system that exhibits a shape memory effect [87]. The uniform tensile ductility and lack of strain-softening in partially crystalline $Cu_{47.5}Zr_{47.5}Al_5$ reinforced by a homogeneously distributed spherical B2-CuZr phase has been attributed to this deformation-induced phase transformation [86]. Furthermore, the compressive plasticity and yield strength were found to scale with the crystalline volume fraction of B2-CuZr in $Cu_{47.5}Zr_{47.5}Al_5$ [88].

Additionally, the addition of a fourth element to the Cu-Zr-Al system leads to

an enhancement in GFA as predicted by confusion principle [89]. For example, the quaternary alloy $Cu_{46}Zr_{42}Al_7Y_5$ exhibits a high critical casting diameter of 10 mm. The increase in GFA is attributed to the alloying effect of Y, which lowers the liquidus temperature of the matrix alloy and brings the composition to a deeper eutectic [43]. Furthermore, $Cu_{43}Zr_{43}Al_7Be_7$ exhibits a high GFA of 12 mm, a yield strength of 2.0 GPa and a compressive plastic strain of over 4.0% [74].

## 1.5 Wear-Resistance

Wear is the progressive damage process of material loss which occurs on the surface of a solid interacting with its working environment. Wear is not simply a result of a material's properties, but operating conditions and the environment also play a role in the wear behavior of a system. Thus, wear resistance is not considered as an intrinsic property of a material. For example, the wear rate of crystalline metals can be influenced by velocity, load, temperature, surface roughness and material hardness [90–92].

In most engineering applications, different forms of lubricants and surface coatings are used to avoid excessive wear and damage, but some applications do not allow for this. Without lubricants or coatings, contacting materials usually exhibit severe wear causing catastrophic damage. Thus a comprehensive understanding of the dry sliding wear of metals from microstructure perspective is of great importance. Lubricated gear sets are susceptible to wear caused by adhesion, abrasion, and polishing. Unlubricated, related failures include brittle fracture, ductile fracture and plastic deformation [93].

There are several different ways to classify wear mechanisms, with the most important being adhesive-wear and abrasive-wear mechanisms [94]. According to some estimates, two-thirds of all wear encountered in industrial situations occurs because of adhesive- and abrasive-wear mechanisms. In many situations several wear mechanisms operate simultaneously, however a primary wear mechanism that dominates the amount of material removal from the surface is always present.

### 1.5.1 Adhesive Wear

Adhesive wear occurs when two nominally flat solid bodies are in sliding contact, with or without lubrication. Wear initiates because of adhesion that occurs at asperity contacts [94]. The asperities are then sheared by the sliding force, and it is possible that this leads to a fractured fragment. In Fig. 1.17, a schematic shows the two possibilities of a break during shearing of an interface. In most cases, the break during shearing occurs at the interface (path 1), because the interfacial adhesion strength is expected to be small as compared to the breaking strength of the material. On the other hand, break may occur in one of the two asperities (path 2) and a small fragment may become attached to the other surface. Some asperities are fractured by a fatigue process during repeated loading and unloading action resulting in formation of loose particles.

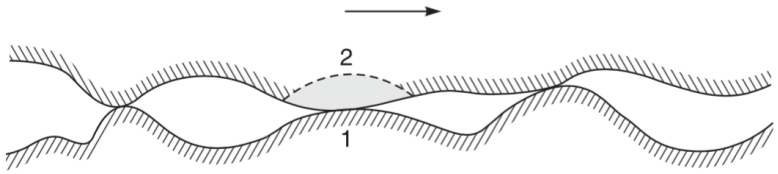


**Figure 1.17**: Schematic showing two possibilities of break (1 and 2) during shearing of an interface. In most cases, the break during shearing occurs at the interface (path 1), because the interfacial adhesion strength is expected to be small as compared to the breaking strength of the material. On the other hand, break may occur in one of the two asperities (path 2) and a small fragment may become attached to the other surface. Taken from Ref. [94].

### 1.5.2 Abrasive Wear

Abrasive wear, on the other hand, is the detachment of material from a surface due to the invasion of hard particles. Two types of damage are imposed on the wearing surfaces, namely plastic deformation or brittle fracture [94]. The type of damage on a surface is very closely related to the removal process, and is a function of the ductility of the surface being abraded. When the wearing material is ductile, it can be removed by plastic deformation related mechanisms. Increasing the hardness of the surface will reduce the volume loss. However, when the wearing surface is brittle, the removal occurs primarily through surface cracking; accordingly, the fracture toughness of the material may play a more important role than hardness.

There are two general situations for abrasive wear, as shown in Fig. 1.18. In the first case, two-body abrasion, a harder surface is rubbing against a softer surface [94]. This situation occurs in operations such as grinding, cutting and machining. In the second case, three-body abrasion, small particles of a harder abrasive sandwiched between two other surfaces, abrade one or both of the surfaces. In many cases, the wear mechanism

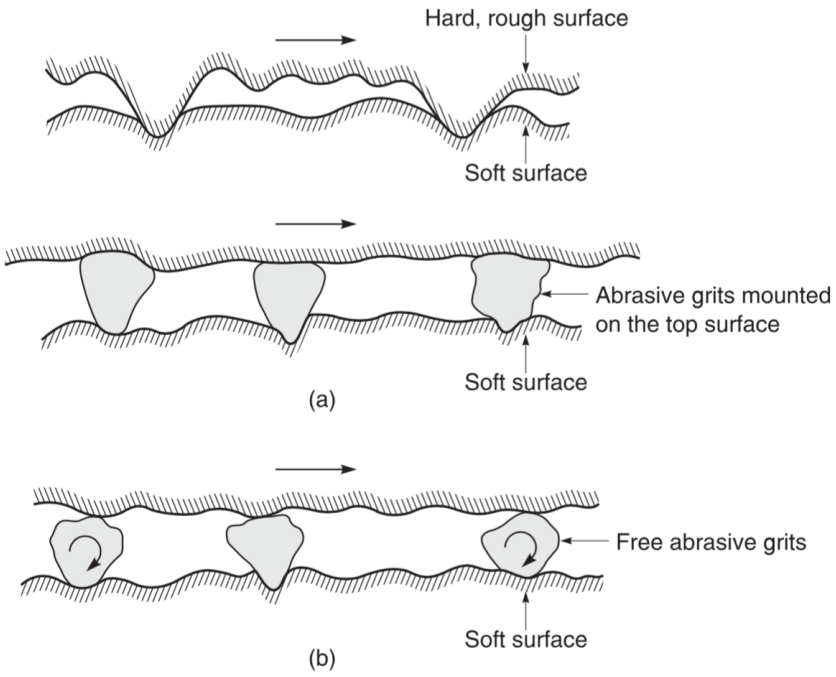


**Figure 1.18**: Schematics of (a) a rough, hard surface or a surface mounted with abrasive grits sliding on a softer surface, and (b) free abrasive grits caught between the surfaces with at least one of the surfaces softer than the abrasive grits. Taken from Ref. [94].

initiates as adhesive, generates wear particles and leads to three-body abrasion [95].

### 1.5.3 Archard's Wear Law

Due to the complicated nature of wear, equations and models to predict wear are typically limited to specific materials and working conditions. The most successful and widely used law was proposed by Archard in 1953 [96]. Archard's wear law states that the wear rate (defined as material's volume loss divided by sliding distance) is directly proportional to the applied load and inversely proportional to the hardness:

$$V_w = k \frac{SN}{H} \tag{1.12}$$

where $V_w$ is the total volume of material removed by wear, $k$ is the dimensionless wear coefficient, $N$ is the applied normal load, $S$ is the sliding distance and $H$ is the material hardness [97]. The relationship was developed based on the behavior of crystalline metals, but has also been shown to describe the behavior of ceramics and even some BMGs, as shown in Fig. 1.19 [98].

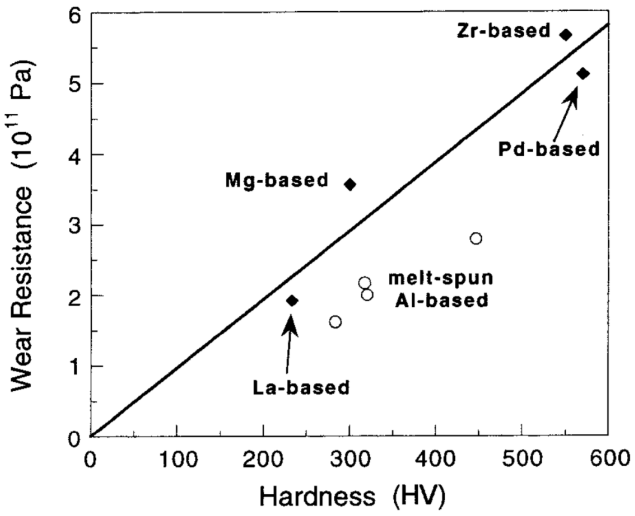


**Figure 1.19**: Correlation of abrasive wear resistance with hardness for different bulk metallic glasses and melt spun amorphous ribbons. The data suggests that bulk metallic glasses follow Archard's wear law. Taken from Ref. [98].

Hardness is quite often the property used for measuring the wear resistance of metals. While in general this principal works, applying it across the board can lead to some catastrophic results. In a macro hardness test, the size of this impression is quite a bit larger than any of the individual grains or hard particles. Essentially this hardness test is measuring the average hardness of many particles. On the other hand, a micro-hardness test measures the hardness of individual grains or particles. Furthermore, in the case of extremely hard or brittle materials, the fracture toughness generally affects the wear rate,

but this is not accounted for in Archard's wear equations. For a material combination with primarily elastic contacts, the wear rate generally decreases with an increase in the modulus of elasticity [94].

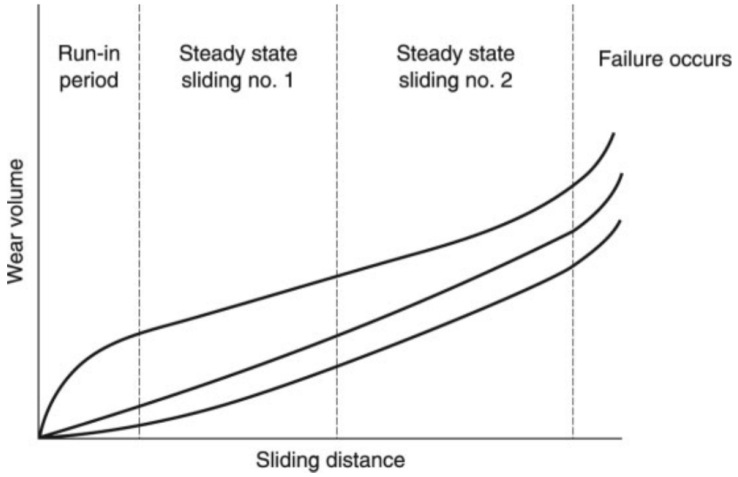


**Figure 1.20**: Three hypothetical cases of wear volume as a function of sliding distance showing run-in, steady-state and failure regions. Taken from [94].

The wear process is generally quantified by wear rate, or the volume loss of material removed per unit time or per unit sliding distance. Other measures could be dimensionless, such as the depth of material per unit sliding distance, or the volume removed per apparent area of contact and per unit sliding distance. Regardless of the quantification method, wear rate is not constant, but rather, a complex function of time. Wear rate may start low and later rise, or vice versa, as shown in Fig. 1.20. The initial period during which wear rate changes is known as the run-in or break-in period. At a certain point, the wear rate transitions to a steady-state wear rate, and this rate may change if a transition from one mechanism to another takes place. Finally, the wear becomes so severe that failure occurs.

## 1.6 Aims and Objectives

Bulk metallic glasses (BMGs) present a unique challenge for materials scientists because there is no "structure" that can be used to make systematic processing–structure–property relationships. Furthermore, the rapidly quenched metastable state of BMGs leads to mechanical properties that are highly correlated to processing and difficult to characterize. Because of this, BMGs have been slow to emerge as a structural engineering material, despite their promising mechanical properties and interesting manufacturing capabilities. The following studies address some of the most pressing hurdles that must be overcome before BMGs can be implemented in engineering designs.

Since the mechanical properties of BMGs are so strongly tied to their composition and processing, it becomes imperative to rigorously test them in their intended engineering environment of a promising specific applications. In Chapter 2, BMGs are investigated in systematic study for highly wear-resistant gears. The main goal of this work is to develop a BMG that can reliably outperform current state-of-the-art gear materials. Comprehensive pin-on-disk wear testing is conducted for over 40 different amorphous alloys in order to identify the most wear-resistant BMG system. Additional custom gear-on-gear testing is used to test select alloys under a specific environment and to compare the wear performance with currently used gear materials. Thermal, physical and mechanical properties are determined and used to describe the wear performance, and a new manufacturing methods for casting net-shaped macroscale gears is considered.

Chapter 3 includes an investigation into the notch toughness of a wear-resistant

$Cu_{43}Zr_{43}Al_7Be_7$ bulk metallic glass. Small fractions of crystalline regions are identified in the alloy, which are thought to lead to the interesting mechanical properties and excellent wear behavior. X-ray diffraction (XRD), energy dispersive X-ray spectroscopy (EDS), electron backscatter diffraction (EBSD) and Vickers' hardness are used to characterize the structure and properties of the in-situ composite. Four-point-bend notch toughness testing shows that the notch toughness correlates well with the composition of the matrix. Furthermore, the XRD operating parameters are described in detail in order to ensure that a partially crystalline alloy can be correctly characterized.

In Chapter 4, a low-cost variant of a partially-crystalline $Cu_{43}Zr_{43}Al_7Be_7$ BMG is investigated by introducing low-purity zirconium. Furthermore, a large commercial-scale synthesis process is also compared. The alloys are evaluated based on glass-forming-ability and toughness, and toughness is characterized based on the composition of the amorphous matrix. Furthermore, a Weibull analysis is provided in order to compare the reliability of high purity $Cu_{43}Zr_{43}Al_7Be_7$ produced commercially and produced in a laboratory.

# 2 Optimizing Bulk Metallic Glasses for Robust, Highly Wear-Resistant Gears

## 2.1 Abstract

Despite their promising mechanical properties and ability to be manufactured like plastics, bulk metallic glasses (BMGs) are slow to emerge as a structural engineering material. As with any new material entering the commercial market, the process of adoption is complex, especially if the material is radically different from alternative materials in terms of manufacturing and performance. Widespread use of BMGs has been limited for exactly these reasons. BMGs typically exhibit more than double the tensile strength of their crystalline constituents, but suffer from brittle fracture and a nearly complete lack of ductility. BMGs are very hard and difficult to machine, but can also be injection-molded using technology similar to plastics, allowing for mass production of complex hardware.

Despite these unique properties, the most confounding aspect of using BMGs in structural applications is the realization that rapidly quenched BMGs are metastable solids with mechanical properties highly correlated to the configurational state of the glass, which is, unfortunately, also highly correlated with composition and manufacturing. As such, it becomes imperative to develop promising applications for BMGs, such as gears, and then rigorously test them in their intended engineering environment. This allows for changes in performance to be correlated with composition and manufacturing, ultimately leading to a strategy for implementation. In the current work, pin-on-disk wear testing is used to identify a class of Cu-Zr-based BMGs that exhibit excellent wear performance compared to other BMGs. Centimeter-scale gear-on-gear test show that Cu-Zr-based BMGs exhibit only about 40% of the wear loss, as compared to an often used steel, Vascomax C300. The results demonstrate that when BMGs are designed specifically for gear use, they can exhibit wear properties that compete with, and even potentially surpass, state-of-the-art engineering materials. Furthermore, as the notch toughness decreases, the performance of macroscale gears transitions from extremely low abrasive wear to catastrophic gear fracture. In order to optimize the wear performance of Cu-Zr-based BMG gears, toughness should be maximized. This differs from the conventional strategy used to develop wear-resistant crystalline alloys, where wear performance increases with increasing hardness. Finally, a new low-cost manufacturing method for casting net-shaped macroscale gears is developed.

## 2.2 Introduction

Gear wear, especially in harsh environments, severely restricts the service life of mechanical systems and currently pushes the limits of existing materials. This presents a serious challenge for implementing gears in spacecraft, for example, which must be designed to withstand extreme space environments throughout the vehicle's lifetime. Cryogenic vacuum operation has long been a design challenge for gear lubrication, which has conventionally required heating a grease lubricant. For example, NASA's recent Mars Science Laboratory (MSL) rover, Curiosity, expends one third of its energy to heat gear lubricant prior to mobile operations. Curiosity is equipped with gears machined from a nitrided maraging steel, Vascomax C300, but still requires the use of heated lubricant to operate at Mars' low temperatures. Steel is the most widely used gear material, but it has poor wear resistance when unlubricated or dry lubricated and is further limited by its relatively high minimum operating temperature range [93]. Ceramic gears generally exhibit far better wear resistance than steel, but they are difficult and expensive to manufacture, and they are prone to failure by catastrophic brittle fracture due to their extremely low fracture toughness (less than 10 MPa-$m^{1/2}$ for all engineering ceramics, with typical values around 1 MPa-$m^{1/2}$) [99, 100].

Bulk metallic glasses (BMGs) are a broad class of metal alloys that, when quenched rapidly from the melt, are able to avoid crystallization and retain an amorphous microstructure. This imparts several advantageous properties that would suggest BMGs are ideal materials for gears: high hardness, low modulus of elasticity, large

elastic strain limit, high strength, and the absence of dislocation-based plasticity [101]. Furthermore, bulk metallic glass matrix composites (BMGMCs), or BMGs reinforced with soft crystalline phases, also have the potential to act as high-performance structural materials due to their high toughness and ductile failure [102]. This paper investigates the wear-resistance of both BMGs and BMGMCs to determine their potential suitability for use as gears.

Tribological studies on BMGs have, for the most part, been focused on material hardness [103–105]. This is because, for crystalline metals, the sliding wear-resistance is roughly proportional to the materials hardness [97]. Literature on the wear resistance of BMGs tends to show promising results as hardness increases [103], but it is clear that in some situations, hardness is not sufficient to describe wear behavior [98, 106]. Although many tribological studies of BMGs have acknowledged the role of toughness, few have measured it. The most comprehensive study to date shows that the sliding wear behavior of annealed Cu-Hf-based BMGs is entirely hardness controlled until the BMG falls below a critical toughness of about 32 MPa-$m^{1/2}$ [107]. In select cases, the use of BMGs (and thinner amorphous metal coatings) in wear-resistant applications is well-established. For example, due to ultra-high hardness and ease of deposition through high velocity oxygen fuel (HVOF) and plasma thermal spray coatings, amorphous metal coatings on steel have been widely used in hardbanding applications in the oil and gas industry [108]. Moreover, BMG gears with diameters on the order of 100 $\mu$m have been fabricated and even run in gearboxes designed for microelectronic devices (MEMS) [104]. Unfortunately, the thermoplastic forming process used to create such gears becomes difficult with increasing

gear size. Furthermore, roller bearings of 7.5 mm in diameter were fabricated from $Zr_{41.2}Ti_{13.8}Cu_{12.5}Ni_{10}Be_{22.5}$ (Vitreloy™[1]) and when integrated into a bearing, their wear compared favorably with steel [109]. For the most part, functional testing of BMGs has been limited to microscale structures or test samples with generic geometries. What is lacking is a new fabrication process and wear testing method to successfully fabricate and evaluate centimeter-scale BMG gears across multiple alloy systems.

In this study, the wear performance of centimeter scale BMGs is investigated using both standard pin-on-disk wear testing and custom spur gear-on-gear testing. In both cases, the wear loss of the BMG material is evaluated in terms of the mechanical properties such as hardness, shear modulus, and notch toughness. BMG test specimens of over 30 different compositions were fabricated and tested in this wear study and promising alloys were then manufactured and tested in centimeter scale spur gears fabricated through suction casting.

## 2.3 Materials and Methods

The BMG compositions presented in this study were limited to BMGs with significant glass-forming-ability, such that bulk amorphous disks could be fabricated for wear testing and gear fabrication. Additionally, practical manufacturing constraints limited alloy selection to those amenable to suction casting in a vacuum arc-melter. For example, alloys containing phosphorus were synthesized, but could not be cast due to the

[1]Liquidmetal® Technologies, 30452 Esperanza, Rancho Santa Margarita, CA 92688.

evaporation of phosphorus during arc-melting. Precious metal BMGs (such as Pd, Ag, Au and Pt), as well as exotic BMGs (such as Ca, Mg, La and Sc) were also not considered due to a perceived lack of engineering suitability in terms of cost, mechanical properties, and reactivity. Thus, the comprehensive pin-on-disk wear testing in this work includes BMG and BMGMC compositions based in CuZr, Ni, Fe, Ti, and Zr. This selection incorporates alloys selected from literature, alloys previously developed by the authors, and alloys developed as part of this study through iterative compositional adjustments. A complete list of the alloys investigated in the pin-on-disk study is given in Table 2.1, along with the critical casting diameter reported in the literature (when available) and the corresponding reference.

**Table 2.1**: List of BMG and BMGMC alloys studied in pin-on-disk wear test, reported critical casting diameter and corresponding reference, and structure of 25 mm diameter and 3 mm thick pin-on-disk sample as measured by XRD. The structure of the sample is reported by "A" for amorphous, "C" for ductile phase-containing composite and "X" for partially or mostly crystalline.

| Alloy | $d_c(mm)$ | Ref. | Structure |
|---|---|---|---|
| $Cu_{50}Zr_{50}$ | 2 | [108] | X [a] |
| $Cu_{47.5}Zr_{48}Al_4Co_{0.5}$ | – | [110] | C [b] |
| $Cu_{47}Zr_{46}Al_7$ | 3 | [43] | X |
| $Cu_{47}Zr_{46}Al_5Y_2$ | – | – | A [c] |
| $(Cu_{47}Zr_{46}Al_5Y_2)Nb_3$ | – | – | A |
| $Cu_{44}Zr_{44}Al_7Ni_5$ | – | – | C |
| $Cu_{44}Zr_{44}Al_7Be_5$ | – | – | A |
| $Cu_{44}Zr_{44}Al_5Ni_3Be_4$ | – | – | A |
| $Cu_{43}Zr_{43}Al_7Ag_7$ | 8 | [74] | C |
| $Cu_{43}Zr_{43}Al_7Be_7$ | 12 | [74] | A |
| $(Cu_{44}Zr_{44}Al_7Be_5)Nb_3$ | – | – | A |
| $Cu_{42}Zr_{41}Al_7Be_{10}$ | – | – | A |
| $Cu_{42}Zr_{41}Al_7Be_7Cr_3$ | – | – | A |
| $Cu_{42}Zr_{41}Al_7Be_7Co_3$ | – | – | A |
| $(Cu_{43}Zr_{43}Al_7Be_7)Nb_3$ | – | – | A |

**Table 2.1**: List of BMG and BMGMC alloys studied in pin-on-disk wear test, reported critical casting diameter and corresponding reference, and structure of 25 mm diameter and 3 mm thick pin-on-disk sample as measured by XRD (continued).

| Alloy | $d_c(mm)$ | Ref. | Structure |
|---|---|---|---|
| $Cu_{41}Zr_{40}Al_7Be_7Co_5$ | – | – | C |
| $(Cu_{42}Zr_{41}Al_7Be_{10})Nb_3$ | – | – | A |
| $Cu_{40}Zr_{40}Al_{10}Be_{10}$ | – | – | A |
| $Ni_{57}Zr_{18}Ti_{14}Si_2Sn_3Be_6$ | – | – | X |
| $Ni_{56}Zr_{17}Ti_{13}Si_2Sn_3Be_9$ | – | – | X |
| $Ni_{40}Zr_{28.5}Ti_{16.5}Be_{15}$ | – | – | X |
| $Ni_{40}Zr_{28.5}Ti_{16.5}Cu_5Al_{10}$ | – | – | X |
| $Ni_{40}Zr_{28.5}Ti_{16.5}Cu_5Be_{10}$ | – | – | X |
| $Fe_{60}Sn_1Y_2Zr_8Co_5Cr_2Mo_7B_{15}$ | – | – | X |
| $Fe_{59.8}Sn_{1.2}Y_2Zr_8Co_5Cr_2Mo_7B_{15}$ | – | – | X |
| $Fe_{48}Cr_{15}Mo_{14}Er_2C_{15}B_6$ | 12 | [111] | X |
| $Fe_{48}Cr_{15}Mo_{14}Y_2C_{15}B_6$ | 9 | [111] | X |
| $Fe_{41}Co_7Cr_{15}Mo_{14}Y_2C_{15}B_6$ | 16 | [112] | X |
| $Ti_{45}Zr_{16}Ni_9Cu_{10}Be_{20}$ | 10 | [113] | A |
| $Ti_{40}Zr_{25}Ni_8Cu_9Be_{18}$ | 10 | [114] | A |
| $Ti_{40}Zr_{25}Be_{30}Cr_5$ | 8 | [6] | A |
| $Ti_{33.18}Zr_{30.51}Ni_{5.33}Be_{22.88}Cu_{8.1}$ | – | – | A |
| $Zr_{65}Cu_{17.5}Al_{7.5}Ni_{10}$ | 16 | [4] | A |
| $Zr_{58.5}Cu_{15.6}Ni_{12.8}Al_{10.3}Nb_{2.8}$ (Vitreloy 106) | 10 | [115] | A |
| $Zr_{55}Cu_{30}Al_{10}Ni_5$ | 8 | [116] | A |
| $Zr_{55}Al_{20}Co_{25}$ | 2.5 | [117] | C |
| $Zr_{52.5}Ti_5Cu_{17.9}Ni_{14.6}Al_{10}$ (Vitreloy 105) | 10 | [118] | A |
| $Zr_{41.2}Be_{22.5}Ti_{13.8}Cu_{12.5}Ni_{10}$ (Vitreloy) | 22 | [3] | A |
| $Zr_{36.6}Ti_{31.4}Nb_7Cu_{5.9}Be_{19.1}$ (DH1) | – | [102] | C |
| $Zr_{35}Ti_{30}Cu_{8.25}Be_{26.75}$ (GHDT) | 28 | [119] | A |

[a] Predominantly amorphous with crystalline inclusions.
[b] Bulk metallic glass matrix composite (BMGMC).
[c] Fully amorphous.

For the alloys listed in Table 2.1, constituent high purity elements were arc-melted together and then suction cast into 25 mm diameter and 3 mm thick disks using water-cooled copper molds under purified argon atmosphere. The pure elements used had purities between 99.5–99.9%. X-ray diffraction (XRD) was used to assess the predominant atomic structure of each as-cast sample. Each alloy was shown to exhibit

one of the three primary structures, also reported in Table 2.1: fully amorphous (A), partially or mostly crystalline (X), or ductile-phase-toughened bulk metallic glass matrix composites (C).

Pin-on-disk wear testing was performed according to ASTM G99 [120]. Fig. 2.1a shows a representative photograph of an as-cast BMG disk, which was cast from the melt in an arc-melter (the casting temperature is unknown, but is ¿2000K). Prior to wear testing, the casting gates were trimmed and the surface on both sides of the disk was polished to 1200 grit. The samples were rotated at 160 rpm, with a point force placed 9.8 mm from the center. The point force was a 4.8 mm diameter 304L stainless steel ball bearing exerting a normal force of 1 N and covered a total distance of 1.2 km over the course of 120 min in open air with no lubrication. The mass of each sample was measured before and after testing, and the net volume loss was calculated using measured densities for a wear performance comparison across different alloy compositions. A pin-on-disk test after wear testing is shown in Fig. 2.1b, with visible wear debris accumulated near the edges of the test fixture, and a schematic of the setup is shown in the inset. The variation in wear-resistance was further characterized by inspection of the wear track. The wear track depth profile was measured using a Mitutoyo Surftest SJ-210 surface roughness tester and characterized by the maximum profile valley depth ($R_m$). For comparison, optical top-down images were taken from the same location on the wear track. Vickers' hardness measurements were taken with a Leco LM247 microhardness tester using a 2 kg load and a 10 s dwell time. A surface polish of 1200 grit proved adequate to accurately measure the Vickers' indents and identify if the indents induced cracking in some of

the more brittle compositions. Reported hardness values represent the averages of at least three measurements taken in different locations of the sample to account for local variability.

Based on the initial pin-on-disk wear screening, select alloys were chosen for gear-on-gear testing. The purpose of gear-on-gear testing was to show whether or not the wear behavior in the pin-on-disk testing would be comparable for the complex loading conditions of an actual gear. Initial spur gears were cut by wire electrical discharge machining (EDM) from samples with the same cylindrical geometry as those used for pin-on-disk testing. The gears had a 16.9 mm outer diameter, and a 9.5 mm diameter hole with a key slot used to drive the gears in the gear rig. Fig. 2.2a shows the customized gear-on-gear test setup, which runs two identical gears—one gear was connected to a speed controlled motor and torque sensor, and one gear was connected to an electrically controlled brake to enable constant loading of the gears. The gears were run without lubricant at a rotational speed of 4100 rpm and 10 N-m torque. After a 10 min run-in period to remove any debris from the surface, each test was run continuously for 180 min. Similar to the pin-on-disk testing, volume loss—calculated from mass loss—was used as a quantitative measure of wear performance. After testing, light optical microscope images of the gear-tooth profiles were taken in both bright field and dark field modes and scanning electron microscope (SEM) images were taken at 20 kV.

Various iterations of $(Cu_{50}Zr_{50})_{100-x-y}Al_xBe_y$ (for x=3, 5, 7 and y=3, 5, 7, 10) were fabricated and tested in order to investigate the variance in toughness of this highly wear-resistant alloy system. Four-point bend notch toughness tests were carried out

on copper-mold suction cast 3 mm diameter rods using a screw-driven 5980 Instron with a loading rate of 0.1 mm/min. The test setup followed ASTM E399 standard, and the test samples were confirmed to meet plane strain conditions based on the plastic zone size constraint [121]. A notch was cut in the center of each rod using a low speed diamond saw to a depth 0.4–0.5 times the diameter with a root radius of 90 $\mu$m. The notch toughness was calculated using Kiuchi's bending stress equation for a notched round rod [122]. Furthermore, the elastic and thermal properties of the notch toughness samples were measured to evaluate the toughness using well-established trends, which will be discussed in more detail later [60, 123]. The elastic constants were determined through ultrasonic measurements by assuming the linear elastic relations for isotropic materials. Thermal parameters, such as the glass transition temperature ($T_g$), the crystallization temperature ($T_x$), and the liquidus temperature ($T_l$), were measured using a Perkin-Elmer Diamond DSC in a purged argon atmosphere with a heating rate of 0.33 K/s.

Finally, due to the high cost of machining each spur gear for testing, the authors developed a method for net-shape suction casting of BMG gears [124]. The method is intended to demonstrate the speed and flexibility of using net-shaped suction casting for manufacturing parts that do not require any post-machining. To cast and run gears without post machining, three features were required: (1) a one-piece gear-tooth mold with extrusion symmetry for preventing parting lines on the gears and allowing the gear to be pressed out, (2) concentric axles that can be connected to the bearings to run the gears at a constant contact stress, and (3) an extruded key or keyway that can be used to drive the gear.

## 2.4 Results

### 2.4.1 Sample Fabrication

In this study, only alloy compositions with high glass-forming-ability (GFA) were considered so that actual gears could be manufactured from promising alloys. Even so, fabrication of a 25 mm diameter, 3 mm thick disk via vacuum arc-melting and copper mold suction casting proved challenging with most alloy systems. Some BMG compositions were successfully alloyed and cast, but due to their brittle nature, cracked repeatedly during multiple attempts at removal from the mold. This was especially true of all Fe-based alloys, including $Fe_{48}Cr_{15}Mo_{14}Er_2C_{15}B_6$ and $Fe_{41}Co_7Cr_{15}Mo_{14}Y_2C_{15}B_6$, which have been reported to have significant GFA at 12 mm and 16 mm, respectively [111, 112]. Thus, because the Fe-based alloys lacked the toughness to survive the manufacturing process, data from the Fe-based alloys could not be obtained and is not included in the results. On the other hand, five Ni-based BMGs were successfully cast into the required cylinder. Although X-ray diffraction analysis showed them to be predominantly crystalline, they were still included in the pin-on-disk analysis.

### 2.4.2 Pin-on-Disk Testing

The results of the comprehensive pin-on-disk study show that not all BMG compositions have good tribological properties. The pin-on-disk test data, plotted as volumetric wear loss versus Vickers' hardness, for all alloys successfully cast into amorphous, composite, or crystalline disks, is shown in Fig. 2.1c. Alloys that are

predominantly crystalline are shown as open data points, and alloy compositions designed as, and confirmed to be, BMGMCs are shown as half open data points. Wear loss in Zr- and Ti-based BMGs was either good (0.2–0.4 $mm^3$) or very poor (greater than 0.6 $mm^3$). On the other hand, wear loss from Cu-Zr- and Ni-BMGs was extremely low (less than 0.15 $mm^3$) with little variation across different compositions in the same system. Vascomax C300 exhibited the least amount of wear loss (a minimal 0.025 $mm^3$).

The difference in wear performance between different BMGs is easily discerned with an inspection of the track after testing. Fig. 2.1d shows the wear track profile, the corresponding maximum profile valley depth, $R_m$, and a top-down optical micrograph of the wear track for select alloys. Fig. 2.1e shows the linear correlation between the pin-on-disk wear loss and $R_m$. It is interesting to note that GHDT—a composition known for its benchmark toughness and thermoplastic forming ability—has particularly poor wear-resistance. This result would seem to contradict often-touted notions that all BMGs are hard and therefore have good wear resistance [125–127]. Like their crystalline alloy counterparts, BMGs as a class of materials do not exhibit monolithic properties, but rather have a broad range of possible properties based on composition.

### 2.4.3 Gear-on-Gear Testing

Initially, five alloys were selected for gear-on-gear testing to show a range of performance across alloy systems. Table 2.2 lists the alloys along with their density and volume loss after 180 min of unlubricated gear testing. It is important to reiterate that all the Ni-based alloys studied in the pin-on-disk tests were found to be predomi-

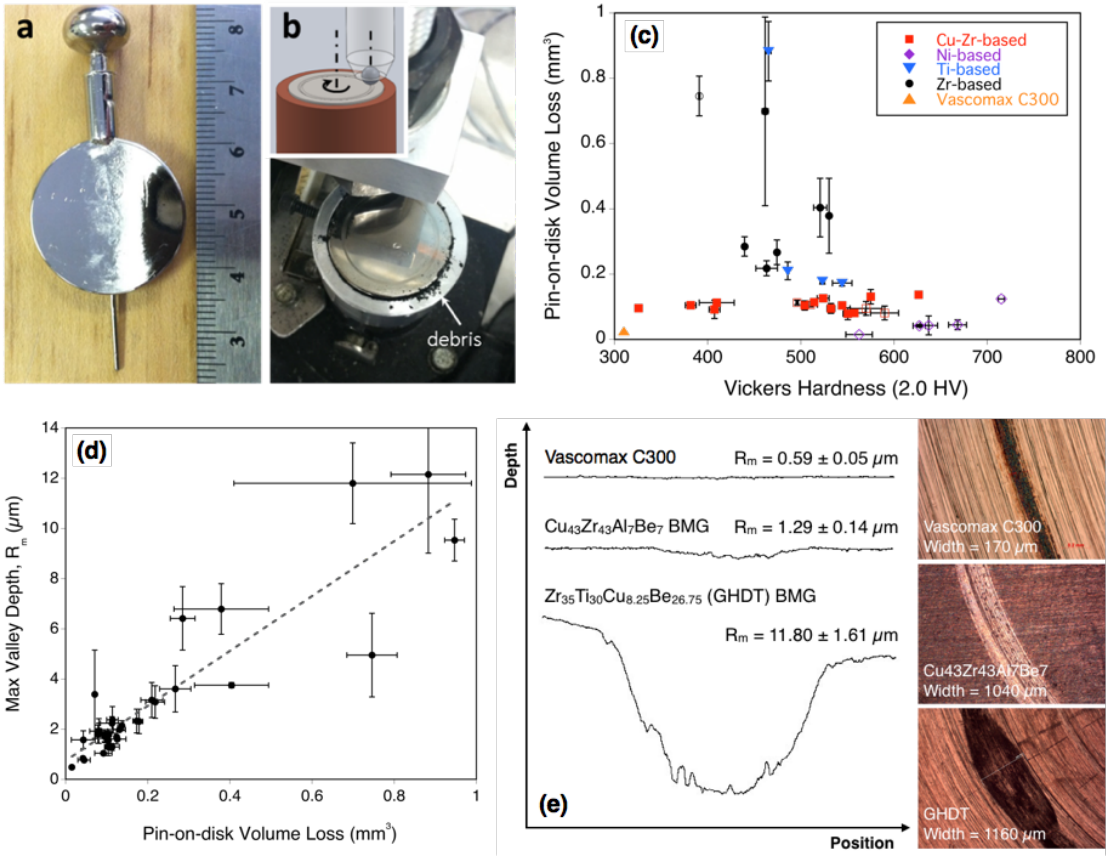


**Figure 2.1**: Pin-on-disk wear testing of BMGs. (a) Photograph of a 25 mm diameter 3 mm thick as-cast BMG disk before the gates are trimmed. (b) Photograph of a mounted sample after a pin-on-disk test showing wear debris. A schematic of the setup is shown in the inset. (c) Plot of pin-on-disk volume loss versus Vickers' hardness for various BMG alloys. The open data points represent bulk metallic glass matrix composites (BMGMCs). (d) Plot showing the linear relationship between pin-on-disk volume loss and the maximum profile valley depth, $R_m$, of the wear track. (e) Comparison of the wear tracks after pin-on-disk testing for different alloys; including the wear track depth profile, the corresponding $R_m$, and a top-down micrograph of the wear track.

nantly crystalline after casting. Despite their superb wear performance, crystallization severely decreased the toughness of these alloys and prevented them from successfully being EDMed into gears. All the plates fractured immediately when contacted with the machining wire.

In general, the results from the gear-on-gear testing track those from the pin-

**Table 2.2**: Gear-on-gear wear loss data for selected BMG alloys and one BMGMC (DH1). Note that the volume loss from $Cu_{43}Zr_{43}Al_7Be_7$ is less than 40% of the volume loss from Vascomax C300 steel.

| Alloy | Density (g/cm$^3$) | Volume loss (mm$^3$) |
|---|---|---|
| $Zr_{36.6}Ti_{31.4}Nb_7Cu_{5.9}Be_{19.1}$ (DH1) | 5.70 | 25.8 [a] |
| $Zr_{35}Ti_{30}Cu_{8.25}Be_{26.75}$ (GHDT) | 5.39 | 28.0 |
| Vascomax C300 | 8.0 0 | 6.04 |
| $Cu_{47}Zr_{46}Al_5Y_2$ | 7.00 | 3.76 |
| $Cu_{43}Zr_{43}Al_7Be_7$ | 6.81 | 2.64 |

[a] Test stopped after 1.5 hours.

on-disk testing. BMGs exhibiting poor wear resistance in pin-on-disk testing typically also performed poorly in gear-on-gear wear testing. The monolithic BMG, $Zr_{35}Ti_{30}Cu_{8.25}Be_{26.75}$ (GHDT), lost 28.0 mm$^3$ after 180 min of testing and the BMG composite, $Zr_{36.6}Ti_{31.4}Nb_7Cu_{5.9}Be_{19.1}$ (DH1), lost nearly the same amount, 25.8 mm$^3$, after only 90 min. GHDT is a very tough monolithic BMG, while DH1 is an ultra-tough BMG matrix composite with significant ductility in tension [102, 119]. Fig. 2.2b shows optical micrographs from the nominal $Cu_{43}Zr_{43}Al_7Be_7$ BMG before and after gear-on-gear testing, in both isometric and profile views. After a 10 min run-in period and 180 min of unlubricated testing, only a small region of wear scarring is visible. In contrast, Fig. 2.2c shows micrographs from Vascomax C300 gears after being tested under the same conditions. A clear notch is visible on the leading edge of the gear teeth in both perspectives. Line profiles of $Cu_{43}Zr_{43}Al_7Be_7$ and Vascomax C300 gear teeth were extracted using ImageJ photo editing software, as shown in Fig. 2.2d. The reduction in area of the Vascomax C300 gear teeth is 11.3%, while $Cu_{43}Zr_{43}Al_7Be_7$ only lost 3.9% of its area. The isometric views of the gear teeth for GHDT and DH1 are shown in

Fig. 2.2e, where the gear tooth profile is almost completely ground away, leaving a point. In total, the initial gear testing for a variety of alloys demonstrates a significant variance in the wear loss properties, primarily between Cu-Zr-based BMGs and other alloys. Conventional Zr-based BMGs typically used in the casting of net-shaped parts exhibit very poor wear performance as macroscale gears, as do highly toughened BMGMCs. In contrast, Cu-Zr-based alloys (both Be and non-Be bearing) exhibited superior wear loss to Vascomax C300 gears under the identical testing conditions.

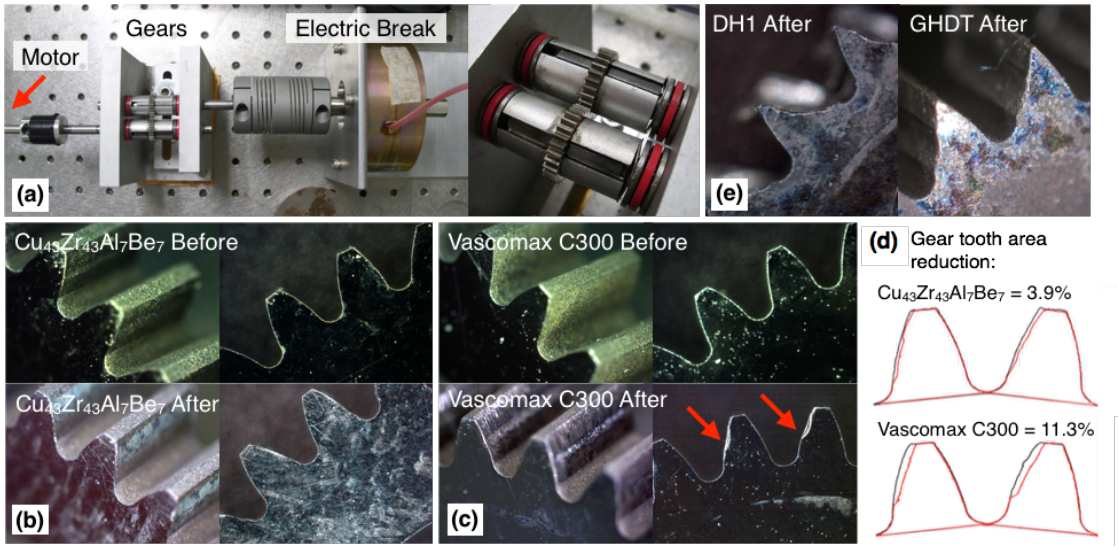


**Figure 2.2**: BMG spur gear-on-gear wear tests. (a) The gear-on-gear test rig at NASA JPL/Caltech for testing spur gears, and a close-up image of the BMG gears installed in the test rig. (b) Images before and after wear testing a $Cu_{43}Zr_{43}Al_7Be_7$ BMG showing virtually no damage to the gears. (c) Vascomax C300 before and after wear testing, showing severe scuffing wear on the gear teeth. (d) Line profiles, created using photo editing software, showing a clear comparison between the wear rate of $Cu_{43}Zr_{43}Al_7Be_7$ and Vascomax C300. (e) Images after wear testing a BMG composite, $Zr_{36.6}Ti_{31.4}Nb_7Cu_{5.9}Be_{19.1}$ (DH1), and a monolithic BMG, $Zr_{35}Ti_{30}Cu_{8.25}Be_{26.75}$ (GHDT). Both alloys are notable for their high toughness and were also damaged so severely by the wear test that sharp points are all that remain of the gear teeth.

The initial gear testing, while informative, does exhibit some drawbacks. Each of the gears had to be machined from plates using wire EDM, which is not only expensive,

but imparts a rough, recast layer on the surface of the gears (this can be seen in Fig. 2.2b and Fig. 2.2c). Moreover, each gear was machined with a center-hole and a sharp notch so that the gears could be driven in a gear tester. These sharp features caused the occasional fracture of the gears and added extra machining expense. As will be shown later, a process for casting fully net-shaped gears is required to reduce the manufacturing cost as well as the performance of the BMG gears.

### 2.4.4 Notch Toughness Testing

It is clear from both the pin-on-disk study and the gear testing that Cu-Zr-based BMGs tend to exhibit exceptional wear resistance. During that work, it was identified that optimal combinations of glass forming ability, wear loss and toughness were achieved in the CuZrAlBe system where the Cu:Zr ratio remains nearly 1:1. Similar alloys have been developed from Cu-Zr-based systems, but have not yet been applied to gear systems [128]. In the current work, it was noticed that by varying the contents of Al and Be in the composites between 3–10 at% independently, the notch toughness and the glass forming ability of the alloys could be tailored. Considering that this entire system was shown to have excellent wear performance, the ability to change the toughness and the thickness of the alloy to be used in a gear is a powerful design tool for BMG gears. The observed trends are shown in Fig. 2.3 for nine alloys from this series, with Fig. 2.3a plotting notch toughness versus the ratio of glass transition temperature to the liquidus temperature, and Fig. 2.3b plotting the notch toughness versus the ratio of the shear modulus to the bulk modulus. The highest measured notch toughness corresponds to

$Cu_{46}Zr_{46}Al_3Be_5$ at 56 MPa-$m^{1/2}$. This alloy also has the lowest GFA of the series, with 3 mm rods being amorphous, but some crystal formation being detected in the larger geometry discs used for EDMed gears.

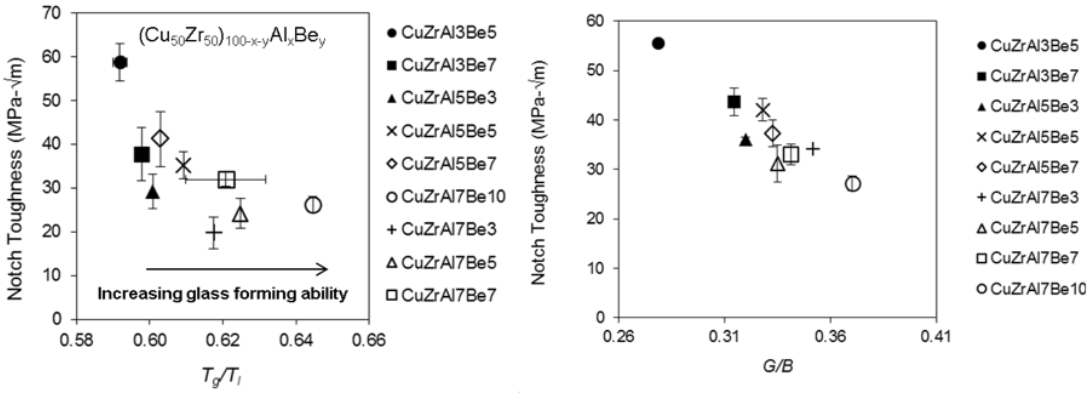


**Figure 2.3**: Cu-Zr-based BMGs as wear-resistant gear materials. (a) A plot of 4-point bend notch toughness versus $T_g/T_l$ showing how toughness of CuZrAlBe BMGs decreases with increasing glass forming ability. (b) A plot of notch toughness versus $G/B$ for CuZrAlBe BMGs showing that toughness is correlated with barrier to shear flow in the glass. These plots demonstrate that glass forming ability and gear wear can be tuned in CuZrAlBe alloys to create gears with desired performance.

Glass-forming-ability of BMGs is known to increase with increasing reduced glass transition temperature, $T_{rg}$, which is the ratio of the glass transition temperature, $T_g$, to the liquidus temperature, $T_l$, or $T_{rg} = T_g/T_l$ [123]. In the $(Cu_{50}Zr_{50})_{100-x-y}Al_xBe_y$ alloys investigated here, it is demonstrated that with increasing glass forming ability, the toughness decreases. This trend is expected based on previous trends in the literature. Another correlation between toughness and BMG properties is the ratio of the shear modulus, $G$, to the bulk modulus, $B$, which is generally considered a "brittleness factor" or a barrier to shear flow where, if $G/B < 0.41$, the alloy is considered intrinsically tough [60]. Here, the entire alloy series exhibit a ratio below this threshold with increasing notch toughness measured for lower ratios of $G/B$. The notch toughness measurements demonstrate that

the CuZrAlBe system has the ability to be *tuned* for a desired performance. This is a beneficial result for the fabrication of gears considering the variety of sizes, shapes and loads that gears must accommodate.

### 2.4.5 Net-Shaped Casting of BMG Gears

As mentioned previously, a major innovation in the testing of BMG gears requires the ability to fabricate gears rapidly, at low cost, without the need for post machining and without a rough surface from machining or wire EDM. The solution presented in this work was to develop a multi-piece suction casting mold, shown in Fig. 2.4a for rapidly casting gears from any BMG alloy with the critical design features of (1) perfectly formed, smooth teeth, (2) concentric axles to rotate the gears and (3) an external key for driving the gears. The three-piece mold, shown in Fig. 2.4a in the assembled form, and in Fig. 2.4b in the disassembled form, was developed to create gears with the same size and tooth profile as in Fig. 2.2, but with a castable geometry. The two outer pieces of the mold lock together with pins to align the shafts, while an EDMed inner mold contains the gear teeth profile. This design was required because the gear teeth could not exhibit a "parting line", which is formed on cast parts from a split mold. Instead, the BMG was cast into the cavity within the three parts, the outer pieces were removed, and the gear was pushed out of the central mold without damage, due to its extrusion symmetry. Fig. 2.4c shows a $Cu_{43}Zr_{43}Al_7Be_7$ BMG directly out of the mold and ready for testing. The mold is completely reusable and was used to cast all of the gears in the current study. Fig. 2.4d, shows a handful of gears that were cast in less than 4 hours using the same

mold, demonstrating the low-cost repeatability of the process. Through many iterations of attempting to suction-cast gears, it was determined that a low-pressure casting process (1–100 kPa) is necessary to ensure that the molds do not overfill and replicate the surface of the rough mold. As Fig. 2.4e demonstrates, some gears can be removed from the mold with a simple push of a finger. Not surprisingly, this low-pressure casting is actually expected to improve the wear performance of the gears by giving the teeth a smoother surface, which creates lower friction and less wear debris. Fig. 2.4f shows the rough surface of a BMG gear after wire EDM, Fig. 2.4g shows the textured surface of a steel gear that was machined, and Fig. 2.4h shows the smooth surface of a BMG gear that was cast. Notice that this latter gear has a smoother finish and slightly rounded corners due to the high surface tension of the molten BMG and the low-pressure casting procedure. A Keyence large depth-of-field microscope was used to measure both the profile and the surface roughness of BMG gear teeth, with the surface contour map and micrograph shown in Fig. 2.4i–j. The microscope was used to characterize the quality of the cast gears prior to testing by allowing for a large depth-of-field inspection of the teeth. Profile mapping was used to characterize variations in different gears to assess repeatability of the casting. More details on the inspection and quality control the BMG gears will be published later.

### 2.4.6 Relationship Between Toughness and Gear Performance

The ability to cast and test a large set of BMG gears allowed us to correlate the toughness of the BMG material with the wear loss. Fig. 2.5 shows the observed trend for

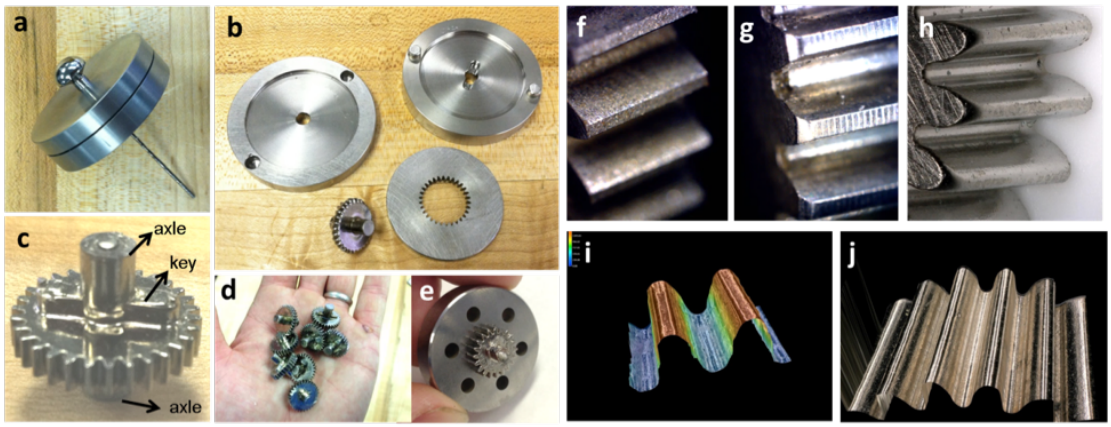


**Figure 2.4**: Low-cost, net-shape casting of macroscale BMG gears. (a) A three-piece gear mold after suction casting a BMG at pressures between 1–100 kPa. (b) The three pieces of the mold fit together with guide pins to create concentric axles. The gear is formed from a single middle piece to avoid parting lines in the teeth of the gears. (c) A $Cu_{43}Zr_{43}Al_7Be_7$ gear after casting showing the key used to drive the gears and the concentric axles. (d) Eight Ti-based BMG gears, all cast from the same mold. (e) A gear being pushed out of the mold using only finger pressure. (f) Enlargement of the surface roughness of a BMG gear that was fabricated from a plate using wire-EDM. (g) A been conventionally machined steel gear. (h) A suction cast BMG gear. (i-j) Optical surface images of the gear teeth measured using a large depth-of-field microscope with profile measuring capabilities.

Ti, Zr and Cu-Zr-based BMGs. As discussed previously, BMGs do not exhibit monolithic properties across all amorphous metals, as the literature often suggests. Instead, each BMG composition exhibits unique properties, such as toughness, wear loss and hardness. During gear testing, we discovered that many gears fractured unexpectedly. Fig. 2.5a shows an SEM image of a $Cu_{43}Zr_{43}Al_7Be_7$ BMG gear, where a crack has propagated through a gear tooth. In Fig. 2.5b, a crack at the root of a $Ti_{40}Zr_{25}Cu_9Ni_8Be_{18}$ BMG gear tooth resulted in the catastrophic fracture of the gear. Fig. 2.5c shows a plot of gear wear loss versus notch toughness for seventeen different alloys tested, along with a trend line. The wear loss for gears, which fractured during the testing, was set to an arbitrarily high value of 100 $mm^3/hr$, for visualization purposes. The Zr- and Ti-based

BMG compositions with very high notch toughness, averaging around 90 MPa-$m^{1/2}$, also exhibited significant wear loss, around 8–10 $mm^3/hr$. Cu-Zr-based BMGs exhibited very low wear rates and significantly lower notch toughness, ranging from 20–70 MPa-$m^{1/2}$. As toughness decreases, the wear performance improves until a critical minimum toughness is reached, at which point the gears begin to fail catastrophically by brittle fracture at the root. It is therefore postulated that the design of BMG spur gears is a judicious compromise between the gear-on-gear wear loss and the fracture toughness of the BMG material, as illustrated by the results in Fig. 2.5c. Designing BMG gears based on their toughness, as opposed to their hardness, is a significant departure in design compared to crystalline metals and is much more in-line with the design of ceramic gears. It should be noted that fatigue of the gears was not directly measured in this study, but also must play an important role in gear design. Future studies will address fatigue through gearbox life testing.

## 2.5 Discussion

### 2.5.1 Archard's Wear Equation

An important result of the pin-on-disk experiments, shown in Fig. 2.1c, is that all 18 Cu-Zr-based BMGs investigated in this study have excellent wear-resistance regardless of their Vickers' hardness. This result suggests that the wear-resistance of Cu-Zr-based BMGs cannot be described by Archard's wear law. Archard's wear equation predicts that

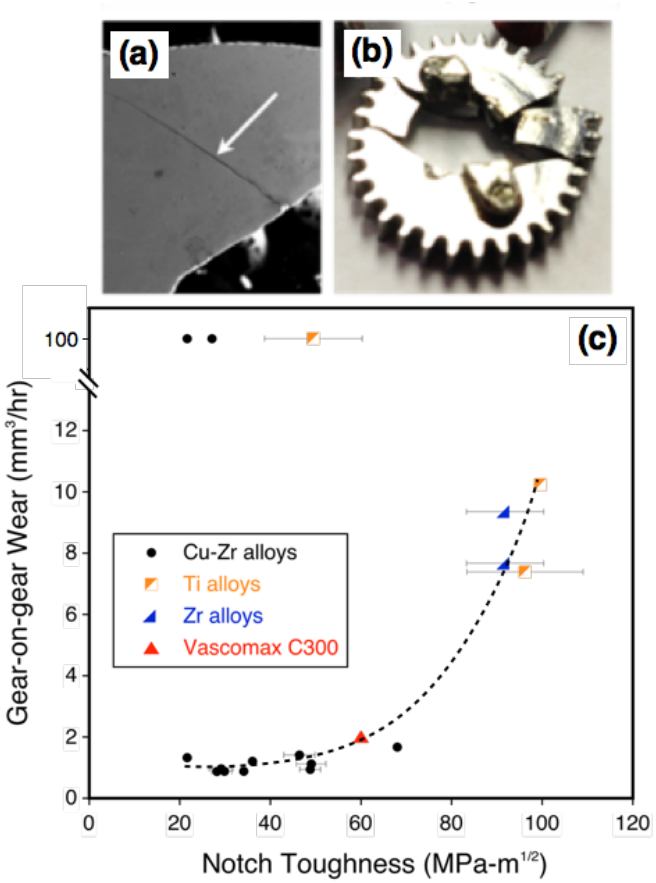


**Figure 2.5**: Role of toughness in BMG gear testing. (a) SEM image of a crack in the edge of a $Cu_{43}Zr_{43}Al_7Be_7$ BMG gear. (b) Catastrophic fracture of a $Ti_{40}Zr_{25}Cu_9Ni_8Be_{18}$ BMG gear. (c) Plot showing gear-on-gear wear rate versus notch toughness for different BMG systems and Vascomax C300. The wear loss of fractured gears was set to an arbitrary high value of 100 $mm^3/hr$.

the sliding wear loss is inversely proportional to the material hardness,

$$V_w = k \frac{SN}{H} \tag{2.1}$$

where $V_w$ is the total volume of material removed by wear, $k$ is the dimensionless wear coefficient, $N$ is the applied normal load, $S$ is the sliding distance and $H$ is the material hardness [97]. The relationship was developed based on the behavior of crystalline metals,

but has also been shown to describe the behavior of ceramics and even some BMGs [98]. In contrast, some studies have also shown BMGs that do not follow Archard's wear law, in particular Zr- and Fe-based BMGs [129, 130]. Excluding the Cu-Zr-based BMGs, Fig. 2.1c does show that the general trend of Archard's wear law does apply to the Ti, Zr, Fe and Ni-based alloys that were tested. The wear behavior of Cu-Zr-BMGs is therefore not adequately captured by conventional models of wear. Partial crystallization, surface oxides, chemical desegregation, and cooling rate are all likely to play a complex role in the wear loss observed in the Cu-Zr-based BMGs [52]. Further investigations as to why the Cu-Zr-based alloys exhibit this exceptional wear loss are currently underway.

### 2.5.2 Role of Toughness

An important result of the current work is that the design of BMG gears should focus on the interplay between wear-resistance and toughness. As the toughness of the gears approached the values typical of ceramics (<10 MPa-$m^{1/2}$), fracture become the dominant mechanism of failure in gears. When implementing a high strength alloy that lacks dislocation-based plasticity, toughness becomes a necessary engineering design factor [100]. Therefore, the design strategy for wear-resistant BMGs is more closely related to ceramics than crystalline metals. This trend indicates a reversal in the way to implement BMGs into wear-resistance applications, where the literature normally suggests that harder BMGs are more wear resistant. This observation opens up the potential for the widespread use of BMG materials in advanced gear and robotics applications.

Additionally, it is shown that pin-on-disk testing, while good at capturing trends,

is insufficient for predicting the performance of BMG gears because it cannot account for toughness and brittle failure. Thus, pin-on-disk wear testing should not be the standard wear metric for testing BMGs gears. Crystalline metals are sufficiently tough to avoid brittle fracture during normal gear operations. However, the torques and bending moments that are applied to various points of the gear as it rotates, creates different stress states in the material from those experienced during pin-on-disk tests and can cause fracture in BMG gears [93]. Here, we demonstrate that gear-on-gear testing serves as a more vigorous performance test, which allows us to identify a crucial material property in the design of BMG gears—toughness. These tests were enabled by the development of net-shaped BMG gear casting, which allowed us to test a statistically significant number of BMG alloys.

For the gear dimensions and operating conditions used in this work, we identified the nominal alloy $Cu_{43}Zr_{43}Al_7Be_7$ as the most robust BMG gear material, which demonstrates the best combination of both toughness (32 MPa-$m^{1/2}$) and GFA (>10 mm). Through slight alterations in the composition to $Cu_{46}Zr_{46}Al_3Be_5$, we were able to increase the toughness by 75% to 56 MPa-$m^{1/2}$.

## 2.6 Conclusion

Contrary to many claims, not all bulk metallic glasses have good wear resistance. In particular, BMGs and BMGMCs that have been specifically designed for maximum toughness, were shown to have extremely poor wear resistance. On the other hand,

Cu-Zr-based BMGs demonstrate exceptional wear-resistance, and it is suggested that the wear-resistance does not correlate with Vickers' hardness. Through gear-on-gear testing it is shown that the $Cu_{43}Zr_{43}Al_7Be_7$ BMG exhibits a 60% improvement in wear-resistance as compared to one high-performance steel, Vascomax C300, which is currently used by NASA on the Mars rover Curiosity.

Owing to the complex stress state on gears as opposed to pin-on-disk tests, gear-on-gear testing is shown to be a superior method to evaluate the wear performance of BMGs. Traditional pin-on-disk wear testing does not adequately evaluate materials toughness because the sample is subject to purely sliding wear in compression. Gear-on-gear testing brings attention to the important role of toughness. Although the high toughness BMGs are not wear-resistant, a minimum toughness is still identified as an important material property in order to prevent catastrophic failure of BMG gears. To optimize a BMG alloy for wear-resistance, the minimum in the curve of toughness versus wear loss must be found. The Cu-Zr-based BMG system is identified as an ideal family of alloys within this property space.

Finally, net-shaped casting of centimeter-scale bulk-metallic-glasses is successfully demonstrated. The as-cast gears require no post-machining and can be integrated into a gear-on-gear test rig or functional gearbox directly from the mold. Furthermore, the surface quality of the net-shaped BMG gears is superior to that of EDMed gears, and it is expected to improve the wear-performance and lifetime of the BMG gear. The current paper is the first step of many towards the eventual implementation of BMG gears and gear systems. Ongoing work at NASA JPL/Caltech in conjunction with collaborators

at UC San Diego and others, involves gearbox testing, environmental testing, commercial fabrication, alloy development, gear characterization and the development of BMG gearbox components.

## 2.7 Acknowledgements

D. C. Hofmann acknowledges financial support from NASA's Science Mission Directorate and Space Technology Mission Directorate through the Game Changing Development program under Prime Contract #NAS7-03001 and from the Presidential Early Career Award. Part of this research was done at the Jet Propulsion Laboratory, California Institute of Technology, under contract with NASA. L. M. Andersen acknowledges financial support from the Achievement Rewards for College Scientists (ARCS) Foundation and the Jet Propulsion Laboratory (JPL) Summer Internship Program. The authors would like to thank Nicolo Valigi for his invaluable contributions in performing hardness and elastic constant measurements and running gear-on-gear testing. The authors acknowledge useful discussions with K. Boykins, B. Wilcox, D. Bickler, G. Davis, and M. Knopp. Patents related to the current technology have been filed with the California Institute of Technology.

Chapter 2, in full, is a reprint of the material that is being prepared for publication in Advanced Engineering Materials. Hofmann, Douglas; Andersen, Laura; Kolodziejska, Joanna; Roberts, Scott; Borgonia, Robert; Vecchio, Kenneth; Kennett, Andrew, WILEY-VCH Verlag GmbH & Co. KGaA, 2016.

# 3 Criteria to Optimize the Toughness of Cu-Zr-based Bulk Metallic Glasses with in-situ Crystallization

## 3.1 Abstract

The notch toughness of wear-resistant $Cu_{43}Zr_{43}Al_7Be_7$ bulk metallic glasses (BMGs) with in-situ crystallization is investigated. Using different cooling rates during copper mold casting and a post-cast anneal, the amount of crystallization is controlled and varied. The notch toughness correlates most closely with the composition of the remaining amorphous matrix, as measured by energy-dispersive X-ray spectroscopy (EDS). As the matrix composition shifts further away from the designed composition, the toughness decreases. The sample with a matrix composition that closely matches $Cu_{43}Zr_{43}Al_7Be_7$ is shown to be the toughest, with a notch toughness of 54 MPa-$m^{1/2}$. X-ray diffraction, EDS and electron backscatter diffraction (EBSD) were used to identify the

metastable crystalline phases as $Cu_3Zr_5Al_2$(+Be) with an $Fm\bar{3}m$ structure. Furthermore, the crystalline phases are shown to be harder than the glassy matrix, and therefore likely contribute to the high wear-resistance of the studied BMG. Under standard XRD operating parameters, as used in the literature, all of the samples examined in this study appear to be fully amorphous, yet many are shown to contain a significant number of crystalline regions. In order to identify in-situ crystallization using XRD with Cu K$\alpha$ radiation, extremely long dwell times and high X-ray fluxes are required. This demonstrates the importance of reporting XRD operating parameters when trying to evaluate the amorphous nature of BMGs.

## 3.2 Introduction

Due to their superior strength and high hardness, bulk metallic glasses (BMGs) have been suggested to be well-suited material replacements for wear-resistant applications such as sensor coatings, medical implants, and hardfacing alloys [98]. In fact, there is sufficient evidence that in some cases BMGs outperform crystalline metals in wear testing. For example, Zr-based BMG bearing rollers have exhibited better wear-resistance than commercial GCr15 steel rollers [109]. Furthermore, the durability of a motor with Ni-based BMG microgears exceeded the durability of the same motor made with carbon tool steel microgears by a factor of four [126]. Studies have also shown that crystalline phases can positively affect the wear-resistance of BMGs [129–131]. Indeed, compared to monolithic materials, wear-resistance is generally enhanced by introducing

a hard secondary phase into the softer matrix material [98, 132]. Thus, it is beneficial to study BMGs (both fully amorphous and partially crystalline) that exhibit excellent wear properties in order to optimize their utility.

Toughness plays an important role in the wear-resistance of brittle materials. Due to the brittle nature of BMGs and their lack of plastic yielding in tension, one would expect the wear behavior of BMGs to be controlled by toughness rather than hardness as predicted by Archard's wear law for crystalline metals [106, 107, 133]. Therefore, maximizing the toughness in wear-resistant BMGs is a key strategy for designing novel wear-resistant materials.

Cu-Zr-based BMGs are promising candidates for engineering applications due to their excellent mechanical properties both with and without small fractions of crystalline phases [10, 78]. Furthermore, recent work by the present authors shows that Cu-Zr-based BMGs exhibit excellent wear-resistance exceeding that of current state-of-the-art crystalline gear material by a 60% increase in wear-resistance [134]. And, in contrast to most BMG systems, there is even substantial data on the defect tolerance of Cu-Zr-based BMGs as measured through fatigue and fracture toughness tests [135, 136].

Such testing, however, illuminates a significant drawback of Cu-Zr-based BMGs in that their reported fractured toughness values vary significantly. One study of a series of Cu-Zr-based BMGs produced an average variation in notch toughness among samples of identical composition that spanned 12.5 MPa-$m^{1/2}$ [136]. In the same study, $Cu_{45}Zr_{46}Al_9$ yielded a notch toughness of 56 MPa-$m^{1/2}$, while another study reported that fatigue pre-cracked $Cu_{45}Zr_{48}Al_7$ yielded a fracture toughness as high as 101 MPa-$m^{1/2}$ [137].

It is surprising that, with a minor difference in composition, the latter material had a reported toughness nearly double that of the former. Especially when it is expected that a fatigue pre-cracked specimen would yield a lower fracture toughness value due to the sharper crack tip root radius [138]. In yet another report, which utilized data from a four-point-bend fatigue test, the fracture toughness of $Cu_{45}Zr_{45}Ag_7Al_3$ was estimated to be as low as 23–30 MPa-$m^{1/2}$ [139]. One author has suggested that this variation is mostly attributable to differences in processing conditions [140]. In order to fully utilize the potential of wear-resistant Cu-Zr-based BMGs, it is critical to first understand the relationship between processing and toughness.

The structure and properties of virtually every material are inherently linked to the processing conditions during fabrication. BMGs are no exception, and in fact, are particularly sensitive to their processing history, most notably the cooling rate during vitrification. Cu-Zr-based BMGs, in particular, have been shown to be exceptionally susceptible to small volume fractions of crystallization. One study revealed that while X-ray diffraction (XRD) of $Cu_{50}Zr_{50}$ exhibited patterns with the characteristic broad diffraction maxima of a glassy structure, images obtained from high-resolution transmission electron microscopy (TEM) and selected area electron diffraction (SAED) revealed the presence of tiny crystallites in the glassy matrix [10]. Another study indicated that minute changes in the microalloying content from $Cu_{45}Zr_{49}Al_6$ to $Cu_{45}Zr_{47}Al_8$ in 8 mm copper-mold cast rods changed their structure from fully amorphous to partially amorphous with some crystallization [141]. Thus, the high sensitivity of the metastable Cu-Zr glassy system on processing conditions makes it imperative to fully assess the amorphous structure when

evaluating the toughness of Cu-Zr-based BMGs.

In this work, we study the toughness of a highly wear-resistant Cu-Zr-based BMG with small amounts of in-situ crystallization. Varied cooling rates during casting and post-fabrication annealing are used to induce small amounts of crystallization in $Cu_{43}Zr_{43}Al_7Be_7$. The results demonstrate that, when using standard XRD measurements, small volume fractions of crystalline regions can easily go undetected, which may explain the observed variance in toughness values. Furthermore, the intended properties, such as resistance to shear flow and toughness, are shown to vary as a function of the remaining base composition. Since crystal formation alters the designed high-glass forming matrix composition, the matrix composition can be used as a simple measurement for the degree of crystallization and toughness. The crystalline phase formed in $Cu_{43}Zr_{43}Al_7Be_7$ is identified as a beryllium containing $\tau_3$ phase with a cubic $Fm\bar{3}m$ structure.

## 3.3 Materials and Methods

The Cu-Zr-based bulk metallic glass $Cu_{43}Zr_{43}Al_7Be_7$ (at%) was selected as the experimental alloy because of its high glass-forming-ability (12 mm), large plastic strain (up to 7% in compression), and lack of exotic or precious elements (such as Ca, Pd or Au), making it a strong candidate for a BMG structural material [128]. Alloy ingots of 15 g were prepared by arc-melting high purity elements (>99.5% pure) in a Ti-gettered argon atmosphere. Prior to melting the vacuum chamber was twice evacuated to <30 mTorr and purged with argon. To ensure homogeneity, the ingots were melted for 3 min and flipped

at 1 min intervals. The precisely-weighed elements and respective resulting ingots were weighed before and after melting to ensure that material was not lost during the melting process; the change in weight was less than 0.1%. The ingots were suction-cast into a water-cooled copper mold to form 3 mm diameter rods. Each rod was then cut into three 28 mm specimens for toughness testing.

To evaluate the effects of processing on the toughness of the metallic glass, a qualitative method for altering the cooling rate during casting was employed. Because approximately 5 g of $Cu_{43}Zr_{43}Al_7Be_7$ was necessary to fill the 3 mm diameter rod mold, the excess material solidified into a small ingot attached to the rod at the entrance of the mold cavity. Fig. 3.1a shows a cross-section schematic diagram of the mold filled with different sized ingots. As the amount of excess material increased, the percentage of the surface area in contact with the copper mold decreased, slightly reducing the cooling rate. While the common approach to vary the cooling rate is to cast rods of different diameters, the method presented here, eliminates the possibility that the sample diameter influences the fracture toughness result. A previous study has suggested that size-independent $K_{IC}$ results for bulk metallic glasses should be reported with caution [142].

Furthermore, selected as-cast rods with comparable cooling rates were annealed below $T_g$ the glass transition temperature, $T_g$, to induce structural relaxation and to obtain more variability in toughness. The samples were heated to 682 K in a vacuum furnace, held for three minutes and air-cooled to room temperature. For reference, the onset of $T_g$ for this particular alloy with in-situ crystallization was measured to begin at 713 K.

Three cross-sections cut from the location near the fracture point of each rod were

cold-mounted and polished to a final step with a 0.05 $\mu$m silica solution. The amorphous structure of each sample was characterized using a Rigaku Rotoflex X-ray diffractometer with Cu-K$\alpha$ radiation. The X-ray operating voltage, current and step size were held constant at 40 keV, 140 mA and 0.02$^\circ$, respectively, while dwell times of 1 s and 20 s were used to compare the detection limits of XRD.

The microstructures were examined with a light optical microscope equipped with differential interference contrast (DIC), which is capable of accentuating surface features such as hard crystalline particles that protrude from a softer amorphous matrix. The topography was further imaged at 20 kV in an FEI Quanta 600 scanning electron microscope (SEM) equipped with a Bruker energy-dispersive X-ray spectroscopy (EDS) and electron backscattered diffraction (EBSD) detectors. Imaging with the backscattered electron detector at a tilt angle of 30$^\circ$ reduced the beam interaction volume and brought out the topography created by hard crystalline regions. Selective EDS point analysis (an average of three areas) was used to identify the composition of the amorphous matrix and the crystalline particles. EBSD was used to identify the crystal structure of the crystalline particles.

Thermal properties of the samples were measured using a Perkin-Elmer differential scanning calorimeter (DSC) calibrated with indium and zinc standards. Cast rod cross-sections of about 60 mg were heated at a continuous rate of 0.33 K/s under purged argon flow. A LECO M-400-HI digital microhardness tester was used to measure the Vickers' microhardness of the samples at load of 10 gf for 15 s. Because of the small indent size, it was possible to independently characterize the hardness of the amorphous

region and microscale crystals.

Notch toughness was measured using a four-point bend setup on a screw-driven 5980 Instron load frame with a displacement rate of 0.1 mm/min. The inner and outer spans of the four-point bend fixture were 8 mm and 16 mm, respectively. A notch was cut in the center of each specimen using a low speed diamond saw to a depth 0.4–0.5 times the diameter with a root radius of 90 $\mu$m.

All samples were verified to meet plane strain conditions based on the sample size constraint. For a linear elastic fracture toughness value to be plane strain, the out-of-plane thickness dimension (in this case the diameter) must equal or exceed $2.5\left(K_Q/\sigma_y\right)^2$ [121]. This calculation is based on the plastic zone size at the crack tip. The plastic zone radius, $r_p$, which can be estimated from $r_p = K_Q^2/\pi\sigma_y^2$, ranged from 289 $\mu$m in the toughest sample to 82 $\mu$m in the most brittle sample. If this specimen thickness constraint is not met, the fracture could take place under partial or full plane stress conditions, potentially causing an overestimation of fracture toughness.

The notch toughness, $K_{IC}$, was calculated from the critical fracture load using Kiuchi's finite element modeled stress intensity factor for a notched round rod [122]. For a beam of a circular cross section in four-point-bend, the toughness is defined as:

$$K_{IC} = \frac{8YP_f(L_o - L_i)\sqrt{a}}{\sqrt{\pi}d^3} \tag{3.1}$$

where $P_f$ is the applied force at fracture, $a$ is the notch depth, $d$ is the rod diameter, and $L_o$ and $L_i$ are the outer and inner loading spans, respectively. The geometric constant, $Y$

is plotted as a function of $a/d$ for a circular cross-section and a notch radius of R = $\infty$ in [122]. The equation of the curve fit for the data was found to be

where $P_f$ is the applied force at fracture, $a$ is the notch depth, $d$ is the rod diameter, and $L_o$ and $L_i$ are the outer and inner loading spans, respectively. The geometric constant, $Y$, is plotted as a function of $a/d$ for a circular cross-section and a notch radius of $R = \infty$ in Ref. [122]. The equation of the curve fit for the data was found to be:

$$Y = -30.332\left(\frac{a}{d}\right)^4 + 38.11\left(\frac{a}{d}\right)^3 - 9.2605\left(\frac{a}{d}\right)^2 - 0.828\left(\frac{a}{d}\right) + 1.12 \qquad (3.2)$$

Data from the plot in Ref. [122] match the modeled equation with an R-squared value of 0.9996. Complete detail on the calculation can be found in App. A.

## 3.4 Results

### 3.4.1 Notch Toughness

Even though all the rods were made from the same nominal composition of $Cu_{43}Zr_{43}Al_7Be_7$, there is a clear variation in notch toughness as a function of the ingot size, as shown in Fig. 3.1b. The variation confirms that a larger ingot size when casting (imposing a slower cooling rate) when casting negatively affects the notch toughness of the BMG. On the other hand, the notch toughness values do not change significantly from the 5 g to the 10 g ingot. This can be explained through closer inspection of Fig. 3.1a.

The qualitative method used to control the cooling rate during casting likely had a larger impact on the 15 g samples with more excess material outside the mold.

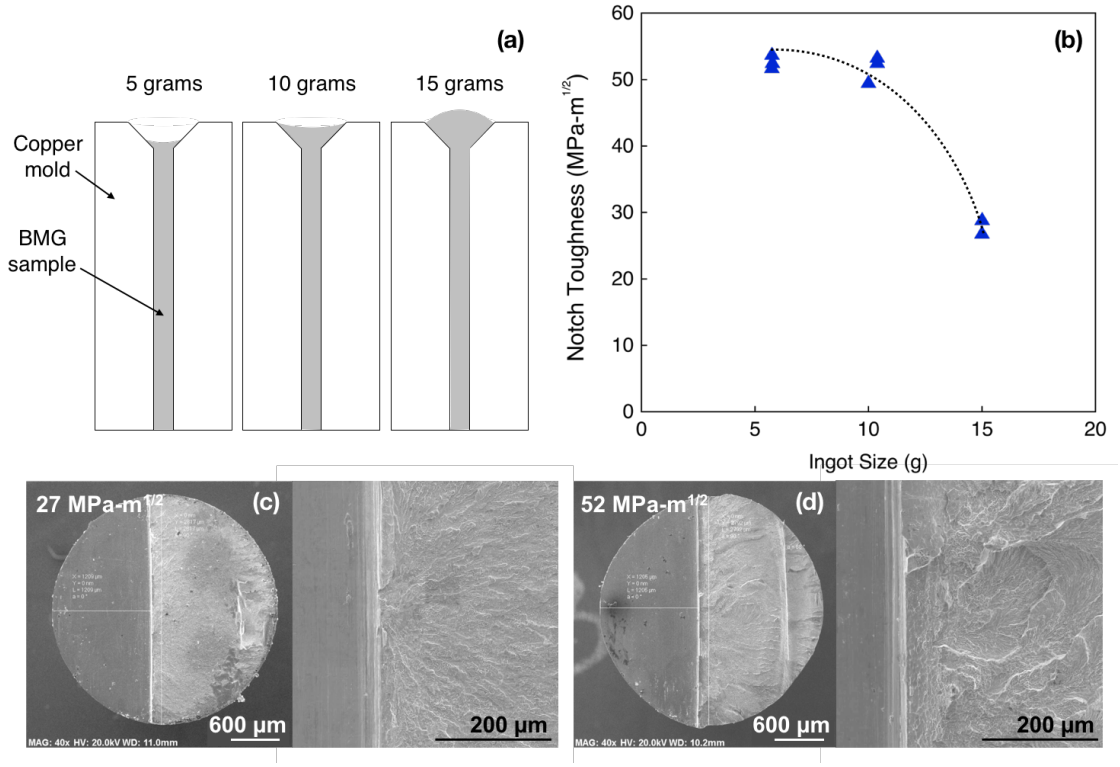


**Figure 3.1**: Variation in notch toughness of $Cu_{43}Zr_{43}Al_7Be_7$ with ingot size. (a) Cross-sectional schematic of filled copper mold with ingots of different mass. The top portion of the cast ingot is exposed to an argon atmosphere rather than in contact with the water-cooled copper mold. (b) Variation in notch toughness of 3 mm $Cu_{43}Zr_{43}Al_7Be_7$ diameter rods cast from different sized ingots. With increasing ingot mass, more excess material solidifies at the entrance to the mold cavity decreasing contact with the water-cooled copper mold; therefore, the cooling rate is reduced. (c) SEM images of the fracture surfaces of a brittle sample. (d) SEM images of the fracture surfaces of a tough sample.

The notch toughness differences can also be seen by the variation in the fracture surface morphology. SEM images in Fig. 3.1c–d are representative of the tough and brittle fracture patterns observed in this experiment. Samples with a notch toughness below 30 MPa-m$^{1/2}$ exhibited a smooth flat-fracture, as shown in Fig. 3.1c. On the other

hand, samples with toughness values above 50 MPa-$m^{1/2}$ had rough and jagged fracture surfaces, as seen in Fig. 3.1d. The high magnification images on the right in each figure show the clear difference in fracture mode. A flat fracture is associated with cavitation and catastrophic crack opening, whereas a rough surface with pronounced river patterns is associated with plasticity caused by an intense shear band network [143].

### 3.4.2 In-situ Crystallization

A sufficiently long dwell time was necessary to identify small volume fractions of crystalline phases in BMGs. The XRD scans with a 1 s dwell time are shown in Fig. 3.2a. Surprisingly, although significant variations in notch toughness were observed, all samples displayed a broad amorphous hump, which is generally accepted in the literature as suggesting a lack of long-range order. To investigate further, XRD measurements were taken twenty times slower with a dwell time of 20 s at each step. The resulting diffraction patterns shown in Fig. 3.2b prove that a sufficiently long dwell time is necessary to identify small volume fractions of crystalline phases in BMGs.

Light optical microscopy with differential interference contrast (DIC) also verified the presence of a crystalline phase within the glassy matrix. Fig. 3.2c–e shows the variation in crystallization among samples of different measured notch toughness values. The micrograph of the low toughness sample in Fig. 3.2c exhibited crystals up to 40 $\mu$m in length with a distinguishable dendrite structure. On the other hand, the high toughness sample exhibited sub-micron crystals that were only identifiable by a texture change in

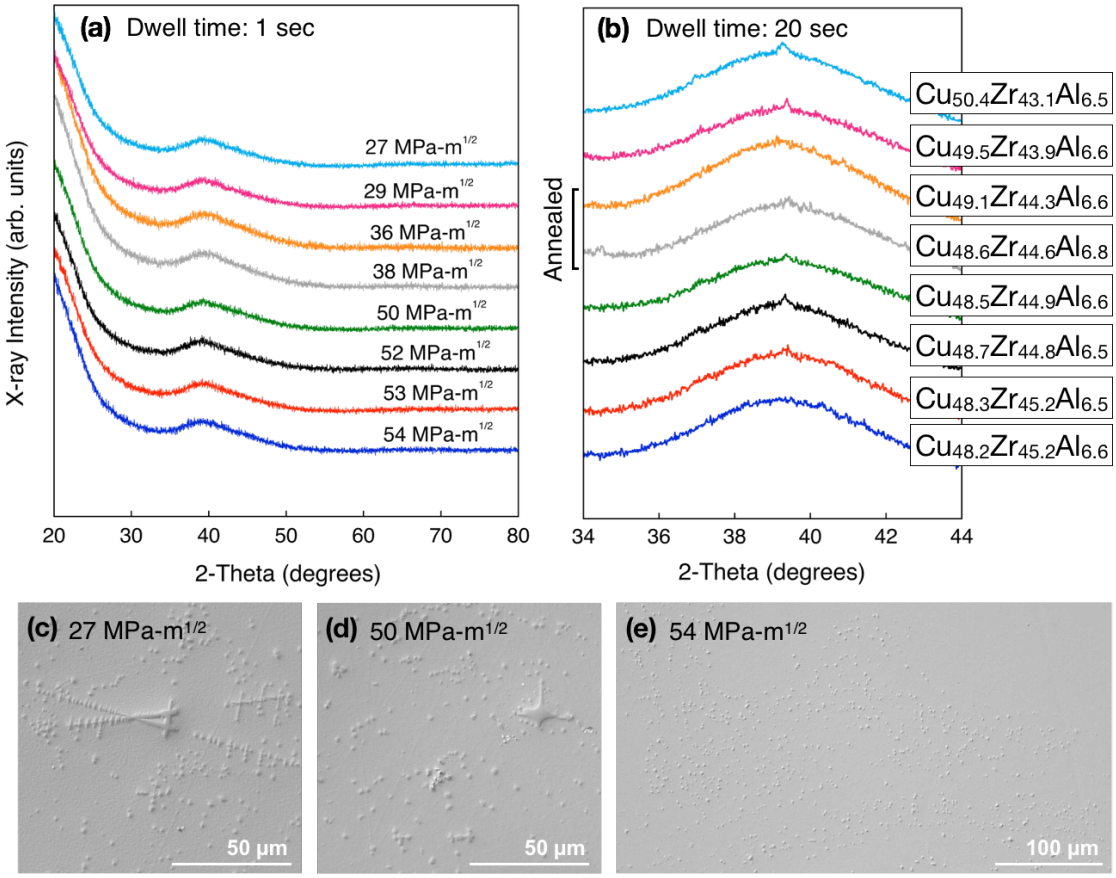


**Figure 3.2**: Identification of small amounts of in-situ crystallization through X-ray diffraction (XRD) and light optical microscopy with differential interference contrast (DIC). (a) XRD patterns for copper mold cast 3 mm rods of $Cu_{43}Zr_{43}Al_7Be_7$ scanned with a 1 s dwell time. The interaction time is not sufficient for detecting small volume fractions of crystallization in BMGs. (b) XRD patterns of the exact same samples with a 20 s dwell time show that the samples exhibit partial crystallization. Although it is difficult to compare crystalline volume fractions using XRD, it appears that notch toughness correlates with the composition of the remaining amorphous matrix. The composition was obtained from EDS at 20 kV and excluded beryllium. (c) Optical micrograph with differential image contrast of a low toughness sample shows large micrometer scale crystals that are just barely detectable under a slow 20 s dwell XRD scan. (d) Higher toughness sample, and (e) very high toughness sample with crystalline phases small enough to be undetectable in a 20 s dwell time (0.02° step size) XRD scan (see bottom dark blue pattern in (b)).

the crystal containing regions, as shown in Fig. 3.2e. The corresponding high resolution XRD pattern is shown in dark blue (bottom) in Fig. 3.2b. An XRD scan with a 20 s dwell time was still unable to detect this small degree of crystallization.

The fact that the crystalline phase in Fig. 3.2c–e is protruding from the matrix suggests that it is a harder phase. To confirm this, microhardness measurements of the crystalline particles were compared with that of the amorphous matrix. Crystals of sufficient size were chosen for hardness measurements to minimize interaction from the surrounding matrix. For example, the largest crystal in Fig. 3.2d is about 6 $\mu$m in size with dendrites that extend up to 23 $\mu$m in length. The low force Vickers' indent had diagonals of 3.5 $\pm$ 0.1 $\mu$m, which fit well inside the crystal. The crystalline phase, with an average Vickers' hardness of HV 694 $\pm$ 2.2, was, in fact, harder than the amorphous matrix, hardness of HV 635 $\pm$ 1.6.

### 3.4.3 Phase Identification

EDS point analysis across multiple samples confirmed that the composition of in-situ crystallization is near $Cu_3Zr_5Al_2$, excluding the presence of beryllium. Due to instrument limitations on obtaining a quantitative atomic percent for beryllium, the exact composition of the crystal could not be determined. The EDS maps in Fig. 3.3a show a qualitative comparison of the crystalline phase and amorphous matrix compositions. Relative to the matrix, the crystalline phase is rich in aluminum and zirconium and deficient in copper. The sample in which this particular crystal was found had a notch toughness of $K_{IC}$ = 29 MPa-m$^{1/2}$.

EBSD identified the structure of the $Cu_3Zr_5Al_2$(+Be) crystalline phase as cubic $Fm\bar{3}m$. A forward-scattered electron image is shown in Fig. 3.3b with the corresponding EBSD phase map for a structure consistent with $Al_7Cu_{16}Zr_6$ in Fig. 3.3c. The similarity

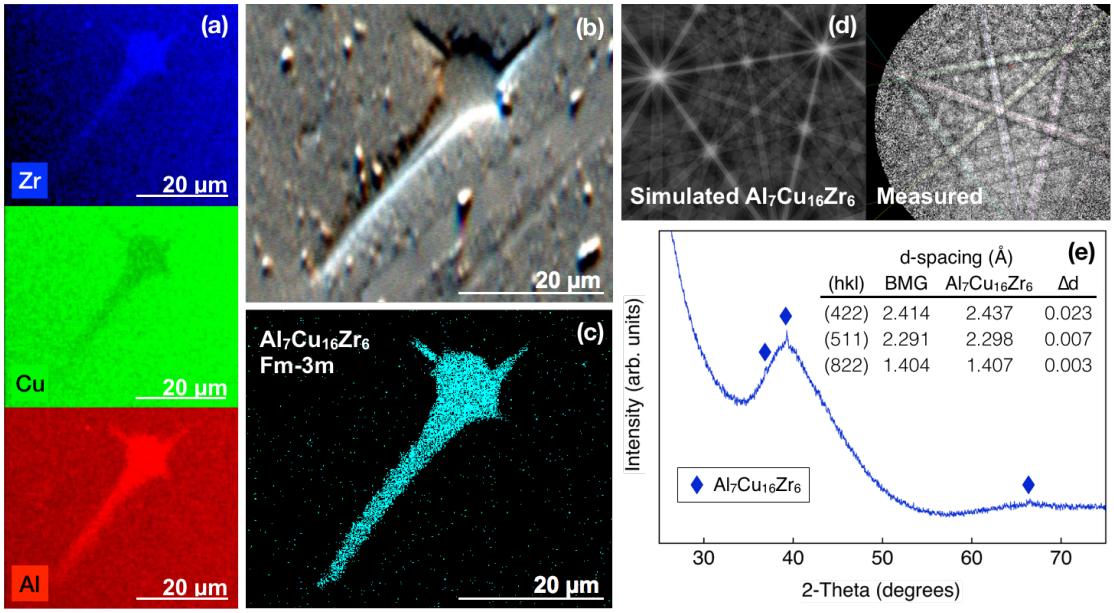


**Figure 3.3**: Phase and structure identification of in-situ crystallization in $Cu_{43}Zr_{43}Al_7Be_7$ using EDS, EBSD and XRD. (a) EDS map of crystallization in $Cu_{43}Zr_{43}Al_7Be_7$. The composition is rich in Zr and Al and deficient in Cu, relative to the matrix. Beryllium content could not be quantified due to limitations of its X-ray absorption. (b) A forward-scattered electron image of crystal and (c) corresponding EBSD phase map showing a strong match to the $Fm\bar{3}m$ structure of $Al_7Cu_{16}Zr_6$. (d) Simulated Kikuchi pattern of $Al_7Cu_{16}Zr_6$ (left) and measured Kikuchi pattern of the identified crystal (right). (e) Indexed XRD diffraction pattern of same sample identifying the $Fm\bar{3}m$ structure of $Al_7Cu_{16}Zr_6$ and a table comparing the calculated d-spacings.

in structure to the $Al_7Cu_{16}Zr_6$ phase is verified by the comparison between the simulated Kikuchi pattern and measured Kikuchi pattern, as shown in Fig. 3.3d. However, from EDS measurements, it is clear that the composition of the crystal is not an $Al_7Cu_{16}Zr_6$ copper-rich phase, but rather closer to a $Cu_3Zr_5Al_2$(+Be) phase. The EBSD result simply shows that the structure of the crystal most closely identifies with that of $Al_7Cu_{16}Zr_6$—a cubic $Fm\bar{3}m$ structure; XRD also detects evidence of this same structure. Fig. 3.3e shows the indexed XRD diffraction pattern (dwell time = 20s) with an inserted table comparing calculated d-spacings. The small difference in lattice spacing is likely due to the presence of beryllium.

Using the ICDD PDF-4+ X-ray database and the Bruker EBSD database, we were unable to identify the structure as $Cu_3Zr_5Al_2$ because, in the literature to date, there is not yet a verified structure for this phase, often referred to as $\tau_3$ [144]. Although the crystalline phase identified here includes a trace amount of beryllium, strong evidence indicates that the highly metastable $\tau_3$ phase of $Cu_3Zr_5Al_2$ forms a cubic $Fm\bar{3}m$ crystal structure. It is possible that the presence of beryllium contributes to the stabilization of the highly metastable $\tau_3$ phase.

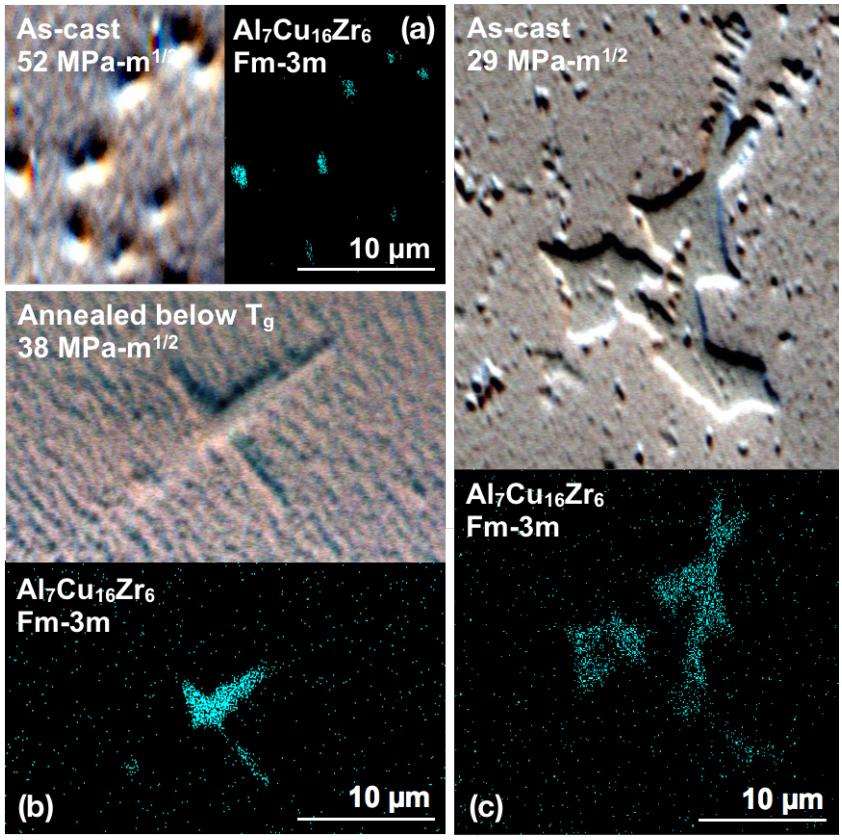


**Figure 3.4**: Verification of only one phase identified via in-situ crystallization in $Cu_{43}Zr_{43}Al_7Be_7$. Forward scattered images and EBSD phase maps for crystals identified in samples with different fracture toughness. The samples in (a, b, and c) had a fracture toughness of 52, 38 and 29 MPa-$m^{1/2}$, respectively. All crystals identified in each sample were confirmed to be the same $Cu_3Zr_5Al_2$(+Be) phase with an $Fm\bar{3}m$ structure.

EDS and EBSD measurements were repeated for multiple crystals across many samples with a range of toughness values. In every crystal analyzed, the composition was found to be near $Cu_3Zr_5Al_2$(+Be) and the structure was verified as $Fm\bar{3}m$. Fig. 3.4 shows a compilation of additional EBSD results from multiple crystals. Fig. 3.4a shows a forward-scattered electron image and corresponding EBSD phase map of a crystal in an annealed sample that measured a notch toughness of 38 MPa-$m^{1/2}$. Similarly, in Fig. 3.4b the same type of crystal is shown in a brittle as-cast sample with a notch toughness of 29 MPa-$m^{1/2}$. The images in Fig. 3.4c show that across a large field of view, all crystals are shown to be the same identified metastable $Cu_3Zr_5Al_2$(+Be) phase.

### 3.4.4 Impact on Toughness

The notch toughness was found to correlate closely with a change in the amorphous matrix composition. EDS point analysis was taken in regions near the fracture surface, which were identified as amorphous based on their smooth topography. Fig. 3.5a shows a plot of the zirconium concentration in the matrix (at%) versus the notch toughness. The inset exemplifies EDS measurement locations in a backscattered electron SEM image. As the Zr- and Al-rich crystalline particles are formed and scavenged from the matrix, this causes the composition of the amorphous matrix to depart from the intended $Cu_{43}Zr_{43}Al_7Be_7$ composition. Accordingly, the reported notch toughness values represent that of the remaining matrix composition rather than the $Cu_{43}Zr_{43}Al_7Be_7$ composition. As the matrix composition shifts further and further away from the designed composition (46.2 at% Zr when excluding Be), the toughness systematically decreases.

The results here suggest that the composition of the final vitrified amorphous phase is a key factor in the notch toughness of BMGs with in-situ crystallization.

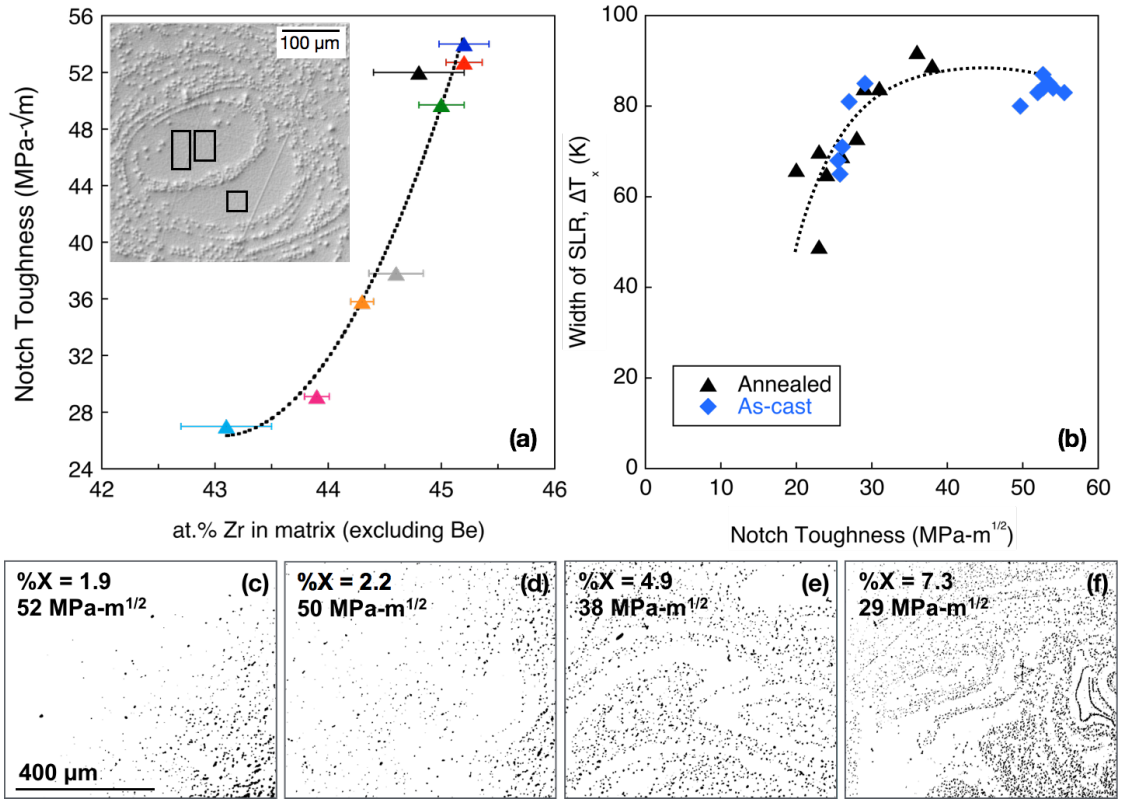


**Figure 3.5**: Effect of crystallization on toughness of $Cu_{43}Zr_{43}Al_7Be_7$. (a) Toughness decreases with decreasing at% zirconium in the remaining matrix composition. Note that the measured composition is normalized after excluding beryllium; the intended Zr concentration is 46.2 at%. Inset in (a) shows an example location of the EDS measurement. (b) DSC results show a positive correlation between $\Delta T_x$ and notch toughness. (c-f) Threshold optimized DIC images used to estimate the volume fraction of in-situ crystallization in select samples. The calculated area fraction of crystalline phases increases as the notch toughness decreases.

Furthermore, ImageJ photo editing software was used to estimate the crystalline volume fraction. Fig. 3.5c–f show threshold adjusted DIC images used to estimate the area fraction of crystals in a given field of view in an optical micrograph. By a simple comparison, it can be seen that the calculated area fraction of crystalline phases increases

as the notch toughness decreases. This relationship compares well with that of the matrix composition. This is expected, given the natural link between the two concepts.

## 3.5 Discussion

### 3.5.1 Limitations of XRD

XRD is usually the first characterization tool used in BMG studies to confirm the amorphous structure of an alloy. This study clearly demonstrates the limitations of the technique. The intensity of the peaks in an XRD pattern are based on a volume fraction of crystalline regions in the material and XRD operating parameters. Therefore, under typical XRD operating conditions (dwell time of 1 s), the small amount of crystallization in a partially crystalline BMG may easily go undetected. In particular, small crystalline peaks, in particular, when superimposed on the amorphous hump, go undetected. The difficulty in detecting partial crystallization, as shown here, may be an origin for the observed wide scatter in reported toughness values of BMGs, particularly Cu-Zr BMGs.

In this study, which employed a high X-ray flux rotating anode system operated at nearly 5 kW power, a dwell time of at least 20 s was necessary to identify crystallization. Even so, the resolution was insufficient to calculate or make a qualitative comparison of differences in crystallized volume fraction. Therefore, the results of this study show that it is critically important to report all operating parameters when using XRD to identify an amorphous structure. Additional characterization techniques such as optical microscopy with DIC, SEM-EBSD, high-resolution TEM or SAED may also be used to confirm the

presence or absence of crystalline regions in BMGs. An advantage of optical microscopy with DIC and SEM-EBSD, is that a large area of material (~100 $\mu m^2$) can be readily characterized.

### 3.5.2 The Role of In-situ Crystallization on Toughness

Previously, it has been shown (in Zr- and Pd-based BMGs) that a dramatic drop in fracture toughness occurs when the volume fraction of crystal phase reaches about 7% [145]. Interestingly, the most brittle samples in this study also have an estimated volume fraction of crystallization of around 7%. Similar to the authors findings in Ref. [145], the samples in this work with at least 7% crystallization experience a reduction in toughness of ~40%—a dramatic change by simply using a larger ingot during casting. However, in this case, the change in toughness seems to be more gradual, rather than a steep drop-off at a critical value.

Partially-crystalline BMGs are expected to behave differently based on the alloying elements and the properties of the crystalline phases that form. It has been shown that crystallization may cause either toughening or embrittlement, depending on the elastic properties of the matrix and the crystal phases [145]. In the study identifying a critical drop in toughness was identified at about 7% crystalline volume fraction, the fracture strength of the metallic glass was shown to be greater than that of the crystalline phase, or $\sigma_{MG} < \sigma_c$. In this case, based on the hardness result, we expect $\sigma_{MG} > \sigma_c$. In such a situation, assuming a perfect interface between the matrix and the crystals, finite element analysis predicts an increase in toughness [145]. However, removing the assumption

of a perfect interface, embrittlement can occur. Here, we suggest that the decrease in toughness from in-situ crystallization is due to a combination of the introduced stress concentrations at the interface and the change in optimal composition of the amorphous matrix.

The large changes in toughness observed through minor compositional changes in the matrix are expected to occur because of an alteration in the medium range order affecting the elastic stress distribution [146]. When a metallic glass is loaded and deforms, shear bands form under localized stress concentrations, leading to intense shearing and catastrophic failure of the sample [49, 51]. The activation of shear bands takes place preferentially in the areas where the atomic packing efficiency is relatively small (i.e. higher free volume) [147]. Thus, materials with more free volume are expected to nucleate more shear bands [148], leading to more plastic deformation. During the solidification process, a slower cooling rate provides more time for structural relaxation, thereby creating a denser atomic configuration with less free volume [149, 150]. Therefore, for the same amorphous alloy, a slower cooling rate produces a more densely-packed structure, reducing the propensity for shear band activation and leading to a degradation in ductility and toughness.

The large changes in toughness observed through minor compositional changes in the matrix are expected to occur because of an alteration in the medium range order affecting the elastic stress distribution [146]. When a metallic glass is loaded and deforms, shear bands form under localized stress concentrations, leading to intense shearing and catastrophic failure of the sample [49, 51]. The activation of shear bands takes place

preferentially in the areas where the atomic packing efficiency is relatively small (i.e. higher free volume) [147]. Thus, materials with more free volume are expected to nucleate more shear bands [148], leading to more plastic deformation. During the solidification process, a slower cooling rate provides more time for structural relaxation creating a denser atomic configuration with less free volume [149,150]. Therefore, for the same amorphous alloy, a slower cooling rate produces a more densely packed structure, reducing the propensity for shear band activation and leads to a degradation in ductility and toughness.

### 3.5.3 Optimizing Toughness and Wear-Resistance

Although often it makes sense to simply avoid crystallization in BMGs, in some cases, small amounts of partial crystallization are inevitable and may even be beneficial. For example, complete avoidance of crystallization has proven difficult for thermoplastic forming [151]. On the other hand, partial crystallization may occur in bulk net-shaped parts when the sample geometry becomes more complicated than a simple round rod that is used to determine critical casting diameters [134]. Partial crystallization in some BMGs does not necessarily have a negative consequence. Some reports have shown that partial crystallization in Cu-Zr-based BMGs enhances fracture toughness [74, 152]. Furthermore, the presence of a harder second phase may contribute to enhanced properties and performance measures. For example, in wear-resistant materials, a two-phase composites allows for the hardening advantages of the second phase to be exploited without excessive embrittlement of the alloy [153]. Thus, rather than attempting to

mitigate crystallization, it is more important to optimize for crystallization.

Previous work by the authors shows that many Cu-Zr-based BMGs are wear-resistant, independent of their hardness, and the $Cu_{43}Zr_{43}Al_7Be_7$ BMG is particularly wear-resistant within the Cu-Zr BMG system [134]. Although such result is surprising in light of Archard's wear law [97], this work suggests that undetected partial crystallization may lead to the excellent wear-resistance of Cu-Zr-based BMGs. The $Cu_3Zr_5Al_2$(+Be) crystalline phase that formed in-situ was determined to have a higher hardness than the amorphous matrix, which likely contributes to the superior wear-resistance of this particular alloy. As previously discussed, engineered wear-resistant materials are often composed of hard particles embedded in a soft matrix, which is exactly what was formed by the $Cu_{43}Zr_{43}Al_7Be_7$ BMG in this report. Furthermore, although in-situ crystallization in $Cu_{43}Zr_{43}Al_7Be_7$ decreased the toughness, notch toughness values as high as 54 MPa-$m^{1/2}$ were still obtained. This is comparable to that of the commercially available BMG, Vitreloy™, and sufficiently tough for many engineering applications [154, 155]. It is suggested here that the toughness could be further improved, while still maintaining its wear-resistance, by designing the alloy so that the final matrix composition is that of $Cu_{43}Zr_{43}Al_7Be_7$. In other words, if an alloy is designed so that the matrix composition approaches the $Cu_{43}Zr_{43}Al_7Be_7$ composition, after accounting for the formation of say 7% by volume $Cu_3Zr_5Al_2$(+Be) phase, then an optimized wear-resistant BMG could be obtained.

A major challenge for implementing BMGs into engineering designs is that their properties are strongly tied to their processing conditions. Bulk net-shaped parts cannot

be tested for specific properties (such as toughness) due to the geometric requirements of the test. Therefore, non-destructive or semi-destructive method must be used to analyze the toughness of net-shaped BMGs. The ratio of the elastic shear modulus, $G$, to the bulk modulus, B, is a promising example of such a method. Lewandowski and co-authors showed that when $G$/B is less than a critical value of 0.41–0.43, the BMG is inherently tough, but when greater than this critical value the sample is inherently brittle [60]. Unfortunately, for BMGs with in-situ crystallization, this method cannot be used due to the physics of ultrasonic testing. On the other hand, thermal analysis is a promising technique that can be used to compare microstructural and compositional differences. Fig. 3.5b shows that the width of the supercooled liquid region ($\Delta T_x = T_x - T_g$) increases with increasing notch toughness. A large $\Delta T_x$ suggests that the glassy phase is very stable and resistant to crystallization. Likewise, increases in the casting temperature during vitrification has been shown to enhance the thermal stability of BMGs [156]. Greater thermal stability is attributed to the negative correlation between casting temperature and amount of local ordering among the clusters. For all practical purposes, this work suggests that thermal analysis can be used to characterize the toughness of BMGs with in-situ crystallization.

## 3.6 Conclusions

The effects of in-situ crystallization on the toughness of bulk metallic glass $Cu_{43}Zr_{43}Al_7Be_7$ have been studied. It was found that the toughness decreased as the

matrix composition traveled further from the intended high-glass-forming composition. Notwithstanding, the studied BMG $Cu_{43}Zr_{43}Al_7Be_7$ with crystalline phases exhibited notch toughness as high as 54 MPa-$m^{1/2}$. The crystalline phase, identified as $Cu_3Zr_5Al_2$(+Be) by EDS, exhibited a higher hardness than the amorphous matrix, revealing its potential contribution to the enhanced wear-resistance of the BMG. EBSD and XRD, identified a specific cubic $Fm\bar{3}m$ structure similar to the structure of $Al_7Cu_{16}Zr_6$, but with the composition consistent with a $Cu_3Zr_5Al_2$(+Be) phase. To produce a wear-resistant Cu-Zr-based BMG with high toughness, the nominal alloy composition should be designed to maximize the plasticity and fracture resistance of the remaining matrix composition after in-situ crystallization. An opportunity exists to optimize the wear-resistance of these materials, by forming a high volume fraction of very small crystalline particles, with a matrix composition driven towards $Cu_{43}Zr_{43}Al_7Be_7$.

## 3.7 Acknowledgements

Financial support from the Achievement Rewards for College Scientists (ARCS) Foundation is gratefully acknowledged. D. C. Hofmann acknowledges financial support from the Presidential Early Career Award. L. M. Andersen would like to thank Moritz Stolpe for discussions on thermal analysis measurements.

Chapter 3, in full, is a reprint of the material that was submitted for publication in Materials Science and Engineering: A. Andersen, Laura; Faulhaber, Sabine; Hofmann, Douglas; Vecchio, Kenneth, Elsevier B.V., 2016. The dissertation/thesis author was the

primary investigator and author of this material.

# 4 The Effect of Zirconium Purity on the Glass-Forming-Ability and Notch Toughness of $Cu_{43}Zr_{43}Al_7Be_7$

The contents of this chapter are published: L. M. Andersen, D. C. Hofmann, and K. S. Vecchio, "Effect of zirconium purity on the glass-forming-ability and notch toughness of $Cu_{43}Zr_{43}Al_7Be_7$," *Materials Science and Engineering: A*, vol. 674, pp. 397–405, 2016.

## 4.1 Abstract

The effect of substituting standard grade zirconium lump (99.8% excluding up to 4% hafnium) for high purity zirconium crystal bar (99.5%) in a $Cu_{43}Zr_{43}Al_7Be_7$ bulk metallic glass (BMG) is examined. The final hafnium content in the BMG specimens was found to range from 0 to 0.44 at%. Introducing low purity zirconium significantly decreased the glass-forming-ability and reduced the notch toughness of the BMG. In

contrast, when adding high purity hafnium to $Cu_{43}Zr_{43}Al_7Be_7$ made with high purity zirconium, no significant change in the glass-forming-ability or toughness was observed. This suggests that the introduction of low purity zirconium in BMGs creates a more complex response than a simple addition of hafnium. It is likely that other impurities in the material, such as oxygen, play a role in the complex crystallization kinetics and change in mechanical properties. The notch toughness was measured through four-point-bend tests, which showed a decrease in notch toughness from an average of ~53 MPa-$m^{1/2}$ for the high purity samples to an average of ~29 MPa-$m^{1/2}$ with full substitution of low purity zirconium. A similar decrease in glass-forming-ability and toughness is observed in commercially synthesized high purity $Cu_{43}Zr_{43}Al_7Be_7$. The large scale commercial process is expected to introduced some unintentional impurities, which decrease the properties of the BMG in the same way as the lower purity elements. Lastly, Weibull statistics are used to provide an analysis of variability in toughness for both ingots synthesized in a small laboratory arc-melter and those synthesized commercially.

## 4.2 Introduction

Of the many bulk metallic glass (BMG) compositions, Zr-based BMGs have received the most attention as promising alloys for commercial applications due to their relatively low cost, high processability and large critical casting thickness [3, 157]. More recently, Cu-Zr-based BMGs (alloys in which the main constituents are nearly equal parts copper and zirconium) have gained attention due to their apparent plasticity in

compression and superior wear-resistance [10, 134]. In both systems, zirconium is a vital element and also one of the most expensive. The chemical similarity between zirconium and hafnium makes it difficult (and expensive) to extract high purity zirconium crystal bar (99.5%), making it more than five times the price of zirconium containing up to 4% Hf [158]. Since a major drawback of implementing BMGs into commercial applications is cost, this study investigates the potential for reducing cost by replacing high purity zirconium crystal bar with a hafnium containing a less pure form of zirconium.

It is generally accepted that the glass-forming-ability of an alloy can be enhanced by adding a chemically similar element [159]. Since hafnium is chemically similar to zirconium, and they belong to the same IVB group, it is not surprising that studies have also reported on hafnium additions improving the glass-forming-ability of Zr-based metallic glasses. One study found that a small substitution of 1.5 at% Hf for Zr resulted in an increase in the critical casting diameter of over 50% [160]. A subsequent study showed that up to 12 at% substitution of hafnium for zirconium increased the glass-forming-ability from 14 mm for $Zr_{57}Nb_5Cu_{15.4}Ni_{12.6}Al_{10}$ to 16 mm and also increased the bend ductility [161]. In yet another study, significant hafnium additions to the quinary $Ti_{20}Zr_{20}Cu_{20}Ni_{20}Be_{20}$ high entropy bulk metallic glass (HE-BMG) improved the critical casting diameter from 3 mm to 15 mm, creating a senary $Ti_{16.7}Zr_{16.7}Hf_{16.7}Cu_{16.7}Ni_{16.7}Be_{16.7}$ HE-BMG [162].

But studies have also reported that hafnium additions in Zr-based BMGs may decrease the glass-forming-ability. In a few related studies, the glass-forming-ability of $(Hf_xZr_{1-x})_{52.5}Cu_{17.9}Ni_{14.6}Al_{10}Ti_5$ (with x=0–1) was found to decrease, with increas-

ing hafnium content as demonstrated by a decrease in the reduced glass transition temperature [163, 164]. Furthermore, although a 1.5 at% substitution of Hf for Zr in $Cu_{45}Zr_{45}Ag_{10}$ improved the glass-forming-ability, greater than 5 at% significantly decreased the glass-forming-ability to less than 1 mm [160]. Thus, the effect of substituting small amounts of hafnium for zirconium is complex and highly dependent on the specific BMG composition. In this paper, we present a first report on the effect of hafnium impurities in $Cu_{43}Zr_{43}Al_7Be_7$ by replacing pure zirconium with a more cost-effective hafnium-containing zirconium.

Previous experiments have also suggested that Hf additions in Zr-based BMGs can significantly increase their mechanical properties [161]; similar results have also been seen in Cu-Zr-based alloys. For example, the compressive fracture strength of $Cu_{50}Zr_{45}Al_5$ increased linearly with increasing hafnium substitutions for zirconium ranging from 0 to 1 at% (increments of 0.25 at%) [165]. In a follow-up study, substitutions as high as 25 at% Hf for Zr were found to increase the mechanical properties in $Cu_{45}Zr_{45}Ag_{10}$ [166]. This paper will consider whether hafnium-containing zirconium can also improve the mechanical properties while, at the same time, reduce material costs.

The hafnium concentration in four variations of $Cu_{43}Zr_{43}Al_7Be_7$ is controlled by substituting zirconium crystal bar (99.5% pure) with zirconium lump containing up to 4% hafnium. Four variations are synthesized in a small laboratory arc-melter. A fifth variation is made using high purity Zr and synthesized via a large-scale commercial procedure. Due to the low cost of zirconium lump, the results clarify whether or not a

more cost effective BMG with comparable properties can be produced. Furthermore, the results provide insight into the effects of a large-scale synthesis method rather than the small-scale laboratory procedures most typically used in the literature. The glass-forming-ability of each alloy is analyzed using X-ray diffraction (XRD) and optical microscopy with differential contrast imaging (DIC). Insight into the effect of zirconium purity on the mechanical properties is provided through notch toughness testing. Since BMGs are considered "macroscopically brittle" and display scatter and variability in their mechanical properties, the statistical distribution of the toughness is also provided in the form of a 2-parameter Weibull analysis. The statistics for $Cu_{43}Zr_{43}Al_7Be_7$ made with pure zirconium synthesized in a small laboratory arc-melter and commercially are compared. The results of this study highlight the challenges that must be overcome before bulk metallic glass can be used widely in engineering designs.

## 4.3 Materials and Methods

Bulk metallic glass master ingots of $Cu_{43}Zr_{43}Al_7Be_7$ were prepared using a laboratory arc-melter on a water-cooled copper hearth in a Ti-gettered argon atmosphere. High purity elements were used for copper (>99.5%), aluminum (99.9%) and beryllium (99.9%). The zirconium purity was varied for each ingot: (A and D) zirconium crystal bar (99.5%) obtained from Alfa Aesar (product #10444), (C) zirconium lump (99.8% excluding up to 4% Hf) obtained from Alfa Aesar (product #36253), and (B) half the amount of each form of Zr [158]. In addition, 0.5 at% hafnium was added to Alloy D

using Hf wire (99.7% excluding up to 3% Zr) obtained from Alfa Aesar (product #13435). The nominal composition of each alloy was estimated based on the average hafnium concentration in each final specimen as measured using EDS.

The ingots were melted for 3 min and flipped after each minute to ensure chemical homogeneity. The precisely-weighed elements and respective resulting ingots were weighted before and after melting to ensure that no material was lost during the melting process; the change in weight was less than 0.1%. Commercially-prepared ingot material of $Cu_{43}Zr_{43}Al_7Be_7$, obtained from Materion Corporation™[1], was also studied. The material was received in the form of one large section of an ingot with a mass of 50 g, but was produced in a total batch of more than 15 kg.

For each of the five material variations, 3 mm cylindrical rod samples were prepared by re-melting the ingot material and suction casting it into a water-cooled copper mold. The temperature of the copper mold was monitored during casting to ensure that each rod experienced a similar cooling rate. The densities of the rods were measured by Archimedes' method using methanol as the immersion liquid in order to reduce surface tension. A minimum of nine rods were cast for each alloy and cut into three test specimens. Additional rods were fabricated for the two high purity samples in order to conduct a Weibull analysis. The specimens were tracked throughout fabrication and testing in order to evaluate the variation in toughness across different rods and location within a rod.

Notch toughness tests were carried out according to ASTM Standard E399 [121].

[1]Materion Corporate Headquarters 6070 Parkland Blvd., Mayfield Heights, OH 44124.

This test method is considered appropriate because in earlier work by the authors shows that $Cu_{43}Zr_{43}Al_7Be_7$ meets plane strain conditions for the sample geometry used [167]. Notch toughness was measured using a four-point bend setup on a screw-driven 5980 Instron load frame with a displacement rate of 0.1 mm/min. The inner and outer spans of the four-point bend fixture were 8 mm and 16 mm, respectively. A notch was cut in the center of each specimen using a low speed diamond saw to a depth 0.4–0.5 times the diameter with a root radius of 90 $\mu$m. The notch toughness, $K_{IC}$, was calculated from the critical fracture load using Kiuchi's finite element modeled stress intensity factor for a notched round rod [122]. Details regarding the equation used to calculate $K_{IC}$ for this specific geometry and loading conditions are described in Ref. [167] and complete detail on the calculation can be found in App. A.

Three cross-sections cut from the location near the point of fracture in each rod were cold-mounted and polished to a final step with a 0.05 $\mu$m silica solution. The amorphous structure was characterized using a Rigaku Rotoflex X-ray diffractometer (XRD) with Cu K$\alpha$ radiation, an X-ray operating voltage of 40 keV, a current of 140 mA, a step size of $0.02^\circ$ and a dwell time of 15 s.

The microstructures were examined with an Olympus GX51 light optical microscope equipped with differential interference contrast (DIC). To make a qualitative assessment of the percent crystallization, ImageJ software was used to select and calculate the area fraction of particular threshold levels. The topography was further imaged at 20 kV in an FEI Quanta 600 scanning electron microscope (SEM) equipped with energy-dispersive X-ray spectroscopy (EDS). Imaging with the backscattered electron

detector at a tilt angle of 30° reduced the beam interaction volume and enhanced the topography created by hard crystalline regions. Selective EDS point analysis (an average of three areas) was used to identify the composition of the amorphous matrix and the crystalline particles.

Furthermore, the reliability of the toughness of $Cu_{43}Zr_{43}Al_7Be_7$ made with high purity zirconium crystal bar was analyzed in the framework of Weibull statistics. A total of 27 fracture toughness tests were used in the analysis for each, the laboratory and commercially-produced $Cu_{43}Zr_{43}Al_7Be_7$ made with high-purity Zr crystal bar.

The Weibull equation describes the fracture probability, $P_f$, for a given uniaxial stress, $\sigma$ (or in this case, fracture toughness, $K_{IC}$). The 3-parameter Weibull equation is:

$$P_f = 1 - \exp\left[-\left(\frac{\sigma - \sigma_u}{\sigma_0}\right)^m\right] \tag{4.1}$$

where $\sigma_0$ is the scale parameter, $m$ is the Weibull modulus or shape parameter, and $\sigma_u$ is the location parameter, which denotes the stress where the probability of failure is zero.

When $\sigma_u = 0$, Eq. 4.1 reduces to a 2-parameter Weibull distribution. Because it is very risky to assume a finite threshold strength without careful screening or non-destructive evaluation, a 2-parameter model is usually used as a safe assumption. Many studies on BMGs have taken this approach [68, 69], while others argue that a 3-parameter model is more appropriate [70, 71]. Numerical simulations and experimental data show that, if sample data are limited in number ($N \leq 40$) and the location parameter, $\sigma_u$, is not too large, the 2-parameter Weibull distribution is the preferred model [72]. Thus, in this

work, a 2-parameter Weibull analysis is implemented.

The parameters of a 2-parameter Weibull distribution can be obtained by linearizing Eq. 4.1 and setting $\sigma_u = 0$:

$$y_i = \ln\left\{\ln\left[\frac{1}{(1-P_{f,i})}\right]\right\} = m\ln\sigma_i - m\ln\sigma_0 = mx_i - m\ln\sigma_0 \tag{4.2}$$

In a double-logarithmic plot of $\ln(\ln(1/(1-P_f)))$ plotted against $\ln\sigma$, the Weibull modulus, $m$, is the slope, and the scale parameter, $\sigma_0$, is obtained from the $y$-intercept.

## 4.4 Results

### 4.4.1 Chemical Composition

The nominal compositions for the alloys investigated are listed in Table 4.1. Alloys A–C were synthesized by the authors using varying amounts of high-purity Zr and standard grade Zr lump, which contains up to 4% Hf. The Hf content in the samples containing the Zr lump was determined using an average of five EDS measurements. In Alloys B and C, the Hf content was measured to be 0.24–0.44 at%, respectively, with a standard error of 0.01 in both cases. Compare this to the maximum possible Hf content. Assuming a maximum of concentration of 4 at% Hf in the zirconium lump, the Hf concentration in Alloy B and C would be 0.86 and 1.72 at%, respectively. This means the zirconium lump used in these experiments had less than the maximum allowed hafnium

impurity. The estimated amount of hafnium impurity in the zirconium lump used in this experiment is about 1 at%. For this reason, Alloy D was made using high purity Zr and an additional 0.5 at% high purity hafnium. The Hf concentration was confirmed by EDS to be within 0.02 of the nominal composition. Alloy E was synthesized using high purity Zr and supplied by Materion Corporation™[2]. No Hf was detected in Alloy A or E, the two, high-purity Zr only, containing samples.

**Table 4.1**: Nominal composition of the BMG alloy ingots studied, the elemental Zr and Hf (if applicable) metals used, and the synthesis method.

| Alloy | Elements | Synthesis method | Nominal composition (at%) [a] |
|---|---|---|---|
| A | Zr crystal bar, 99.5% pure | Laboratory, 15 g ingots | $Cu_{43}Zr_{43}Al_7Be_7$ |
| B | ½ Zr crystal bar, ½ Zr lump | Laboratory, 15 g ingots | $Cu_{43}Zr_{42.14}Al_7Be_7Hf_{0.24}$ |
| C | Zr lump, 99.8% excluding up to 4% Hf | Laboratory, 15 g ingots | $Cu_{43}Zr_{41.28}Al_7Be_7Hf_{0.44}$ |
| D | Zr crystal bar, 99.5% pure + Hf wire, 99.7% excl. up to 3% Zr | Laboratory, 15 g ingots | $Cu_{43}Zr_{42.5}Al_7Be_7Hf_{0.50}$ |
| E | Zr crystal bar, 99.5% pure | Materion Corp.™, >15 kg ingots, recast as 15 g | $Cu_{43}Zr_{43}Al_7Be_7$ |

[a] Hf based on average of five EDS measurements in final specimens.

### 4.4.2 Glass-Forming-Ability

The XRD patterns of the $Cu_{43}Zr_{43}Al_7Be_7$ 3 mm BMG rods are shown in Fig. 4.1a. Alloy A and D appear to be primarily amorphous, based on the broad hump in the XRD pattern that has no indication of defined peaks. On the other hand, both Alloy B, C and E have distinct peaks overlaid on an amorphous background. This suggests that using

[2]Materion Corporate Headquarters 6070 Parkland Blvd., Mayfield Heights, OH 44124.

cost-effective hafnium-containing zirconium or a commercial scale synthesis method, decreases the glass-forming-ability of $Cu_{43}Zr_{43}Al_7Be_7$.

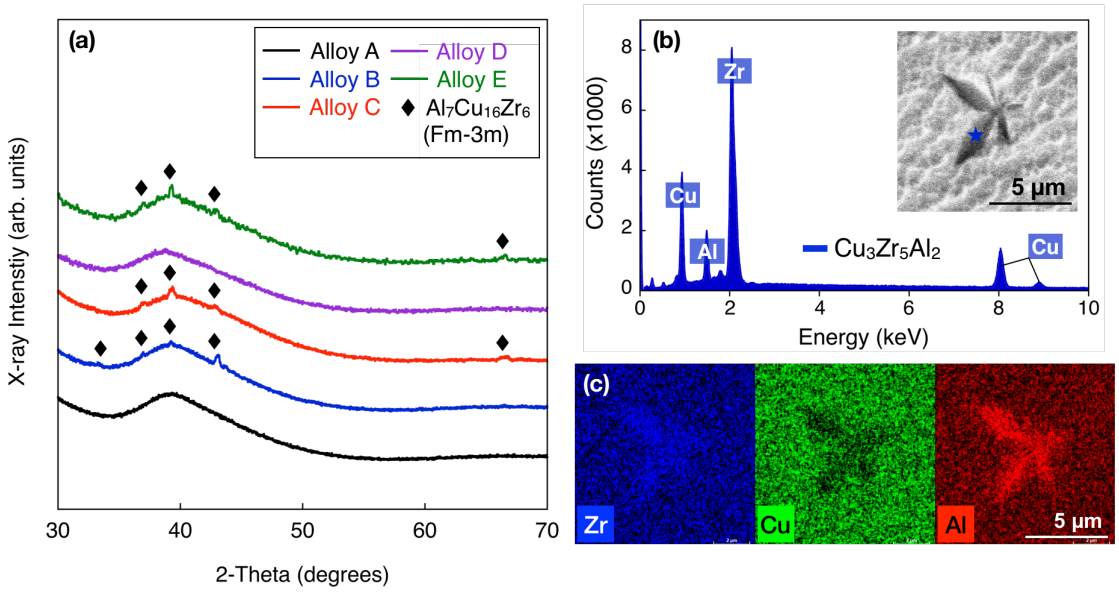


**Figure 4.1**: $Cu_{43}Zr_{43}Al_7Be_7$ 3 mm BMG rods with varying amounts of hafnium. (a) XRD patterns taken with a dwell time of 15 s. Alloy A was made with Zr crystal bar, Alloy C was made with Zr lump (incl. up to 4 at% Hf) and Alloy B was made using half the amount of each. Alloy D was made using Zr crystal bar and 0.5 at% high-purity Hf. The crystalline peaks along the amorphous background show that low purity zirconium (containing Hf) decreases the glass-forming-ability of $Cu_{43}Zr_{43}Al_7Be_7$. (b) EDS spectrum corresponding to the measured crystalline phase of $Cu_{3.1}Zr_{5.5}Al_{1.5}$. The back-scattered SEM image in the inset shows the location where the analysis was taken. (c) EDS map of the same crystal in the inset in (b), which shows that the crystalline phase is Zr-rich and Al-rich and Cu deficient relative to the matrix.

The peaks in the XRD pattern correspond to $Al_7Cu_{16}Zr_6$ in the ICDD PDF-4+ X-ray database. However, EDS analysis confirms an average composition of $Cu_{3.1}Zr_{5.5}Al_{1.5}$, excluding Be and trace amounts of Hf. The exact composition of the crystal could not be determined due to instrument limitations on obtaining a quantitative atomic percent for beryllium. Nevertheless, this composition is very close to the metastable $\tau_3$ phase $Cu_3Zr_5Al_2$. An EDS map and corresponding point analysis spectrum are included

in Fig. 4.1b–c. In previous work, these authors have identified this same beryllium containing $\tau_3$ phase in $Cu_{43}Zr_{43}Al_7Be_7$ and confirmed it to have an $Fm\bar{3}m$ structure that matches closely with $Al_7Cu_{16}Zr_6$ [167]. Therefore, the crystalline peaks in the XRD patterns are expected to correspond to a $Cu_3Zr_5Al_2$ crystalline phase containing beryllium and trace amounts of hafnium as labeled in Fig. 4.1a.

Moreover, the decrease in glass-forming-ability is also visible in an analysis of differential image contrast (DIC) images. Select images are shown in Fig. 4.2a–o that best represent the overall microstructure for each type of sample. Fig. 4.2a–c correspond to $Cu_{43}Zr_{43}Al_7Be_7$ made with high purity zirconium crystal bar. The XRD pattern in Fig. 4.1a suggests that the sample is entirely amorphous, but DIC imaging reveals small crystalline particles are dispersed across the amorphous matrix. It is possible that using a longer dwell time for the XRD measurement would allow for detection of these small regions of crystallization, but the limitations of X-ray diffraction for identifying small crystalline volume fractions should also be acknowledged. Fig. 4.2d–f and Fig. 4.2g–i show the images corresponding to Alloy B and C, respectively. The significant amount of crystallization seen in Alloy B and C in comparison to Alloy A confirms that by introducing Zr(+4% Hf max) lump into $Cu_{43}Zr_{43}Al_7Be_7$, the glass-forming-ability decreases. The structure of Alloy D, shown in Fig. 4.2j–l, appears similar to Alloy A. Once again, the small amount of crystallization is not detectable using XRD with the given operating parameters. On the other hand, Fig. 4.2m–o show DIC images of Alloy E. The amount of crystallization in the commercial sample appears to be somewhere in between that of the high purity samples (Alloy A and D) and those with

Hf impurities (Alloys B and C).

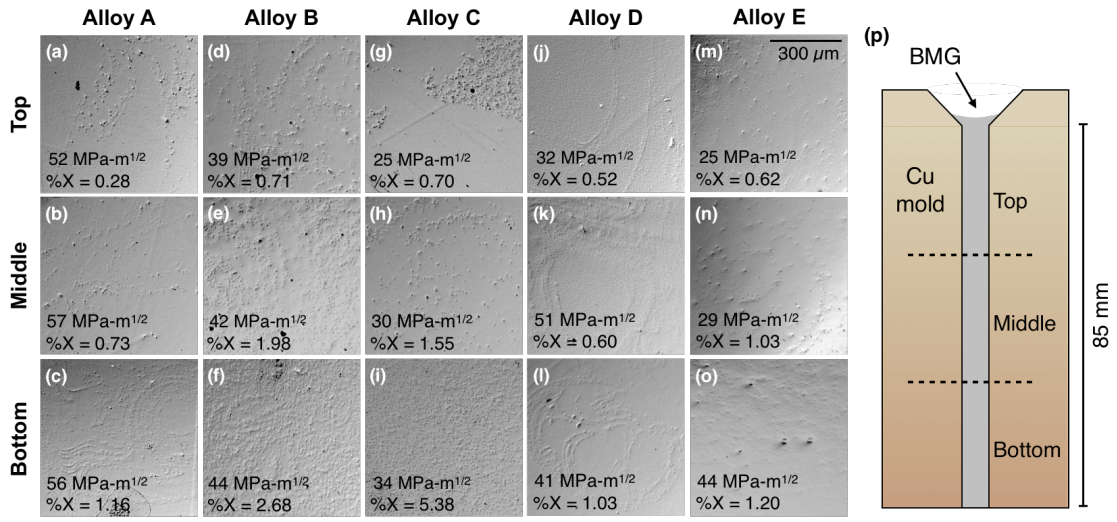


**Figure 4.2**: Optical microscope images taken with DIC showing the variation in crystallization among different alloy compositions. (a–c) Alloy A has very little crystallization at all locations along the rod. (d–f) Alloy B has a large variation in crystallization amount based on the location in the rod. (g–i) Alloy C has the largest amount of crystallization and it also varies significantly based on location. (j–l) Alloy D has a similar amount of crystallization to that of Alloy A. This suggests that the small Hf addition itself does not alter the glass-forming-ability. (m–o) Alloy E showing a slight decrease in glass-forming-ability. Quantitative crystalline volume fraction calculations based on threshold optimized images are shown for each image. The crystalline volume fraction significantly increases with any amount of zirconium lump (Alloys B and C). There is little difference in the crystalline content between Alloy B and C. (p) Schematic diagram illustrating the rod suction casting mold.

The average crystalline volume fraction was calculated by optimizing the threshold values in the DIC images. The results are plotted in Fig. 4.3a with the interquartile range marked by a shaded box. Alloy A and D have very little crystallization, about 0.7% and 0.5%, respectively. As comparable to the XRD results, Alloys B, C and D have more crystallization at 3.32, 3.75, and 1.87, respectively. Applying Welch's *t*-test for unequal variances, reveals that the volume fraction of crystallization in Alloy A and D is significantly less than that in Alloys B and C. On the other hand, Alloy E is significantly

different from all others, lying somewhere in-between the two pairs.

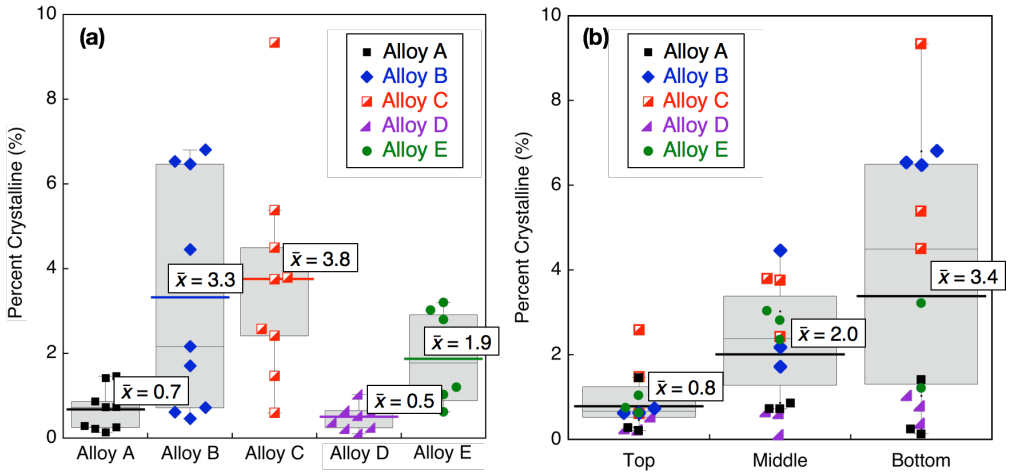


**Figure 4.3**: Variation in crystalline volume fraction for each alloy and specimen location during casting. (a) Variation in crystalline volume fraction in each $Cu_{43}Zr_{43}Al_7Be_7$ alloy. Using Zr lump rather than high purity Zr significantly increases the amount of crystallization (Alloys B and C). Additions of high purity Hf do not have a significant effect on the glass-forming-ability (Alloy D). But high purity samples produced using a large scale synthesis process (Alloy E) exhibit a decrease in glass-forming-ability. (b) Crystalline volume fraction calculation as a function of specimen location in the mold during casting, showing that the specimens at the bottom of the mold developed the most crystallization. According to Welch's *t*-test, the difference in crystalline percent between the top and middle specimens is not statistically significant, although a trend does emerge.

With closer inspection of the DIC images in Fig. 4.2, it appears that the amount of crystallization also varies based on the location of the specimen in the rod. Fig. 4.2p shows a schematic of the as-cast rods, indicating where each specimen was cut. The rods were cast vertically into a copper-mold, and each rod was large enough to be cut into three specimens, thus the cooling rate could differ between specimens. The images in the top row of Fig. 4.2 are cross-sections from specimens taken from the top third portion of the as-cast rod. Likewise, the middle row images are taken from the middle portion of the rod, and the bottom row images are from the bottom third. The statistics

of crystallization based on the location of the specimen are shown in Fig. 4.3b, which suggest that crystallization increases toward the bottom of the as-cast rod. However, due to the large error in the crystalline percent analysis, only the bottom specimens have a significantly larger amount of crystallization relative to the top and middle.

### 4.4.3 Notch Toughness

The average notch toughness for each alloy type is shown in Fig. 4.4. The notch toughness of $Cu_{43}Zr_{43}Al_7Be_7$ significantly decreases due to replacing high purity zirconium crystal bar with a lower purity zirconium lump. Alloy A, made using high purity zirconium crystal bar, has the highest toughness with an average of ~53 MPa-$m^{1/2}$ and a standard deviation of 14 MPa-$m^{1/2}$. Alloy B, which has half zirconium crystal bar and half hafnium-containing zirconium lump, has a reduced notch toughness of ~41 MPa-$m^{1/2}$ with a standard deviation of 6 MPa-$m^{1/2}$. Alloy C, which is made using only hafnium-containing zirconium lump, has a notch toughness of ~29 MPa-$m^{1/2}$ and a standard deviation of 5 MPa-$m^{1/2}$. By substituting high purity zirconium in $Cu_{43}Zr_{43}Al_7Be_7$ with the more economical hafnium-containing zirconium the notch toughness is reduced by over 40%. Alloy D, made with high purity Zr and high purity Hf has a notch toughness of ~45 MPa-$m^{1/2}$ and a standard deviation of 3 MPa-$m^{1/2}$. The difference in notch toughness due to simply the presence of Hf (Alloy A and D) is not significant. Alloy E, made with high purity Zr and synthesized using a different large-scale process, has a notch toughness of ~33 MPa-$m^{1/2}$ with a standard deviation of 6 MPa-$m^{1/2}$. Although Alloy A has the highest toughness, the variation in toughness

across the ingot is wide. Thus, a Weibull analysis, as presented in the next section, will provide insight into the reliability of the toughness measurements of the BMG $Cu_{43}Zr_{43}Al_7Be_7$.

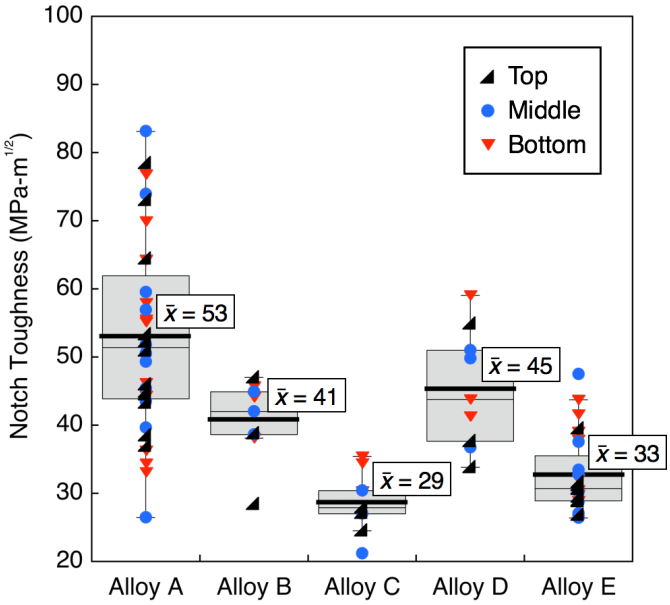


**Figure 4.4**: Notch toughness of $Cu_{43}Zr_{43}Al_7Be_7$ based on zirconium source and synthesis process as shown in Table 4.1. As the amount of low-purity zirconium lump increases, the toughness significantly decreases. Furthermore, a large-scale synthesis process creates a similar reduction in toughness.

The notch toughness correlates with both the final amorphous matrix composition after in-situ crystallization and the percent volume fraction of crystallization. Fig. 4.5a shows that as the amount of Cu in the matrix increases, the notch toughness decreases. This is not surprising because due to the in-situ crystallization in the specimen, the amorphous composition is no longer composed of $Cu_{43}Zr_{43}Al_7Be_7$ as intended. Rather, as Cu-deficient $Cu_3Zr_5Al_2$ crystalline regions develop, the amount of copper remaining in the matrix increases. On the other hand, a similar trend is noticed where the toughness decreases with an increase in volume fraction of crystallization, as shown in Fig. 4.5b.

In particular, there is a sharp decrease in toughness of at least 25% with only 1% crystallization.

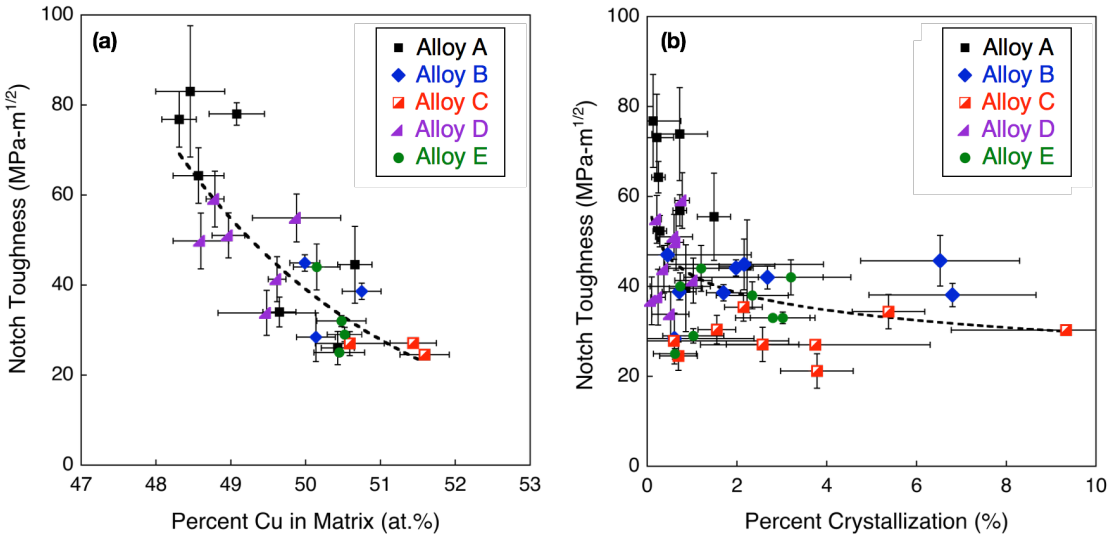


**Figure 4.5**: Variation in notch toughness of $Cu_{43}Zr_{43}Al_7Be_7$ as a function of (a) percent copper in the matrix and (b) percent crystallization. As the amount of crystallization in the BMG increases, the matrix composition changes due to the preferential formation of the crystalline phase $Cu_3Zr_5Al_2$.

### 4.4.4 Weibull Statistics

The Weibull statistics of $Cu_{43}Zr_{43}Al_7Be_7$ were calculated to better understand the variability in toughness. The toughest composition, Alloy A, made with high purity zirconium, was used for this portion of the study. Furthermore, to gain insight into the effect of the manufacturing process on the variability in BMG properties, commercially-prepared ingots made with high purity Zr (Alloy E) were also included in the study.

The 2-parameter Weibull plot, a double-logarithmic plot of $\ln(\ln(1/(1-P_f)))$ plotted against $\ln\sigma$, for each set of samples is presented in Fig. 4.6a. The equation for the linear regression line in Fig. 4.6a has the same form as Eq. 4.2, and it was used to

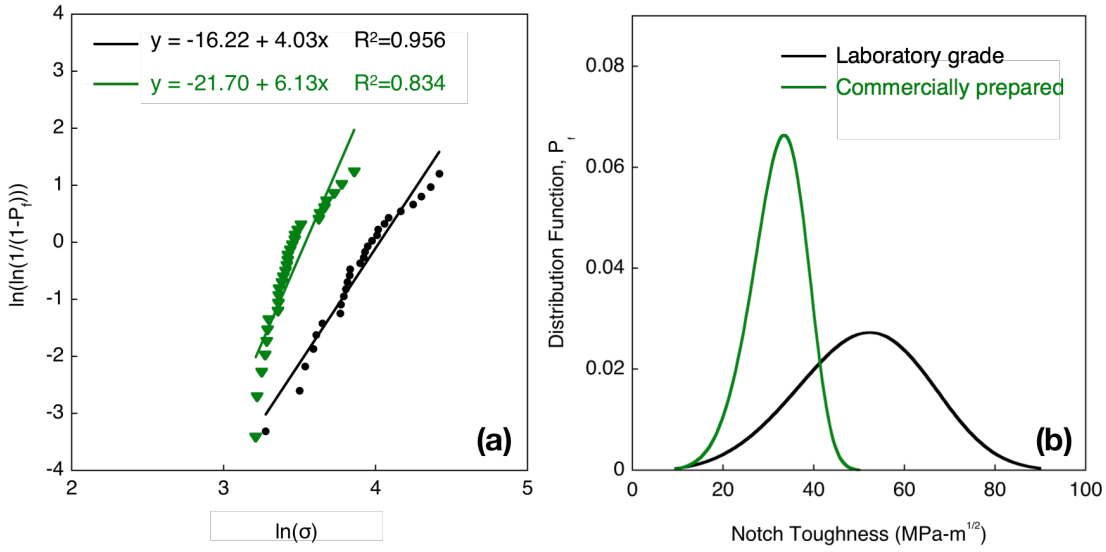


**Figure 4.6**: (a) 2-parameter Weibull plot and (b) Weibull probability density function for the notch toughness of $Cu_{43}Zr_{43}Al_7Be_7$ made with high purity zirconium. Two different material sources were compared: ingots synthesized in a small laboratory arc-melter and ingots commercially-prepared by an undisclosed procedure.

determine the necessary parameters as previously described. For the laboratory prepared samples, the Weibull modulus, $m$, was found to be 4.03 and the shape parameter, $\sigma_0$, was determined to be 56.2 MPa-m$^{1/2}$. In contrast, the commercially-produced samples have a Weibull modulus, $m$, of 6.13 and a shape parameter, $\sigma_0$, of 34.5 MPa-m$^{1/2}$. These parameters define the Weibull probability density function, which is given by:

$$f(x) = \frac{m}{\sigma_0}\left(\frac{x}{\sigma_0}\right)^{m-1} \exp\left(-\left(\frac{x}{\sigma_0}\right)^{m}\right), \tag{4.3}$$

and is shown for each set of samples in Fig. 4.6b.

## 4.5 Discussion

### 4.5.1 Effect of Impurities on Glass-Forming-Ability

In this study it is shown that using zirconium lump with hafnium impurities in place of high purity Zr significantly degrades the glass-forming-ability of $Cu_{43}Zr_{43}Al_7Be_7$. Furthermore, adding 0.5 at% high purity Hf to high purity $Cu_{43}Zr_{43}Al_7Be_7$, has little effect on the GFA. For many applications, small amounts of hafnium impurities in pure zirconium may be deemed acceptable and provide for cost savings. Unfortunately, the cost effective lower grade Zr decreases the GFA, which is expected to be due to other impurities in the materials, such as oxygen.

To further evaluate the GFA behavior in this study, a theoretical evaluation was carried out using comprehensive modeling criteria in incorporating several techniques [168]. The tool relies the liquidus temperature, the depth of eutectics as measured by the parameter, and the calculation of the chemical-short-range-order (CSRO) [168]. The model predicts that small substitutions of Hf for Zr have little effect on glass-forming-ability of $Cu_{43}Zr_{43}Al_7Be_7$, and this result compares will with the results of the high purity samples in this study (Alloy A and D).

The observed reduction in GFA due to Zr lump is expected to result from other impurities in the zirconium lump; for example, oxygen. A certain level of oxygen in Zr-based BMGs coming from raw materials or processing atmosphere is expected and unavoidable due to the very strong affinity between zirconium and oxygen. The nominal oxygen content in the high purity Zr crystal bar obtained from Alfa Aesar (product

#10444) is less than 103 ppm, although the majority of lots contain closer 50 ppm. Moreover, an oxygen analysis is not reported for zirconium lump (product #36253), but it is produced by vacuum melting, and the oxygen content is expected to be low (~100 ppm).

Previous studies have shown that the glass-forming-ability of Zr-based BMGs is strongly dependent on the oxygen concentrations. Oxygen concentrations greater than ~2000 ppm in Zr-based BMGs have been shown to significantly decrease the critical casting diameter [115, 169]. An increase in the oxygen content beyond ~6000 ppm may also trigger the formation of metastable crystalline phases that are not seen in alloys with lower oxygen impurities [170,171]. On the contrary, the aforementioned studies observed a good glass-forming-ability where the oxygen content was less than ~500 ppm. The effect of oxygen and other impurities in standard grade zirconium on the GFA of BMGs is an important topic to address. Thus, further studies on this topic are recommended in order to gain a clearer understanding of this behavior.

### 4.5.2 Effect of Crystallization on Toughness

The reduction in toughness is discussed with the consideration of three important factors: the properties and volume fraction of the crystalline phase formed, the changing composition of the glassy phase, or the strength of the interface between the crystalline phase and the matrix.

In this report, as the volume fraction of the crystalline phase increases, the toughness decreases, as shown in Fig. 4.5b. This finding is compared with a previous

study finding that crystallization in $Zr_{44}Ti_{11}Cu_{10}Ni_{10}Be_{25}$ exceeding ~6%, caused a dramatic drop in fracture toughness, reducing the fracture toughness by 50% [145]. Although a steep drop in the fracture toughness is observed here, it occurs at a much lower estimated crystalline volume fraction. It is possible that the DIC threshold image analysis resulted in an underestimation of crystallization percent. The procedure was designed as a relative comparison between samples within this study. Nevertheless, there is significant error in the calculated crystalline volume fractions due to the subjective nature of identifying the crystalline phase, and the variation in microstructure across many of the cross-sections.

Besides the crystalline phase fraction, the varying composition in the matrix due to the selective crystallization process may also have a profound impact on toughness. With a composition difference between the crystals and the glassy matrix, the composition of the matrix must change during crystallization. In a couple of previous reports, an increase in overall hardness was observed with an increasing small volume fraction of a crystalline phase, which was attributed, at least in part, to composition changes in the glassy matrix [153]. In Fig. 4.5a, the decreases in toughness correlate with the remaining copper in the amorphous matrix. Although the degree that the matrix composition contributes to the decrease in toughness is unclear, the correlation seems stronger than with the percent volume fraction of crystalline phase. To verify this observation, a more objective crystalline volume fraction calculation would be necessary. Nevertheless, it is demonstrated that EDS analysis of the matrix composition is an efficient and reliable test method to characterize the toughness of a partially-crystalline BMG.

To verify the hardness of each phase, Vickers' microhardness measurements were taken at a load of 10 gf for 15 s to ensure that the indent size was small enough to independently characterize the amorphous region and microscale crystals. From an average of three points, the hardness of the amorphous matrix and the crystalline phase was found to be 597 $\pm$ 27 and 767 $\pm$ 34, respectively. When the crystalline particles are harder than the matrix, the secondary phase carries higher loads than the matrix, and stresses are therefore reduced in the matrix for the same far-field stress. This may delay shear band formation before eventual fracture and, hence, increase toughness [145]. However, this result assumes a perfect interface. If stress concentrations exist at the interface between the amorphous matrix and the crystal, embrittlement may occur. It is interesting to note that although the amount of crystallization varies significantly at different locations in the rods in Alloys B and C, the notch toughness variation is fairly independent of the amount of crystallization.

To investigate the effect of the matrix-crystal interface, Vickers' indentation marks were made in the matrix in close proximity to a crystal. Due to the relatively high toughness of the amorphous phase, cracking at the indent tip was difficult to achieve. However, with sufficient indents in one location, the stress field became large enough that cracks emerged from the indent side occurring in the form of semi-circular cracks. Many different interactions between the cracks and crystals were observed. Fig. 4.7a shows a schematic drawing of the indent orientation necessary to consistently produce cracks in the vicinity of an identified crystal. Furthermore, the left side of Fig. 4.7b shows a crack extending from an indent corner and branching around a small crystal. The right

side of Fig. 4.7b shows evidence of shear bands produced due to the compressive force of the Vickers' indents on either side. Fig. 4.7c shows a crack that branched toward a crystal and passed right thorough it. In Fig. 4.7d, a crack is seen propagating along the interface between the crystal and the amorphous matrix, and in Fig. 4.7e, a crack has traveled through the crystal without any deflection or bifurcation. It is interesting to consider how the properties of each phase may be affected by the dispersion of crystals. Based on the interactions in Fig. 4.7a–b, it is likely that the operation of shear bands is affected by the presence of crystallite. However, further investigations are needed to show whether $Cu_3Zr_5Al_2$ in-situ crystallization in $Cu_{43}Zr_{43}Al_7Be_7$ can impeded shear band propagation during deformation.

### 4.5.3 Weibull Statistics for Reliability

The glassy structure of BMGs gives them extremely low tolerance to the presence of flaws. This is apparent by that fact that the samples in this study (especially Alloy A) exhibit significant variability in their toughness. Although a high average toughness of ~53 MPa-$m^{1/2}$ suggests that the alloy is resistant to crack initiation, once a crack or shear band begins to propagate, catastrophic failure proceeds immediately. The high scatter arises based on the statistical probability of a crack or shear band to propagate. This presents a major challenge for engineers to predictably and safely design components using BMGs. Therefore, it is important to address the statistical reliability of BMGs if they are to be used in engineering design.

In this work, it is found that the 2-parameter Weibull modulus for the fracture

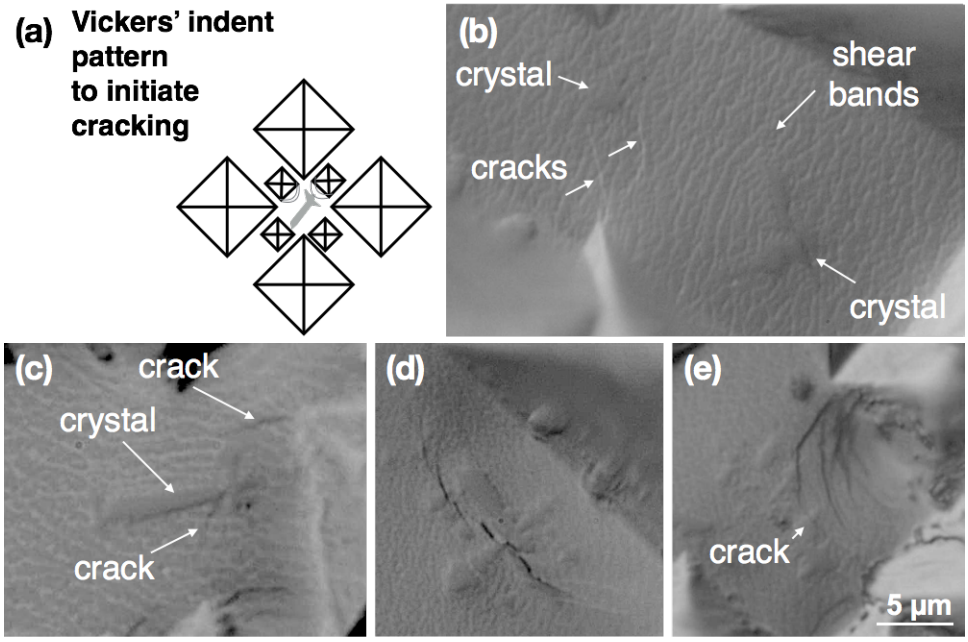


**Figure 4.7**: (a) Schematic drawing of the indent orientation necessary to consistently produce cracks in the vicinity of an identified crystal. (b–e) Optical microscope images of interactions between induced cracking and in-situ crystallization. (b) Cracks branching around a crystal ~3 $\mu$m wide, and evidence of strain localization as the crystal is compressed between two Vickers' indents. (c) Crack branching through a crystal where the crack branched toward the crystal. (d) Crack propagating along the crystal-matrix interface. (e) Crack propagating through a crystal, which appears to be unaffected by the presence of the crack.

toughness of $Cu_{43}Zr_{43}Al_7Be_7$ synthesized in a small laboratory arc-melter is ~4. Comparatively, this is quite low, suggesting that the fracture exhibits low reliability. The Weibull modulus reflects the degree of variation in the toughness of the samples tested. A higher Weibull modulus represents a very narrow dispersion in strength, whereas a low value suggests a wide dispersion [68]. For example, Weibull moduli for the strength of ductile crystalline metals are typically on the order of ~100 and that of brittle engineering ceramic materials are in the order of ~5 [172]. If the Weibull moduli is very low, such as <5, tensile loading on the material is typically avoided in engineering designs.

In this work, it is shown that the commercially-prepared alloys have a slightly

higher 2-parameter Weibull modulus than that of the laboratory prepared samples. This is attributed to the more consistent synthesis process used commercially. The Weibull modulus is highly dependent on the processing conditions, including both the alloy synthesizing method and the casting conditions. Homogeneity may be promoted by the large-scale processing method used to synthesize the BMG ingots on a commercial scale. By comparison, the alloys synthesized in the laboratory were individual ingots no larger than 20 g. The one-step copper-mold casting process was held constant for all samples in this experiment. However, the effect of casting conditions on the Weibull modulus of BMGs is an interesting and valuable direction of study.

However, the characteristic fracture toughness of the commercially-prepared samples is much lower than that of the laboratory-produced samples. It is possible that the reduced toughness is attributable to the purity of the elements used or, potentially, to oxygen contamination during synthesis. It would be an interesting problem to solve, in order to obtain high toughness $Cu_{43}Zr_{43}Al_7Be_7$ BMGs with improved reliability. In support of this effort, it should be mentioned that the Weibull modulus remains unchanged as toughness is increased [173]. Thus, the problem of flaw sensitivity could, in principle, be handled by understanding, and designing for, statistical variations in the toughness of BMGs.

## 4.6 Conclusions

In summary, it has been shown that using standard grade zirconium lump (99.8% excluding up to 4% hafnium) in place of high purity zirconium crystal bar (99.5%) in a $Cu_{43}Zr_{43}Al_7Be_7$ bulk metallic glass (BMG) decreases its glass-forming-ability and toughness. Using high purity zirconium crystal bar, the notch toughness of $Cu_{43}Zr_{43}Al_7Be_7$ is ~53 MPa-$m^{1/2}$, with half zirconium crystal bar and half hafnium-containing zirconium lump, the resulting notch toughness is ~41 MPa-$m^{1/2}$, and when using only hafnium-containing zirconium lump, the resulting notch toughness is ~29 MPa-$m^{1/2}$. Moreover, when adding small amounts of high purity Hf to high purity $Cu_{43}Zr_{43}Al_7Be_7$, the resulting notch toughness is ~45 MPa-$m^{1/2}$ and not a statistically significant reduction in toughness as compared to the high purity sample without Hf. Thus, 0.5 at% Hf has little effect on the GFA and toughness of $Cu_{43}Zr_{43}Al_7Be_7$. On the other hand, standard grade Zr with Hf impurities does significantly reduce the glass-forming-ability and toughness. The change is attributed to other impurities in the elemental zirconium lump.

The crystalline phase formed in-situ was determined through EDS to be $Cu_3Zr_5Al$. Both the volume fraction of crystalline phase and the change in composition of the amorphous matrix scaled with the reduction in toughness. With ~2% crystalline volume fraction the toughness decreases by about 50%. However, the volume fraction calculation may be underestimated due to the large variation in the image analysis measurement. On the other hand, the toughness decreases as the percent Cu in the matrix increases. This is a much less subjective measurement and a better method to evaluate the toughness

using structural-property relationships. Further work is needed to clarify whether the volume fraction of crystalline phase or the change in composition of the amorphous matrix controls the reduction in toughness.

Finally, the 2-parameter Weibull statistics of $Cu_{43}Zr_{43}Al_7Be_7$ with high purity zirconium are presented. Two synthesis methods are compared: ingots synthesized in a small laboratory arc-melter and material synthesized at the commercial-scale. The commercial alloys have a Weibull modulus and characteristic toughness of ~6 and 34.5 MPa-$m^{1/2}$, respectively. Compare that to the Weibull modulus and characteristic toughness of the laboratory ingots, which are ~4 and 56.2 MPa-$m^{1/2}$, respectively. The higher Weibull modulus of the commercial material is attributed to the large-scale synthesis method, whereas the higher characteristic toughness of the laboratory ingots is attributed to higher purity of the BMGs.

## 4.7 Acknowledgements

Financial support from the Achievement Rewards for College Scientists (ARCS) Foundation is gratefully acknowledged. D. C. Hofmann acknowledges financial support from NASA's Science Mission Directorate and Space Technology Mission Directorate through the Game Changing Development program under Prime Contract #NAS7-03001and from the Presidential Early Career Award. Part of this research was done at the Jet Propulsion Laboratory, California Institute of Technology, under contract with NASA.

Chapter 4, in full, is a reprint of the material as it appears in Materials Science and Engineering: A. Andersen, Laura; Hofmann, Douglas; Vecchio, Kenneth, Elsevier B.V., 2016. The dissertation author was the primary investigator and author of this material.

# 5 Summary and Future Directions

The primary aim of this work was to identify wear-resistant bulk metallic glasses and study the relationships between the processing, structure and mechanical properties in these unique alloys. Rather than taking the traditional approach of applying the well-studied alloy, Vitreloy, the work presented here focuses on a specific material class for a well-defined application (i.e. wear-resistant gears). The work includes a comprehensive and systematic wear study, an investigation into the toughness of Cu-Zr-based BMGs, and a closer look at the effects of processing on the toughness in this BMG system. All the work presented here has either been published or is in the process of being published; and therefore, provides a large quantity of good data that is available to the public and can lead to advancements in the field of BMGs.

In Chapter 2, Cu-Zr-based alloys are identified as high-glass-forming alloys with excellent wear properties. Furthermore, the wear-resistant Cu-Zr-based alloys could serve as a competitive material replacement for long-life, low-torque gears. Compared to a current state-of-the-art gear material, Vascomax C300, $Cu_{43}Zr_{43}Al_7Be$ exhibits over 50% improvement in unlubricated wear-resistance. Rigorous testing in custom gear-on-gear

testing identifies the importance of toughness to maximize the wear-resistance and life of a bulk metallic glass gear. Net-shaped casting is shown to be a viable and low-cost method to systematically produce a series of bulk metallic glass gears.

In Chapter 3, it is shown that partial crystallization in Cu-Zr-BMGs can be difficult to identify using standard XRD methods. Furthermore, the toughness of partially-crystalline $Cu_{43}Zr_{43}Al_7Be$ is investigated with respect to the structure and composition of the in-situ composite. The toughness is found to decrease as the matrix composition travels further from the intended high glass forming composition. Notwithstanding, partially-crystalline $Cu_{43}Zr_{43}Al_7Be_7$ exhibits notch toughness of ~54 MPa-$m^{1/2}$. The crystalline phase, identified as $Cu_3Zr_5Al_2$(+Be) by EDS, exhibits a higher hardness than the amorphous matrix, revealing its potential contribution to the enhanced wear-resistance of the BMG. EBSD and XRD, identified a specific cubic $Fm\bar{3}m$ structure similar to the structure of $Al_7Cu_{16}Zr_6$, but with the composition consistent with a $Cu_3Zr_5Al_2$(+Be) phase. To produce a wear-resistant Cu-Zr-based BMG with high toughness, the nominal alloy composition should be designed to maximize the plasticity and fracture resistance of the remaining matrix composition after in-situ crystallization. An opportunity exists to optimize the wear-resistance of these materials, by forming a high volume fraction of very small crystalline particles, with a matrix composition driven towards $Cu_{43}Zr_{43}Al_7Be_7$.

Finally, Chapter 4, includes a study on the effect of standard-grade zirconium and a commercial-scale synthesis method on the GFA and toughness of $Cu_{43}Zr_{43}Al_7Be_7$. Using high purity zirconium crystal bar, the notch toughness of $Cu_{43}Zr_{43}Al_7Be_7$ is as high as ~53 MPa-$m^{1/2}$, and an addition of 0.5 at% Hf has little effect on the GFA and

toughness. On the other hand, standard-grade Zr with Hf impurities significantly reduces the GFA and toughness, which is attributed to other impurities (such as oxygen) in the standard-grade zirconium lump. Similarly, a large commercial-scale synthesis method leads to a decrease in the GFA and toughness. However, a 2-parameter Weibull analysis shows that the material synthesized at the commercial-scale has greater reliability than the ingots synthesized in a small laboratory arc-melter. The commercial alloys have a Weibull modulus and characteristic toughness of ~6 and 34.5 MPa-$m^{1/2}$, respectively. Compare that to the Weibull modulus and characteristic toughness of the laboratory ingots, which are ~4 and 56.2 MPa-$m^{1/2}$, respectively.

Promising directions of future research include additional investigations on the net-shaped casting of gears, optimizing the toughness of $Cu_{43}Zr_{43}Al_7Be_7$ through computational alloy design and correlating wear-resistance to the crystalline volume fraction. Further work on the net-shaped casting of gears (both spur gears and strain wave gears) is already underway at NASA's Jet Propulsion Laboratory.

# A Stress Intensity Factor Calculation for a Notched Round Rod

Material fractures begin at the location where the stress concentration is highest. In the case of a notched rod, the highest stress concentration is at the tip of the notch or sharp crack. Here, the stress state is a function of the applied stress and the crack length, and it is described by the stress intensity factor, $K_I$ [174]. The subscript describes the loading mode, and in this example we assume a mode I (opening) fracture; hence $I$ is used as the subscript. When a failure occurs, the stress-intensity factor has reached its critical value, $K_{IC}$, referred to as the fracture toughness of the material. The fracture toughness is a material constant defined as

$$K_{IC} = Y\sigma_f \sqrt{\pi a} \tag{A.1}$$

where $\sigma_f$ is the applied normal stress at fracture, $a$ is the edge-crack length and $Y$ is a dimensionless geometric constant on the order of 1. The SI units of fracture toughness are MPa-m$^{1/2}$.

When measuring fracture toughness in bending, $\sigma_f$ is taken to the maximum stress in the beam as described by simple beam theory [175],

$$\sigma_f = \frac{Mc}{I} \tag{A.2}$$

where $M$ is the applied moment, $c$ is the furthest distance from the neutral axis and $I$ is the moment of inertia of the cross-section about the neutral axis. For a beam of a circular cross section, $I = \frac{\pi d^4}{64}$ and $c = \frac{d}{2}$, $d$ as the diameter. In four-point-bend, the bending moment is $M = \frac{P_f(L_o - L_i)}{4}$, where $P_f$ is the applied force at fracture, and $L_o$ and $L_i$ are the outer and inner loading spans, respectively. Thus,

$$\sigma_f = \frac{8P_{max}(L_o - L_i)}{\pi d^3} \tag{A.3}$$

It follows then,

$$K_{IC} = \frac{8YP_{max}(L_o - L_i)\sqrt{a}}{\sqrt{\pi} d^3} \tag{A.4}$$

Using the finite element method, the geometric constant, $Y$ was determined for a surface crack in a long shaft under bending [122]. The value of $Y$ as a function of $a/d$ is shown in Fig. A.1. Note that in Fig. A.1, $Y = F_I$, $d = D$ and $a = b$. The equation of the curve fit for a circular cross-section and a notch radius of R = $\infty$ was found to be

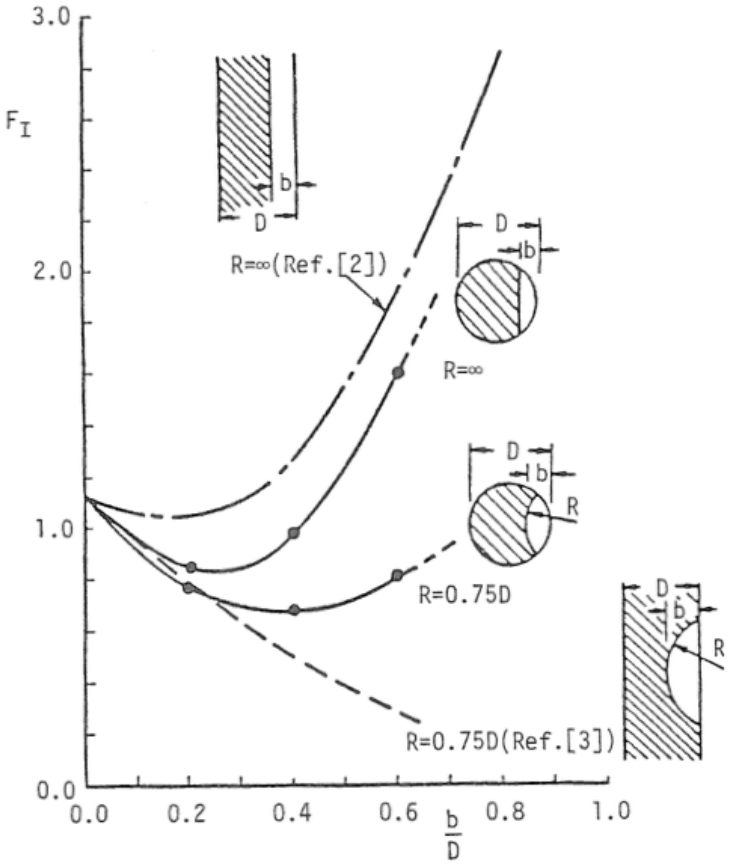


**Figure A.1**: Stress intensity factor for a surface crack in a long shaft. Note that $F_I = Y$, $D = d$ and $b = a$. Taken from [122].

$$Y = -30.332\left(\frac{a}{d}\right)^4 + 38.11\left(\frac{a}{d}\right)^3 - 9.2605\left(\frac{a}{d}\right)^2 - 0.828\left(\frac{a}{d}\right) + 1.12 \qquad \text{(A.5)}$$

Data points from the plot in Fig. A.1 match the modeled equation with an R-squared value of 0.9996.

# Bibliography


[1] D. Turnbull, "Under what conditions can a glass be formed?," *Contemporary Physics*, vol. 10, no. 5, pp. 473–488, 1969.

[2] W. Klement and R. H. Willens, "Non-crystalline structure in solidified gold–silicon alloys," *Nature*, vol. 187, no. 4740, pp. 869–870, 1960.

[3] A. Peker and W. L. Johnson, "A highly processable metallic glass: $Zr_{41.2}Ti_{13.8}Cu_{12.5}Ni_{10}Be_{22.5}$," *Applied Physics Letters*, vol. 63, no. 17, pp. 2342–2344, 1993.

[4] A. Inoue, T. Zhang, N. Nishiyama, K. Ohba, and T. Masumoto, "Preparation of 16 mm diameter rod of amorphous $Zr_{65}Al_{7.5}Ni_{10}Cu_{17.5}$ alloy," *Materials Transactions*, vol. 34, pp. 1234–1234, 1993.

[5] E. Ma and Z. Zhang, "Amorphous alloys: Reflections from the glass maze," *Nature Materials*, vol. 10, no. 1, pp. 10–11, 2011.

[6] G. Duan, A. Wiest, M.-L. Lind, A. Kahl, and W. L. Johnson, "Lightweight Ti-based bulk metallic glasses excluding late transition metals," *Scripta Materialia*, vol. 58, no. 6, pp. 465–468, 2008.

[7] X. Gu, S. J. Poon, and G. J. Shiflet, "Mechanical properties of iron-based bulk metallic glasses," *Journal of Materials Research*, vol. 22, no. 2, pp. 344–351, 2007.

[8] W. L. Johnson, "Bulk amorphous metal—An emerging engineering material," *JOM*, vol. 54, no. 3, pp. 40–43, 2002.

[9] W. Johnson, "Bulk metallic glass development." Online: http://vitreloy.caltech.edu/development.htm. Accessed March 2016.

[10] J. Das, M. Tang, K. Kim, R. Theissmann, F. Baier, W. Wang, and J. Eckert, ""Work-hardenable" ductile bulk metallic glass," *Physical Review Letters*, vol. 94, no. 20, p. 205501, 2005.

[11] J. Plummer, "Is metallic glass poised to come of age?," *Nature Materials*, vol. 14, no. 6, pp. 553–555, 2015.

[12] M. D. Demetriou, M. E. Launey, G. Garrett, J. P. Schramm, D. C. Hofmann, W. L. Johnson, and R. O. Ritchie, "A damage-tolerant glass," *Nature Materials*, vol. 10, no. 2, pp. 1–6, 2011.

[13] J. Dyre, "Colloquium: The glass transition and elastic models of glass-forming liquids," *Reviews of Modern Physics*, vol. 78, no. 3, pp. 953–972, 2006.

[14] S. Pauly, *Phase formation and mechanical properties of metastable Cu-Zr-based alloys*. PhD thesis, Dresden Technical University, 2010.

[15] G. H. Fredrickson, "Recent developments in dynamical theories of the liquid-glass transition," *Annual Review of Physical Chemistry*, vol. 39, no. 1, pp. 149–180, 1988.

[16] D. R. Uhlmann, "A kinetic treatment of glass formation," *Journal of Non-Crystalline Solids*, vol. 7, no. 4, pp. 337–348, 1972.

[17] R. Busch, "The thermophysical properties of bulk metallic glass-forming liquids," *JOM*, vol. 52, no. 7, pp. 39–42, 2000.

[18] X. H. Lin and W. L. Johnson, "Formation of Ti–Zr–Cu–Ni bulk metallic glasses," *Journal of Applied Physics*, vol. 78, no. 11, pp. 6514–7, 1995.

[19] S. Guo, Z. P. Lu, and C. T. Liu, "Identify the best glass forming ability criterion," *Intermetallics*, vol. 18, no. 5, pp. 883–888, 2010.

[20] H. Kozachkov, J. Kolodziejska, W. L. Johnson, and D. C. Hofmann, "Effect of cooling rate on the volume fraction of B2 phases in a CuZrAlCo metallic glass matrix composite," *Intermetallics*, vol. 39, pp. 89–93, 2013.

[21] ASTM-E1356-08, "Standard test method for assignment of the glass transition temperatures by differential scanning calorimetry," tech. rep., ASTM International, West Conshohocken, PA, 2014.

[22] ASTM-E794-06, "Standard test method for melting and crystallization temperatures by thermal analysis," tech. rep., ASTM International, West Conshohocken, PA, 2012.

[23] A. Inoue, "Stabilization of metallic supercooled liquid and bulk amorphous alloys," *Acta Materialia*, vol. 48, no. 1, pp. 279–306, 2000.

[24] N. Nishiyama and A. Inoue, "Direct comparison between critical cooling rate and some quantitative parameters for evaluation of glass-forming ability in Pd-Cu-Ni-P alloys," *Materials Transactions*, vol. 43, no. 8, pp. 1913–1917, 2002.

[25] Y. Zhang, Y. Li, H. Tan, G. L. Chen, and H. A. Davies, "Glass forming ability criteria for La–Al–(Cu,Ni) alloys," *Journal of Non-Crystalline Solids*, vol. 352, no. 52-54, pp. 5482–5486, 2006.

[26] C. Suryanarayana and A. Inoue, *Bulk Metallic Glasses*. CRC Press, 2011.

[27] Z. P. Lu, Y. Li, and S. C. Ng, "Reduced glass transition temperature and glass forming ability of bulk glass forming alloys," *Journal of Non-Crystalline Solids*, vol. 270, no. 1, pp. 103–114, 2000.

[28] D. Wang, Y. Li, B. B. Sun, M. L. Sui, K. Lu, and E. Ma, "Bulk metallic glass formation in the binary Cu–Zr system," *Applied Physics Letters*, vol. 84, no. 20, p. 4029, 2004.

[29] J. Cheney and K. Vecchio, "Prediction of glass-forming compositions using liquidus temperature calculations," *Materials Science and Engineering: A*, vol. 471, no. 1-2, pp. 135–143, 2007.

[30] Z. P. Lu, H. Bei, and C. T. Liu, "Recent progress in quantifying glass-forming ability of bulk metallic glasses," *Intermetallics*, vol. 15, no. 5-6, pp. 618–624, 2007.

[31] A. L. Greer and E. MA, "Bulk metallic glasses: at the cutting edge of metals research," *MRS Bulletin*, vol. 32, no. 08, pp. 611–619, 2007.

[32] A. Inoue, "Recent progress of Zr-based bulk amorphous alloys," *Science reports of the Research Institutes, Tohoku University. Ser. A, Physics, chemistry and metallurgy*, vol. 42, no. 1, pp. 1–11, 1996.

[33] Y. Wang, J. Qiang, C. Wong, C. Shek, and C. Dong, "Composition rule of bulk metallic glasses and quasicrystals using electron concentration criterion," *Journal of Materials Research*, vol. 18, no. 03, pp. 642–648, 2003.

[34] M. Miller and P. Liaw, *Bulk Metallic Glasses: An Overview*. SpringerLink : Bücher, Springer US, 2007.

[35] P. H. Gaskell, "A new structural model for amorphous transition metal silicides, borides, phosphides and carbides," *Journal of Non-Crystalline Solids*, vol. 32, no. 1, pp. 207–224, 1979.

[36] A. Inoue, T. Zhang, and T. Masumoto, "Zr–Al–Ni amorphous alloys with high glass transition temperature and significant supercooled liquid region," *Materials Transactions*, vol. 31, no. 3, pp. 177–183, 1990.

[37] A. Inoue, T. Negishi, H. M. Kimura, and T. Zhang, "High packing density of Zr-and Pd-based bulk amorphous alloys," *Materials Transactions*, vol. 39, no. 2, pp. 318–321, 1998.

[38] D. R. Nelson and F. Spaepen, "Polytetrahedral order in condensed matter," *Solid State Physics*, vol. 42, pp. 1–90, 1989.

[39] T. Egami and Y. Waseda, "Atomic size effect on the formability of metallic glasses," *Journal of Non-Crystalline Solids*, vol. 64, no. 1-2, pp. 113–134, 1984.

[40] D. B. Miracle, "A structural model for metallic glasses," *Nature*, vol. 3, no. 10, pp. 697–702, 2004.

[41] H. W. Sheng, W. K. Luo, F. M. Alamgir, J. M. Bai, and E. MA, "Atomic packing and short-to-medium-range order in metallic glasses," *Nature*, vol. 439, no. 7075, pp. 419–425, 2006.

[42] Y. Cheng, E. MA, and H. Sheng, "Atomic level structure in multicomponent bulk metallic glass," *Physical Review Letters*, vol. 102, no. 24, p. 245501, 2009.

[43] D. Xu, G. Duan, and W. Johnson, "Unusual glass-forming ability of bulk amorphous alloys based on ordinary metal copper," *Physical Review Letters*, vol. 92, no. 24, p. 245504, 2004.

[44] T. Fujita, K. Konno, W. Zhang, V. Kumar, M. Matsuura, A. Inoue, T. Sakurai, and M. Chen, "Atomic-scale heterogeneity of a multicomponent bulk metallic glass with excellent glass forming ability," *Physical Review Letters*, vol. 103, no. 7, p. 075502, 2009.

[45] X. K. Xi, L. L. Li, B. Zhang, W. H. Wang, and Y. Wu, "Correlation of atomic cluster symmetry and glass-forming ability of metallic glass," *Physical Review Letters*, vol. 99, no. 9, pp. 095501–4, 2007.

[46] P. S. Steif, F. Spaepen, and J. W. Hutchinson, "Strain localization in amorphous metals," *Acta Metallurgica*, vol. 30, no. 2, pp. 447–455, 1982.

[47] T. Masumoto and R. Maddin, "The mechanical properties of palladium 20 a/o silicon alloy quenched from the liquid state," *Acta Metallurgica*, vol. 19, no. 7, pp. 725–741, 1971.

[48] M. H. Cohen and D. Turnbull, "Molecular Transport in Liquids and Glasses," *The Journal of Chemical Physics*, vol. 31, no. 5, p. 1164, 1959.

[49] F. Spaepen, "A microscopic mechanism for steady state inhomogeneous flow in metallic glasses," *Acta Metallurgica*, vol. 25, no. 4, pp. 407–415, 1977.

[50] F. Spaepen, "Metallic glasses: Must shear bands be hot?," *Nature Materials*, vol. 5, no. 1, pp. 7–8, 2006.

[51] A. S. Argon, "Plastic deformation in metallic glasses," *Acta Metallurgica*, vol. 27, no. 1, pp. 47–58, 1979.

[52] C. Schuh, T. Hufnagel, and U. Ramamurty, "Mechanical behavior of amorphous alloys," *Acta Materialia*, vol. 55, no. 12, pp. 4067–4109, 2007.

[53] R. D. Conner, W. L. Johnson, N. E. Paton, and W. D. Nix, "Shear bands and cracking of metallic glass plates in bending," *Journal of Applied Physics*, vol. 94, no. 2, p. 904, 2003.

[54] W. Johnson and K. Samwer, "A universal criterion for plastic yielding of metallic glasses with a $(T/T_g)^{2/3}$) temperature dependence," *Physical Review Letters*, vol. 95, no. 19, p. 195501, 2005.

[55] D. Pan, A. Inoue, T. Sakurai, and M. Chen, "Experimental characterization of shear transformation zones for plastic flow of bulk metallic glasses," *Proceedings of the National Academy of Sciences*, vol. 105, no. 39, pp. 14769–14772, 2008.

[56] C. Schuh and T. Nieh, "A survey of instrumented indentation studies on metallic glasses," *Journal of Materials Research*, vol. 19, no. 01, pp. 46–57, 2004.

[57] H. Kimura and T. Masumoto, "Deformation and fracture of an amorphous PdCuSi alloy in V-notch bending tests—I: Model mechanics of inhomogeneous plastic flow in non-strain hardening solid," *Acta Metallurgica*, vol. 28, no. 12, pp. 1663–1675, 1980.

[58] C. Pampillo and H. Chen, "Comprehensive plastic deformation of a bulk metallic glass," *Materials Science and Engineering*, vol. 13, no. 2, pp. 181–188, 1974.

[59] S. Pugh, "XCII. relations between the elastic moduli and the plastic properties of polycrystalline pure metals," *The London, Edinburgh, and Dublin Philosophical Magazine and Journal of Science*, vol. 45, no. 367, pp. 823–843, 1954.

[60] J. J. Lewandowski, W. H. Wang, and A. L. Greer, "Intrinsic plasticity or brittleness of metallic glasses," *Philosophical Magazine Letters*, vol. 85, no. 2, pp. 77–87, 2005.

[61] M. Chen, "Mechanical behavior of metallic glasses: microscopic understanding of strength and ductility," *Annual Review of Materials Research*, vol. 38, no. 1, pp. 445–469, 2008.

[62] W. H. Wang, "Correlations between elastic moduli and properties in bulk metallic glasses," *Journal of Applied Physics*, vol. 99, no. 9, p. 093506, 2006.

[63] P. Yu and H. Y. Bai, "Poisson's ratio and plasticity in CuZrAl bulk metallic glasses," *Materials Science and Engineering A*, vol. 485, no. 1-2, pp. 1–4, 2008.

[64] J. Schroers and W. Johnson, "Ductile Bulk Metallic Glass," *Physical Review Letters*, vol. 93, no. 25, p. 255506, 2004.

[65] W. Weibull, "Wide applicability," *Journal of applied mechanics*, 1951.

[66] M. Calvo, "Application of the Weibull statistics to the characterization of metallic glass ribbons," *Journal of Materials Science*, vol. 24, no. 5, pp. 1801–1808, 1989.

[67] V. Ocelík, V. Z. Bengus, E. B. Korolkova, E. D. Tabachnikova, K. Csach, and P. Duhaj, "Fracture toughness of amorphous $Fe_{40}Ni_{40}B_{20}$ ribbons: strain rate dependence," *Journal of Materials Science Letters*, vol. 9, no. 5, pp. 529–531, 1990.

[68] W. F. Wu, Y. Li, and C. A. Schuh, "Strength, plasticity and brittleness of bulk metallic glasses under compression: statistical and geometric effects," *Philosophical Magazine*, vol. 88, no. 1, pp. 71–89, 2008.

[69] J. H. Yao, J. Q. Wang, L. Lu, and Y. Li, "High tensile strength reliability in a bulk metallic glass," *Applied Physics Letters*, vol. 92, no. 4, pp. 041905–4, 2008.

[70] Z. Han, L. C. Tang, J. Xu, and Y. Li, "A three-parameter Weibull statistical analysis of the strength variation of bulk metallic glasses," *Scripta Materialia*, vol. 61, no. 9, pp. 923–926, 2009.

[71] H.-L. Gao, Y. Shen, and J. Xu, "Weibull analysis of fracture strength for $Zr_{55}Ti_2Co_{28}Al_{15}$ bulk metallic glass: Tension–compression asymmetry and porosity effect," *Journal of Materials Research*, vol. 26, no. 16, pp. 2087–2097, 2011.

[72] C. Lu, R. Danzer, and F. D. Fischer, "Influence of threshold stress on the estimation of the Weibull statistics," *Journal of the American Ceramic Society*, vol. 85, no. 6, pp. 1640–1642, 2002.

[73] W. Zhang, Q. Zhang, C. Qin, and A. Inoue, "Synthesis and properties of Cu–Zr–Ag–Al glassy alloys with high glass-forming ability," *Materials Science and Engineering: B*, vol. 148, no. 1-3, pp. 92–96, 2008.

[74] S.-W. Lee, M.-Y. Huh, E. Fleury, and J.-C. Lee, "Crystallization-induced plasticity of Cu–Zr containing bulk amorphous alloys," *Acta Materialia*, vol. 54, no. 2, pp. 349–355, 2006.

[75] W. H. Wang, J. J. Lewandowski, and A. L. Greer, "Understanding the glass-forming ability of $Cu_{50}Zr_{50}$ alloys in terms of a metastable eutectic," *Journal of Materials Research*, vol. 20, no. 9, pp. 2307–2313, 2011.

[76] X. C. He, H. Wang, H. S. Liu, and Z. P. Jin, "Thermodynamic description of the Cu–Ag–Zr system," *Calphad*, vol. 30, no. 4, pp. 367–374, 2006.

[77] Z. Altounian, T. Guo-hua, and J. O. Strom-Olsen, "Crystallization characteristics of Cu-Zr metallic glasses from $Cu_{70}Zr_{30}$ to $Cu_{25}Zr_{75}$," *Journal of Applied Physics*, vol. 53, no. 7, pp. 4755–7, 1982.

[78] D. Xu, B. Lohwongwatana, G. Duan, W. L. Johnson, and C. Garland, "Bulk metallic glass formation in binary Cu-rich alloy series $Cu_{100-x}Zr_x$ (x = 34, 36, 38.2, 40 at.%) and mechanical properties of bulk $Cu_{64}Zr_{36}$ glass," *Acta Materialia*, vol. 52, no. 9, pp. 2621–2624, 2004.

[79] A. Inoue and W. Zhang, "Formation, thermal stability and mechanical properties of Cu-Zr and Cu-Hf binary glassy alloy rods," *Materials Transactions*, vol. 45, no. 2, pp. 584–587, 2004.

[80] T. Mei-Bo, Z. De-Qian, P. Ming-Xiang, and W. Wei-Hua, "Binary Cu–Zr bulk metallic glasses," *Chinese Physics Letters*, vol. 21, no. 5, p. 901, 2004.

[81] W. H. Wang, Z. Bian, P. Wen, Y. Zhang, M. X. Pan, and D. Q. Zhao, "Role of addition in formation and properties of Zr-based bulk metallic glasses," *Intermetallics*, vol. 10, no. 11-12, pp. 1249–1257, 2002.

[82] G. J. Fan, M. Freels, H. Choo, P. K. Liaw, J. J. Z. Li, W.-K. Rhim, W. L. Johnson, P. Yu, and W. H. Wang, "Thermophysical and elastic properties of $Cu_{50}Zr_{50}$ and $(Cu_{50}Zr_{50})_{95}Al_5$ bulk-metallic-glass-forming alloys," *Applied Physics Letters*, vol. 89, no. 24, p. 241917, 2006.

[83] K. B. Kim, J. Das, F. Baier, M. B. Tang, W. H. Wang, and J. Eckert, "Heterogeneity of a $Cu_{47.5}Zr_{47.5}Al_5$ bulk metallic glass," *Applied Physics Letters*, vol. 88, no. 5, p. 051911, 2006.

[84] J. Eckert, J. Das, K. B. Kim, F. Baier, M. B. Tang, W. H. Wang, and Z. F. Zhang, "High strength ductile Cu-base metallic glass," *Intermetallics*, vol. 14, no. 8-9, pp. 876–881, 2006.

[85] G. Kumar, T. Ohkubo, T. Mukai, and K. Hono, "Plasticity and microstructure of Zr–Cu–Al bulk metallic glasses," *Scripta Materialia*, vol. 57, no. 2, pp. 173–176, 2007.

[86] Y. Wu, H. Wang, H. H. Wu, Z. Y. Zhang, X. D. Hui, G. L. Chen, D. Ma, X. L. Wang, and Z. P. Lu, "Formation of Cu-Zr-Al bulk metallic glass composites with improved tensile properties," *Acta Materialia*, vol. 59, no. 8, pp. 2928–2936, 2011.

[87] Y. N. Koval, G. Firstov, L. Delaey, and J. Humbeeck, "The influence of Ni and Ti on the martensitic transformation and shape memory effect of the intermetallic compound ZrCu," *Scripta Metallurgica et Materialia*, vol. 31, no. 7, pp. 799–802, 1994.

[88] S. Pauly, G. Liu, G. Wang, U. Kühn, N. Mattern, and J. Eckert, "Microstructural heterogeneities governing the deformation of $Cu_{47.5}Zr_{47.5}Al_5$ bulk metallic glass composites," *Acta Materialia*, vol. 57, no. 18, pp. 5445–5453, 2009.

[89] A. L. Greer, "Confusion by design," *Nature*, vol. 366, pp. 303–304, 1993.

[90] A. Emge, S. Karthikeyan, and D. Rigney, "The effects of sliding velocity and sliding time on nanocrystalline tribolayer development and properties in copper," *Wear*, vol. 267, no. 1, pp. 562–567, 2009.

[91] I. Garbar, "The effect of load on the structure and wear of friction pair materials (example of low-carbon steel and copper)," *Wear*, vol. 205, no. 1, pp. 240–245, 1997.

[92] A. Gåård, N. Hallbäck, P. Krakhmalev, and J. Bergström, "Temperature effects on adhesive wear in dry sliding contacts," *Wear*, vol. 268, no. 7, pp. 968–975, 2010.

[93] J. R. Davis, *Gear Materials, Properties, and Manufacture*. ASM International, 2005.

[94] B. Bhushan, *Introduction to Tribology*. John Wiley & Sons, 2013.

[95] B. Bhushan, R. E. Davis, and H. R. Kolar, "Metallurgical re-examination of wear modes ii: Adhesive and abrasive," *Thin Solid Films*, vol. 123, no. 2, pp. 113–126, 1985.

[96] J. F. Archard, "Contact and Rubbing of Flat Surfaces," *Journal of Applied Physics*, vol. 24, no. 8, pp. 981–9, 1953.

[97] J. F. Archard and W. Hirst, "The wear of metals under unlubricated conditions," *Proceedings of the Royal Society A: Mathematical, Physical and Engineering Sciences*, vol. 236, no. 1206, pp. 397–410, 1956.

[98] A. L. Greer, K. L. Rutherford, and I. M. Hutchings, "Wear resistance of amorphous alloys and related materials," *International Materials Reviews*, vol. 47, no. 2, pp. 87–112, 2002.

[99] G. R. Gillis-Smith and D. Petercsak, "Compact drilling and sample system," in *32nd Aerospace Mechanisms Symposium*, p. 141, 1998.

[100] R. O. Ritchie, "The conflicts between strength and toughness," *Nature Materials*, vol. 10, no. 11, pp. 817–822, 2011.

[101] M. Ashby and A. Greer, "Metallic glasses as structural materials," *Scripta Materialia*, vol. 54, no. 3, pp. 321–326, 2006.

[102] D. C. Hofmann, J.-Y. Suh, A. Wiest, G. Duan, M.-L. Lind, M. D. Demetriou, and W. L. Johnson, "Designing metallic glass matrix composites with high toughness and tensile ductility," *Nature*, vol. 451, no. 7182, pp. 1085–1089, 2008.

[103] G. Q. Zhang, X. J. Li, M. Shao, L. N. Wang, J. L. Yang, L. P. Gao, L. Y. Chen, and C. X. Liu, "Wear behavior of a series of Zr-based bulk metallic glasses," *Materials Science and Engineering: A*, vol. 475, no. 1-2, pp. 124–127, 2008.

[104] M. Ishida, H. Takeda, N. Nishiyama, K. Kita, Y. Shimizu, Y. Saotome, and A. Inoue, "Wear resistivity of super-precision microgear made of Ni-based metallic glass," *Materials Science and Engineering: A*, vol. 449-451, pp. 149–154, 2007.

[105] D. Z. Segu, J. H. Choi, S. Yi, and S. S. Kim, "Dry sliding tribological properties of Fe-based bulk metallic glass," *Tribology Letters*, vol. 47, no. 1, pp. 131–138, 2012.

[106] C. Y. Tam and C. H. Shek, "Abrasion resistance of Cu-based bulk metallic glasses," *Journal of Non-Crystalline Solids*, vol. 347, no. 1-3, pp. 268–272, 2004.

[107] D. Maddala and R. J. Hebert, "Effect of notch toughness and hardness on sliding wear of $Cu_{50}Hf_{41.5}Al_{8.5}$ bulk metallic glass," *Scripta Materialia*, vol. 65, no. 7, pp. 630–633, 2011.

[108] D. J. Branagan, W. D. Swank, D. C. Haggard, and J. R. Fincke, "Wear-resistant amorphous and nanocomposite steel coatings," *Metallurgical and Materials Transactions A*, vol. 32, no. 10, pp. 2615–2621, 2001.

[109] M. Z. Ma, R. P. Liu, Y. Xiao, D. C. Lou, L. Liu, Q. Wang, and W. K. Wang, "Wear resistance of Zr-based bulk metallic glass applied in bearing rollers," *Materials Science and Engineering: A*, vol. 386, no. 1-2, pp. 326–330, 2004.

[110] Y. Wu, Y. Xiao, G. Chen, C. T. Liu, and Z. Lu, "Bulk metallic glass composites with transformation-mediated work-hardening and ductility," *Advanced Materials*, vol. 22, no. 25, pp. 2770–2773, 2010.

[111] V. Ponnambalam, S. J. Poon, and G. J. Shiflet, "Fe-based bulk metallic glasses with diameter thickness larger than one centimeter," *Journal of Materials Research*, vol. 19, no. 5, pp. 1320–1323, 2004.

[112] C. Qing-Jun, S. Jun, F. Hong-Bo, S. Jian-Fei, H. Yong-Jiang, and M. D. G, "Glass-forming ability of an iron-based alloy enhanced by Co addition and evaluated by a new criterion," *Chinese Physics Letters*, vol. 22, no. 7, pp. 1736–1738, 2005.

[113] J. M. Park, H. J. Chang, K. H. Han, W. T. Kim, and D. H. Kim, "Enhancement of plasticity in Ti-rich Ti–Zr–Be–Cu–Ni bulk metallic glasses," *Scripta Materialia*, vol. 53, pp. 1–6, July 2005.

[114] H. T. Duan, J. S. Tu, S. M. Du, H. C. Kou, Y. Li, J. P. Wang, Z. W. Chen, and J. Li, "Tribological properties of $Ti_{40}Zr_{25}Ni_8Cu_9Be_{18}$ bulk metallic glasses under different conditions," *Materials & Design*, vol. 32, pp. 4573–4579, Sept. 2011.

[115] X. H. Lin, W. L. Johnson, and W. K. Rhim, "Effect of oxygen impurity on crystallization of an undercooled bulk glass forming Zr–Ti–Cu–Ni–Al alloy," *Materials Transactions*, vol. 38, no. 5, pp. 473–477, 1997.

[116] O. Haruyama, Y. Nakayama, R. Wada, H. Tokunaga, J. Okada, T. Ishikawa, and Y. Yokoyama, "Volume and enthalpy relaxation in $Zr_{55}Cu_{30}Ni_5Al_{10}$ bulk metallic glass," *Acta Materialia*, vol. 58, no. 5, pp. 1829–1836, 2010.

[117] T. Wada, T. Zhang, and A. Inoue, "Formation, thermal stability and mechanical properties in Zr-Al-Co bulk glassy alloys.," *Materials Transactions*, vol. 43, no. 11, pp. 2843–2846, 2002.

[118] A. A. Kündig, J. F. Löffler, W. L. Johnson, P. J. Uggowitzer, and P. Thiyagarajan, "Influence of decomposition on the thermal stability of undercooled Zr-Ti-Cu-Ni-Al alloys," *Scripta Materialia*, vol. 44, no. 8-9, pp. 1269–1273, 2001.

[119] G. Duan, A. Wiest, M. L. Lind, J. Li, W. K. Rhim, and W. L. Johnson, "Bulk metallic glass with benchmark thermoplastic processability," *Advanced Materials*, vol. 19, no. 23, pp. 4272–4275, 2007.

[120] ASTM-G99-05, "Standard test method for wear testing with a pin-on-disk apparatus," tech. rep., ASTM International, West Conshohocken, PA, 2010.

[121] ASTM-E399-12e3, "Standard test method for linear-elastic plane-strain fracture toughness $K_{IC}$ of metallic materials," tech. rep., ASTM International, West Conshohocken, PA, 2012.

[122] Y. Murakami, *Stress Intensity Factors Handbook*. No. v. 2, Pergamon Press, Oxford, UK, 1988.

[123] D. V. Louzguine-Luzgin, D. B. Miracle, and A. Inoue, "Intrinsic and Extrinsic Factors Influencing the Glass-Forming Ability of Alloys," *Advanced Engineering Materials*, vol. 10, no. 11, pp. 1008–1015, 2008.

[124] D. C. Hofmann and B. Wilcox, "Systems and methods for implementing bulk metallic glass-based strain wave gears and strain wave gear components," Feb. 11 2014. US Patent App. 14/177,608.

[125] D. R. Maddala, A. Mubarok, and R. J. Hebert, "Sliding wear behavior of $Cu_{50}Hf_{41.5}Al_{8.5}$ bulk metallic glass," *Wear*, vol. 269, no. 7-8, pp. 572–580, 2010.

[126] N. Togashi, M. Ishida, N. Nishiyama, and A. Inoue, "Wear resistance of metallic glass bearings," *Reviews on Advanced Materials Science*, vol. 18, pp. 93–97, 2008.

[127] R. Moreton and J. Lancaster, "The friction and wear behavior of various metallic glasses," *Journal of Materials Science Letters*, vol. 4, no. 2, pp. 133–137, 1985.

[128] S.-W. Lee, S.-C. Lee, Y.-C. Kim, E. Fleury, and J.-C. Lee, "Design of a bulk amorphous alloy containing Cu–Zr with simultaneous improvement in glass-forming ability and plasticity," *Journal of Materials Research*, vol. 22, no. 02, pp. 486–492, 2007.

[129] Y. Liu, Z. Yitian, L. Xuekun, and Z. Liu, "Wear behavior of a Zr-based bulk metallic glass and its composites," *Journal of Alloys and Compounds*, vol. 503, no. 1, pp. 138–144, 2010.

[130] D. H. Kwon, E. S. Park, M. Y. Huh, H. J. Kim, and J. C. Bae, "Wear behavior of Fe-based bulk metallic glass composites," *Journal of Alloys and Compounds*, vol. 509, pp. S105–S108, 2011.

[131] T. Gloriant, "Microhardness and abrasive wear resistance of metallic glasses and nanostructured composite materials," *Journal of Non-Crystalline Solids*, vol. 316, no. 1, pp. 96–103, 2003.

[132] G. Y. Lee, C. Dharan, and R. O. Ritchie, "A physically-based abrasive wear model for composite materials," *Wear*, vol. 252, no. 3-4, pp. 322–331, 2002.

[133] E. Rabinowicz, *Friction and Wear of Materials*. Wiley series on the science and technology of materials, Wiley, 1965.

[134] D. C. Hofmann, L. M. Andersen, J. Kolodziejska, S. Roberts, J. P. Borgonia, K. S. Vecchio, and A. Kennett, "Optimizing bulk metallic glasses for robust, highly wear-resistant gears," *Unpublished research*, 2016.

[135] D. Qiao, G. Fan, P. Liaw, and H. Choo, "Fatigue behaviors of the $Cu_{47.5}Zr_{47.5}Al_5$ bulk-metallic glass (BMG) and $Cu_{47.5}Zr_{38}Hf_{9.5}Al_5$ BMG composite," *International Journal of Fatigue*, vol. 29, no. 12, pp. 2149–2154, 2007.

[136] P. Jia, Z.-d. Zhu, E. Ma, and J. Xu, "Notch toughness of Cu-based bulk metallic glasses," *Scripta Materialia*, vol. 61, no. 2, pp. 137–140, 2009.

[137] Q. He, Y.-Q. Cheng, E. Ma, and J. Xu, "Locating bulk metallic glasses with high fracture toughness: Chemical effects and composition optimization," *Acta Materialia*, vol. 59, no. 1, pp. 202–215, 2011.

[138] P. Lowhaphandu and J. J. Lewandowski, "Fracture toughness and notched toughness of bulk amorphous alloy: Zr-Ti-Ni-Cu-Be," *Scripta Materialia*, vol. 38, no. 12, 1998.

[139] L. K. Zhang, Z. H. Chen, D. Chen, X. Y. Zhao, and Q. Zheng, "Four-point-bending-fatigue behavior of the $Cu_{45}Zr_{45}Ag_7Al_3$ bulk metallic glass," *Journal of Non-Crystalline Solids*, vol. 370, no. C, pp. 31–36, 2013.

[140] A. Kawashima, H. Kurishita, H. Kimura, T. Zhang, and A. Inoue, "Fracture toughness of $Zr_{55}Al_{10}Ni_5Cu_{30}$ bulk metallic glass by 3-point bend testing," *Materials Transactions*, vol. 46, no. 7, p. 1725, 2005.

[141] D. Wang, H. Tan, and Y. Li, "Multiple maxima of GFA in three adjacent eutectics in Zr–Cu–Al alloy system—A metallographic way to pinpoint the best glass forming alloys," *Acta Materialia*, vol. 53, no. 10, pp. 2969–2979, 2005.

[142] B. Gludovatz, S. E. Naleway, R. O. Ritchie, and J. J. Kruzic, "Size-dependent fracture toughness of bulk metallic glasses," *Acta Materialia*, vol. 70, no. C, pp. 198–207, 2014.

[143] J.-Y. Suh, R. Dale Conner, C. Paul Kim, M. D. Demetriou, and W. L. Johnson, "Correlation between fracture surface morphology and toughness in Zr-based bulk metallic glasses," *Journal of Materials Research*, vol. 25, no. 5, pp. 982–990, 2010.

[144] V. Raghavan, "Al-Cu-Zr (Aluminum-Copper-Zirconium)," *Journal of Phase Equilibria and Diffusion*, vol. 32, no. 5, pp. 452–454, 2011.

[145] J. Ketkaew, Z. Liu, W. Chen, and J. Schroers, "Critical crystallization for embrittlement in metallic glasses," *Physical Review Letters*, vol. 115, no. 26, pp. 265502–6, 2015.

[146] S. M. Chathoth, B. Damaschke, J. P. Embs, and K. Samwer, "Giant changes in atomic dynamics on microalloying metallic melt," *Applied Physics Letters*, vol. 95, no. 19, pp. 191907–4, 2009.

[147] Y. J. Huang, J. Shen, and J. F. Sun, "Bulk metallic glasses: Smaller is softer," *Applied Physics Letters*, vol. 90, no. 8, pp. 081919–4, 2007.

[148] F. Jiang, M. Q. Jiang, H. F. Wang, Y. L. Zhao, L. He, and J. Sun, "Shear transformation zone volume determining ductile–brittle transition of bulk metallic glasses," *Acta Materialia*, vol. 59, no. 5, pp. 2057–2068, 2011.

[149] Y. Huang, H. Fan, D. Wang, Y. Sun, F. Liu, J. Shen, J. Sun, and J. Mi, "The effect of cooling rate on the wear performance of a ZrCuAlAg bulk metallic glass," *Journal of Materials & Design*, vol. 58, no. C, pp. 284–289, 2014.

[150] Y. Liu, H. Bei, C. T. Liu, and E. P. George, "Cooling-rate induced softening in a $Zr_{50}Cu_{50}$ bulk metallic glass," *Applied Physics Letters*, vol. 90, no. 7, pp. 071909–4, 2007.

[151] J. Schroers, "Processing of Bulk Metallic Glass," *Advanced Materials*, vol. 22, no. 14, pp. 1566–1597, 2009.

[152] F. Qiu, P. Shen, T. Liu, and Q. Jiang, "Enhanced ductility in a $Zr_{65}Cu_{15}Al_{10}Ni_{10}$ bulk metallic glass by nanocrystallization during compression," *Materials & Design*, vol. 36, no. C, pp. 168–171, 2012.

[153] A. L. Greer, "Partially or fully devitrified alloys for mechanical properties," *Materials Science and Engineering: A*, vol. 304-306, pp. 68–72, 2001.

[154] C. J. Gilbert, R. O. Ritchie, and W. L. Johnson, "Fracture toughness and fatigue-crack propagation in a Zr–Ti–Ni–Cu–Be bulk metallic glass," *Applied Physics Letters*, vol. 71, no. 4, pp. 476–478, 1997.

[155] C. P. Kim, J.-Y. Suh, A. Wiest, M.-L. Lind, R. D. Conner, and W. L. Johnson, "Fracture toughness study of new Zr-based Be-bearing bulk metallic glasses," *Scripta Materialia*, vol. 60, no. 2, pp. 79–82, 2009.

[156] Z. W. Zhu, H. F. Zhang, H. Wang, B. Z. Ding, and Z. Q. Hu, "Influence of casting temperature on the thermal stability of Cu- and Zr-based metallic glasses: Theoretical analysis and experiments," *Journal of Materials Research*, vol. 23, no. 10, pp. 2714–2719, 2011.

[157] A. Inoue and T. Zhang, "Fabrication of bulk glassy $Zr_{55}Al_{10}Ni_5Cu_{30}$ alloy of 30 mm in diameter by a suction casting method," *Materials Transactions*, vol. 37, no. 2, pp. 185–187, 1996.

[158] "Alfa Aesar 2013-15 Catalog of Research Chemicals, Metals and Materials," Accessed December 2014. https://www.alfa.com/en/.

[159] A. Takeuchi and A. Inoue, "Classification of bulk metallic glasses by atomic size difference, heat of mixing and period of constituent elements and its application to characterization of the main alloying element," *Materials Transactions*, vol. 46, no. 12, pp. 2817–2829, 2005.

[160] I. A. Figueroa, H. Zhao, S. González, H. A. Davies, and I. Todd, "Bulk glass formability for Cu–Hf–Zr–Ag and Cu–Zr–Ag–Si alloys," *Journal of Non-Crystalline Solids*, vol. 354, no. 47-51, pp. 5181–5183, 2008.

[161] D. Qiao and A. Peker, "Enhanced glass forming ability in Zr-based bulk metallic glasses with Hf Addition," *Intermetallics*, vol. 24, no. C, pp. 115–119, 2012.

[162] H. Y. Ding, Y. Shao, P. Gong, J. F. Li, and K. F. Yao, "A senary TiZrHfCuNiBe high entropy bulk metallic glass with large glass-forming ability," *Materials Letters*, vol. 125, no. C, pp. 151–153, 2014.

[163] X. Gu, L. Q. Xing, and T. C. Hufnagel, "Glass-forming ability and crystallization of bulk metallic glass $(Hf_xZr_{1-x})_{52.5}Cu_{17.9}Ni_{14.6}Al_{10}Ti_5$ ," *Journal of Non-Crystalline Solids*, vol. 311, no. 1, pp. 77–82, 2002.

[164] X. Gu, T. Jiao, L. J. Kecskes, R. H. Woodman, C. Fan, K. T. Ramesh, and T. C. Hufnagel, "Crystallization and mechanical behavior of (Hf, Zr)–Ti–Cu–Ni–Al metallic glasses," *Journal of Non-Crystalline Solids*, vol. 317, no. 1-2, pp. 112–117, 2003.

[165] W. Zhang and A. Inoue, "Thermal stability and mechanical properties of Cu-based bulk glassy alloys in $Cu_{50}(Zr_{1-x}Hf_x)_{45}Al_5$ system," *Materials Transactions*, vol. 44, no. 10, pp. 2220–2223, 2003.

[166] F. Jia, W. Zhang, and A. Inoue, "Effects of additional Hf on the thermal stability and mechanical properties of Cu-Zr-Ag bulk glassy alloys," *Materials Transactions*, vol. 47, no. 8, pp. 1922–1925, 2006.

[167] L. M. Andersen, S. Faulhaber, D. C. Hofmann, and K. S. Vecchio, "Criteria to optimize the toughness of Cu-Zr-based bulk metallic glasses with in-situ crystallization," *Unpublished research*, 2016.

[168] J. Cheney and K. Vecchio, "Evaluation of glass-forming ability in metals using multi-model techniques," *Journal of Alloys and Compounds*, vol. 471, no. 1-2, pp. 222–240, 2009.

[169] V. Keryvin, C. Bernard, J. C. Sanglebœuf, Y. Yokoyama, and T. Rouxel, "Toughness of $Zr_{55}Cu_{30}Al_{10}Ni_5$ bulk metallic glass for two oxygen levels," *Journal of non-crystalline solids*, vol. 352, no. 26-27, pp. 2863–2868, 2006.

[170] A. Gebert, J. Eckert, and L. Schultz, "Effect of oxygen on phase formation and thermal stability of slowly cooled $Zr_{65}Al_{7.5}Cu_{17.5}Ni_{10}$ metallic glass," *Acta Materialia*, vol. 46, no. 15, pp. 5475–5482, 1998.

[171] R. Bhowmick, B. Majumdar, D. K. Misra, U. Ramamurty, and K. Chattopadhyay, "Synthesis of bulk metallic glass composites using high oxygen containing Zr sponge," *Journal of Materials Science*, vol. 42, no. 22, pp. 9359–9365, 2007.

[172] M. A. Meyers and K. K. Chawla, *Mechanical Behavior of Materials*. Cambridge University Press, Cambridge, UK, 2009.

[173] K. Kendall, N. Alford, S. R. Tan, and J. D. Birchall, "Influence of toughness on Weibull modulus of ceramic bending strength," *Journal of Materials Research*, vol. 1, no. 01, pp. 120–123, 1986.

[174] W. Smith and J. Hashemi, *Foundations of Materials Science and Engineering*. McGraw-Hill, 2003.

[175] B. T. Sparenberg, D. D. Arola, G. D. Quinn, L. K. Ives, P. Koshy, and S. Jahanmir, "Flexural strength of ceramic and glass rods," *Journal of Testing and Evaluation*, vol. 37, no. 3, pp. 1–23, 2009.